

Faculty of Engineering and Built Environment

**School of Engineering**

**Mechanical Engineering Project B**

**Semester 1 - 2016**



**PROJECT TITLE**

Simulated Strain Field Reconstruction via Bragg-Edge Neutron Transmission

**NAME**

Alexander William Thomas Gregg

**SUPERVISOR**

Associate Professor Christopher Wensrich



**FINAL YEAR PROJECT**



# **Simulated Strain Field Reconstruction via Bragg-Edge Neutron Transmission**



THE UNIVERSITY OF  
**NEWCASTLE**  
AUSTRALIA

by

Alexander W. T. Gregg

A thesis submitted in partial fulfilment for the  
degree of Bachelor of Engineering (Mechanical) (Honours)

Faculty of Engineering and Built Environment  
School of Engineering

March 2017



# Declaration

I declare that this thesis is my own work unless otherwise acknowledged and is in accordance with the University's academic integrity policy available from the Policy Library on the web at  
<http://www.newcastle.edu.au/policylibrary/000608.html>

I certify that this assessment item has not been submitted previously for academic credit in this or any other course.

I acknowledge that the Faculty of Engineering may, for the purpose of assessing this thesis:

- Reproduce this thesis and provide a copy to another member of the Faculty; and/or
- Communicate a copy of this assessment item to a plagiarism checking service (which may then retain a copy of the item on its database for the purpose of future plagiarism checking).
- Submit the assessment item to other forms of plagiarism checking.

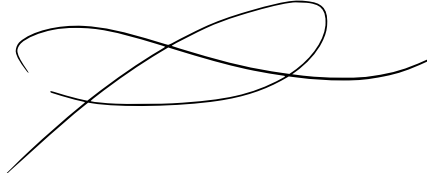
I further acknowledge that the Faculty of Engineering may, for the purpose of sector wide Quality Assurance:

- Reproduce this thesis to provide a copy to a member of another engineering faculty.

I certify that the electronic versions of this thesis I have submitted are identical to this hardcopy version. Furthermore, I have checked that the electronic version is complete and intact on the submitted location.

Student name: Alexander William Thomas Gregg

Signature

A handwritten signature in black ink, appearing to read "Alexander William Thomas Gregg". The signature is fluid and cursive, with a large loop on the left and a more vertical section on the right.



# Acknowledgements

I owe a debt of gratitude to those who have invested their time and effort in helping me complete my undergraduate studies.

To the postgraduate students ('The Condors') of ES320 — Mariana, Dave, Mark, Dylan, Anthony, Sam, Joss, Alex and Shaun — thank you for your hospitality, guidance and company. You have helped cement my decision to undertake postgraduate studies. I have enjoyed knowing each of you and learning about your research.

To my friend Johannes, thank you for your company and mentoring, our morning coffees, and the many thesis drafts you have reviewed! I am inspired by your drive and passion and your constant encouragement has certainly helped me approach new fields of knowledge with confidence.

I would also like to acknowledge Professor Erich Kisi and Associate Professor Adrian Wills for your consultation and guidance on the specifics of Neutron Diffraction and Optimisation, respectively.

I owe particular thanks to my supervisor and mentor, Associate Professor Christopher Wensrich. You have provided for me endless opportunity these past two years, and I am beyond grateful. I have enjoyed every aspect of our research — particularly the head-scratching, whiteboard-staring sessions. Your constant guidance, direction and support have kept me on the right path and opened my eyes to how much I still have to learn! I truly look forward to the next three years of research under your supervision.

Finally, to my family, for the sacrifices you have made and opportunities you've provided. This thesis is dedicated to you.



# Abstract

For many years, neutron *diffraction* techniques have provided a means of mapping the elastic strain tensor field within a sample composed of an engineering material. Usually, strain is measured within a representative volume element at a number of discrete points. Knowledge of the elastic strain allows for determination of internal stresses present (via Hooke's Law). This is of great importance in validation and calibration of mathematical models (such as those generated by finite element packages) which are crucial in the iterative nature of engineering design, and in failure prediction and analysis. Unfortunately, this process is extremely labour intensive, and discrete measurements fail to completely characterise the system.

In medicine, a method known as Computed Tomography (CT) imaging exploits the attenuation of electromagnetic waves as they penetrate an object to reconstruct complete, three dimensional models of the human body. In an analogous way to CT, Bragg-Edge Neutron *transmission* methods have recently shown promise in the *tomographic* reconstruction of the complete elastic strain tensor field within a sample.

The scarcity of suitable experimental data (largely due to the specialised equipment necessary to perform Bragg-Edge neutron measurements) has led to the development of a numerical measurement simulation environment and reconstruction algorithm.

This thesis represents a significant extension to the body of knowledge concerning Bragg-Edge neutron strain tomography. As a result of this project, (simulated) Bragg-Edge strain field reconstruction of non-axisymmetric systems has been achieved for the first time (under *in-situ* loading assumptions), and the prospect of general tomographic reconstruction is now within arms reach. Additionally, a journal article, largely composed of results from this project has been published ([Appendix B](#)) and a second article is currently being prepared for submission ([Appendix C](#)).



# Nomenclature

Listed in order of first appearance. Vectors are generally typeset as lowercase **bold** letters. Tensors are generally typeset as uppercase **bold** characters. In the case of greek characters, the nature of the symbol is defined in the nomenclature. Hats generally indicate unit vectors, and subscripts are usually used to indicate a specific quantity.

## Chapter 1

Symbol	Units	Description
$\lambda$	[m]	Radiation wavelength
$d$	[m]	Atomic lattice spacing
$\theta$	[degrees]	Angle of reflection
$y$	[ $-$ ]	Average Bragg-Edge strain measurement
$d_0$	[m]	Unstrained atomic lattice spacing
$\epsilon(x, y, z)$	[ $-$ ]	3D Strain tensor field
$\epsilon(x, y)$	[ $-$ ]	2D Strain tensor field
$\hat{n}$	[m]	Ray propagation direction unit vector
$x_0$	[m]	Ray entry point position vector
$s$	[m]	Ray propagation distance co-ordinate
$L$	[m]	Total ray irradiation distance

## Chapter 2

Symbol	Units	Description
$\phi(x, y)$	[m]	Sample deformation vector field
$u$	[m]	$x$ component of deformation
$v$	[m]	$y$ component of deformation
$H(x, y)$	[ $-$ ]	Deformation gradient tensor field
$\nabla$	[ $1/m$ ]	Euclidean Grad vector
$\phi_p$	[m]	Ray entry point deformation vector

$\phi_q$	[m]	Ray exit point deformation vector
$\phi_a$	[m]	Ray entry point deformation vector (through-node case)
$\phi_b$	[m]	Ray exit point deformation vector (through-node case)
$\phi_{a_1}, \phi_{a_2}$	[m]	Ray entry point deformation vectors (between-nodes case)
$\phi_{b_1}, \phi_{b_2}$	[m]	Ray exit point deformation vectors (between-nodes case)
$d$	[m]	Intersect distance between nodes (shape function evaluations)
$D$	[m]	Total distance between nodes (shape function evaluations)
$N(d)$	[‐]	Shape function
$A$	[ $\frac{1}{m}$ ]	Discretised boundary reconstruction problem co-efficient matrix
$\Phi$	[m]	Vector of unknown boundary node deformation components
$\Phi^*$	[m]	Reconstructed vector of unknown boundary node deformation components
$\mathbf{y}$	[m]	Vector of Bragg-Edge measurements
$\phi_r$	[m]	Boundary rigid body motion

## Chapter 3

Symbol	Units	Description
$\theta$	[rad]	Ray projection Angle
$j$	[‐]	Number of finite-element Gauss points
$\varepsilon_t$	[‐]	True strain field (vector)
$\varepsilon_r$	[‐]	Reconstructed strain field (vector)
$P$	[N]	Cantilevered beam edge load
$l$	[m]	Cantilevered beam length
$h$	[m]	Cantilevered beam height
$t$	[m]	Cantilevered beam thickness
$E$	[Pa]	Young's modulus
$\nu$	[‐]	Poisson's ratio
$N$	[‐]	Number of projections taken
$\mathbf{y}'$	[‐]	Vector of Bragg-Edge measurements with noise
$\mathcal{N}(0, \sigma)$	[‐]	Zero-mean normally distributed noise
$\sigma$	[‐]	Noise standard deviation
$\chi(s)$	[‐]	Exponential decay (attenuation) weighting function
$\mu$	[ $m^{-1}$ ]	Linear attenuation co-efficient
$t$	[m]	Ray propagation width co-ordinate
$\hat{\mathbf{n}}^\perp$	[m]	Ray propagation direction perpendicular unit vector
$W$	[m]	Ray width

## Chapter 4

<b>Symbol</b>	<b>Units</b>	<b>Description</b>
$\epsilon(x, y)$	[·]	Total strain field
$\epsilon_E(x, y)$	[·]	Elastic strain field
$\epsilon_P(x, y)$	[·]	Eigen strain field
$\epsilon_T(x, y)$	[·]	Thermal strain field
$\epsilon_{\theta\theta}(r)$	[·]	Hoop strain field
$\epsilon_T(r, \theta)$	[·]	Transmission strain field
$T(\epsilon, \mathbf{x}_0, \hat{\mathbf{n}})$	[·]	Unattenuated linear transformation
$\epsilon_n(x, y)$	[·]	Strain field in the kernel of $T$

## Chapter 5

<b>Symbol</b>	<b>Units</b>	<b>Description</b>
$\epsilon_i$	[·]	Unique voxel strain tensor
$i$	[·]	Unique voxel index
$M$	[·]	Set of voxels intersect by a given ray
$\Delta L_i$	[·]	Irradiated length of voxel $i$
$N$	[·]	Number of irradiated voxels for a ray
$s_i$	[·]	Penetration distance at voxel $i$
$\alpha_i$	[m]	Path-length contribution to $\mathbf{A}$ matrix construction
$\mathbf{A}$	[·]	Internal Strain Method co-efficient matrix
$\mathbf{U}$	[·]	Singular Value Decomposition matrix
$\Sigma$	[·]	Diagonal singular values matrix
$\mathbf{V}$	[·]	Singular Value Decomposition matrix
$\beta_1 \dots \beta_n$	[·]	Linear combination co-efficients
$W_0$	[J/m <sup>2</sup> ]	Strain Energy density
$\mathbf{x}$	[·]	Quadratic programming unknowns vector
$\mathbf{H}$	[·]	Quadratic programming Hessian Matrix
$\mathbf{f}$	[·]	Quadratic programming co-efficient vector.

## Chapter 6

<b>Symbol</b>	<b>Units</b>	<b>Description</b>
$N$	[·]	Number of Projections taken
$I$	[1/m <sup>2</sup> ]	Incompatibility
$I_r$	[·]	Relative incompatibility



# Contents

<b>1 An Introduction to Neutron Strain Measurement Methods</b>	<b>1</b>
1.1 X-Ray and Neutron Diffraction Strain Measurements . . . . .	2
1.2 Computed Tomography (CT) . . . . .	7
1.3 Neutron Transmission Tomography . . . . .	9
<b>2 The Boundary Reconstruction Method</b>	<b>13</b>
2.1 Derivation: Boundary Deformation from Measured Average Strain . . . . .	14
2.2 Problem Discretisation . . . . .	17
2.2.1 Ray-boundary intersection through boundary nodes . . . . .	18
2.2.2 Intersection between boundary nodes . . . . .	19
2.2.3 Constructing a system of equations . . . . .	21
2.3 Discretised Problem Solution . . . . .	21
<b>3 Simulation and Analysis: The Boundary Reconstruction Method</b>	<b>25</b>
3.1 Measurement Simulation Environment . . . . .	25
3.1.1 Sample and Strain Field Characterisation . . . . .	26
3.1.2 Measurement Geometry Generation and Ray Intersection Location	26
3.1.3 Simulating Bragg-Edge Measurements . . . . .	27
3.2 Reconstruction Algorithm . . . . .	27
3.3 Case Study: Cantilevered Beam Problem . . . . .	28
3.3.1 Simulation Results: Ideal Measurements . . . . .	30
3.3.2 Simulation Results: Measurement Uncertainty . . . . .	32
3.3.3 Simulation Results: Ray Attenuation . . . . .	33
3.3.4 Simulation Results: Ray Width . . . . .	36
3.4 Conclusions . . . . .	38
<b>4 General Tomographic Reconstruction</b>	<b>41</b>
4.1 Prerequisite: Eigen Strains and Compatibility . . . . .	41
4.2 Literature Review: Previous Work . . . . .	43
4.2.1 <i>Feasibility study of neutron strain tomography</i> . . . . .	44
4.2.2 <i>Reconstruction of axisymmetric strain distributions via neutron strain tomography</i> . . . . .	44
4.2.3 <i>Bragg Edge Neutron Strain Tomography</i> . . . . .	45
4.2.4 <i>Neutron Strain Tomography using the Radon Transform</i> . . . . .	45
4.2.5 <i>Diffraction tomography of strain</i> . . . . .	46
4.3 Existence and Uniqueness, Problem Null Space . . . . .	47

<b>5 A New Approach: Internal Strain Method</b>	<b>49</b>
5.1 Non-Attenuated Measurement Model . . . . .	49
5.1.1 Euler (Riemann Sum) Integral Approximation. . . . .	52
5.1.2 Trapezoidal Integral Approximation . . . . .	53
5.2 Simulation and Analysis . . . . .	57
5.3 Additional Constraints . . . . .	58
5.3.1 Coupled Optimisation: Strain Energy Minimisation . . . . .	59
5.3.2 Null Space Characterisation via Singular Value Decomposition . . . . .	62
5.4 Conclusions . . . . .	64
<b>6 Attenuated Bragg-Edge Reconstruction</b>	<b>67</b>
6.1 Conceptual Introduction . . . . .	67
6.2 Problem Formulation . . . . .	68
6.3 Simulation and Analysis . . . . .	69
6.3.1 Reconstruction Results . . . . .	70
6.4 Error Field Compatibility . . . . .	74
6.4.1 Numerical Differentiation . . . . .	74
6.5 Reconstruction Results: Incompatible Strain Field . . . . .	78
6.5.1 Reconstruction Results: Experimental Nonideality . . . . .	81
6.6 Conclusions . . . . .	81
<b>7 Conclusions, Future Work</b>	<b>83</b>
<b>References</b>	<b>87</b>
<b>Appendices</b>	<b>89</b>
<b>A Turnitin Originality Report</b>	<b>91</b>
<b>B Boundary Reconstruction Paper</b>	<b>93</b>
<b>C General Tomographic Reconstruction Paper</b>	<b>101</b>

# List of Figures

1.1	Strain Gauges are commonly used in engineering to measure strains with high precision . . . . .	1
1.2	Incident radiation is reflected by a crystal lattice. . . . .	2
1.3	Experimental geometry for a neutron diffraction strain measurement. . . . .	3
1.4	While the neutron rays penetrate and interact with all crystals in their path, only those oriented such as to satisfy Bragg's Law produce the constructive interference that leads to the diffracted waves . . . . .	4
1.5	A characteristic diffraction peak is observed. Intensity is usually measured as a count of detected neutrons. . . . .	5
1.6	A medical CT scanner setup . . . . .	7
1.7	A magic square. Entries in each row, column and diagonal must add to the same number. CT reconstruction is a similar problem, but 3D, and the number to which a single direction must sum is not constant, but dependent on the amount of density encountered . . . . .	8
1.8	Incident and transmitted neutron intensity-wavelength distributions, and the transmission distribution showing characteristic Bragg-Edges . . . . .	10
1.9	General system co-ordinate system. . . . .	12
2.1	Since $\hat{\mathbf{n}}$ is a unit vector, its components are partial derivatives of the position vector $\mathbf{x}$ components with respect to the co-ordinate $s$ . . . . .	16
2.2	Sample Geometry and Nodal Boundary Deformations . . . . .	17
2.3	A ray intersects two nodes on the sample boundary. . . . .	18
2.4	The linear shape function $N(d)$ is used to relate deformation at an entry or exit point to the adjacent boundary nodes. . . . .	19
2.5	The solution states (a) $\Phi = [\phi_1 \dots \phi_7]^\top$ and (b) $\Phi + \phi_r$ fit the measurements equally well, since the reconstruction is invariant to rigid-body motions of the boundary. . . . .	23
3.1	The detector pixels and associated ray propagation vectors are rotated as projections are taken from different directions. . . . .	27
3.2	System free-body diagram. . . . .	29
3.3	Finite element solutions to the strain field. . . . .	30
3.4	Reconstructed principal strain distributions within the cantilevered beam. Original strain fields are black, reconstructed strain fields are red. . . . .	31
3.5	Uncertainty in reconstructed strains as a function of the number of projections taken and magnitude of measurement noise applied. . . . .	33
3.6	Relative error in reconstructed strains as a function of the number of projections taken and magnitude of attenuation applied. . . . .	34

3.7	Projection directions for (a) projections over $180^\circ$ and (b) over $360^\circ$ . . . . .	35
3.8	The $s - t$ co-ordinate system used for Ray-Width analysis. . . . .	36
3.9	A grid aligned with the local $s - t$ co-ordinate system is created to perform a surface integral. . . . .	37
3.10	A negligible increase in relative error was observed as the measurement ray width was increased. . . . .	38
4.1	Magic Squares representing the effect of null strain fields. . . . .	48
5.1	The elastic strain tensor field $\epsilon_E(x, y)$ is discretised into a number of finite elements — called <i>voxels</i> — each said to posses a constant strain tensor. . . . .	50
5.2	The integrand of a Bragg-Edge measurement is a scalar field, and the line integral measurement model essentially calculates the face area of a ‘fence’ formed between the $(x, y)$ plane and the field magnitude along the ray path. Euler (top left) and Trapezoidal (top right) approximations to the integral can be seen. . . . .	51
5.3	Each voxel intersected by the neutron ray has an associated irradiated length $\Delta L$ that is included in the sum argument. . . . .	52
5.4	The trapezoidal provides a discrete approximation to the integral of $f(x)$ . . . . .	54
5.5	A plane-stress element in a general loading scenario. . . . .	59
6.1	This fixed boundary strain field is in the kernel of Equation 1.8, meaning that any measurement of that form through this field (such as the one shown by the black arrow) will have zero magnitude. . . . .	67
6.2	Increasing the amount of attenuation changes the magnitude of a Bragg-Edge measurement significantly, preventing fixed-boundary strain fields lying in the null of the transform. . . . .	68
6.3	Convergence of the reconstruction algorithm was observed in the presence of attenuation. . . . .	70
6.4	Left: True and Reconstructed cantilevered beam $\epsilon_{xx}$ , $\epsilon_{xy}$ and $\epsilon_{yy}$ strain field components. Right: Reconstruction error fields . . . . .	71
6.5	Cumulative density function showing the relative magnitude of measurements through the reconstruction error fields to that of measurements through the sample strain field. . . . .	72
6.6	As the magnitude of attenuation is increased, the reconstruction error fields (right) undergo significant changes. . . . .	73
6.7	The numerical derivative algorithm developed works by fitting surfaces to localised segments of the strain field. . . . .	75
6.8	Relative Incompatibility of the cantilevered beam strain field. (a) True solution. (b) Solution found by central difference algorithm. (c) Solution found by curve-fitting. . . . .	76
6.9	Relative Incompatibility of the known-incompatible strain field. (a) True solution. (b) Solution found by central difference algorithm (clearly incorrect). (c) Solution found by curve-fitting. . . . .	79
6.10	Reconstruction of an incompatible strain field has been achieved in the presence of attenuation. . . . .	80

# Chapter 1

## An Introduction to Neutron Strain Measurement Methods

Every day, engineers and scientists rely on mathematical models of physical systems to better understand the world around us. In the past half-century, as computational capability has increased there has been widespread adoption of numerical computational models in the engineering industry. Take for instance computational *Finite Element models*, which have been used extensively by engineers to predict and analyse the stress and strain state in engineering designs [1]. In granular systems, mechanical engineers often utilise *Discrete Element models* to capture the ensemble behaviour of a bulk solid by characterising the interaction of individual particles. Mechatronics and Electrical engineers routinely characterise complex multi-domain problems using *state-space* models, which can then be utilised in the control of these systems.

Clearly, the calibration and validation of these mathematical models is of great importance in ensuring the accuracy of their predictions. In ascertaining the validity of results produced by Finite Element models of engineering designs, or discrete element models of particulate systems, confirmation of predicted stresses (or strains) within these bodies is often sought. A number of methods exist by which strain on the surface of a solid body can be measured. One such method is the well known and ubiquitous strain gauge — an electrical component which varies in resistance when under tension or compression, as shown in Figure 1.1.

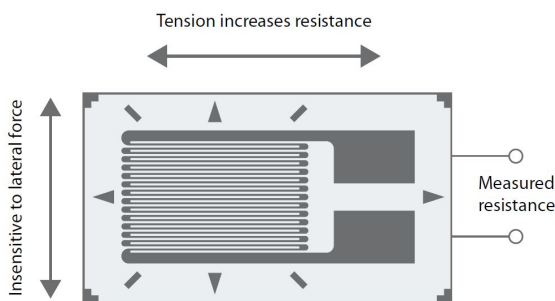


**Figure 1.1:** Strain Gauges are commonly used in engineering to measure strains with high precision [2].

When attempting to resolve the triaxial strain fields within solid bodies or granular systems, however, the only practical approach is to utilise neutron or X-ray diffraction. These methods offer an unrivalled level of detail that is of great value in the validation of finite or discrete element models. In this chapter, the nature of these diffraction methods, their limitations, and the motivation for this thesis will be discussed.

## 1.1 X-Ray and Neutron Diffraction Strain Measurements

In 1912, German physicist Max von Laue published a discovery which would later win him a Nobel prize and pioneer a field of research that remains active to this day [3]. Von Laue observed that X-rays propagating through the highly ordered structure of a crystalline material were subject to systematic interference. In the time since, the governing principles responsible for this interference have become the foundation for a range of scientific techniques.

One such technique is strain measurement in crystalline materials via neutron diffraction. As is the case with electromagnetic radiation (e.g, X-rays), corpuscular (particle) radiation experiences interference as it propagates through crystalline structures. In 1913, father and son William Lawrence and William Henry Bragg re-wrote Von Laue's equations, formalising the conditions under which this interference is constructive. Bragg's Law [4] specifies these conditions:

$$n\lambda = 2d \sin \theta \quad (1.1)$$

Where  $n\lambda$  is an integer multiple  $n$  of the wavelength  $\lambda$  of incident radiation,  $d$  the atomic lattice spacing of the polycrystalline sample and  $\theta$  the radiation angle of reflection with respect to the lattice plane. This process is illustrated in Figure 1.2, where two rays with identical wavelength and phase propagate through a crystal lattice. Here, the lower ray must travel an additional distance of  $2d \sin(\theta)$  than that above it. Bragg's Law specifies that *constructive* interference occurs only when this additional distance is an integer multiple  $n$  of the radiation wavelength  $\lambda$ .

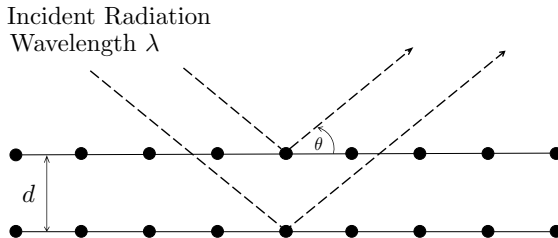


**Figure 1.2:** Incident radiation is reflected by a crystal lattice.

Intuitively, it can be seen that for a fixed atomic spacing, in order to satisfy Bragg's Law, the reflection angle  $\theta$  increases as the radiation wavelength  $\lambda$  is increased — up to a point. Consider an alternative form of [Equation 1.1](#):

$$\frac{n\lambda}{2d} = \sin \theta \quad (1.2)$$

Since  $\sin \theta$  can only produce values between -1 and 1, the wavelength of incident radiation  $\lambda$  can at most be equal to twice the atomic lattice spacing. For any value of  $\lambda$  greater than this, known as the *Bragg cut-off*, Bragg's Law cannot be satisfied, and constructive interference is not possible. In this case, the parallel waves shown in [Figure 1.2](#) will *destructively* interfere, and no diffraction will be observed.

Of course, this condition on constructive interference raises the prospect of exploiting Bragg's Law to measure the atomic lattice spacing of a polycrystalline sample. In fact, this concept forms the basis of neutron diffraction strain measurement methods, which we will now discuss with respect to the experimental geometry shown in [Figure 1.3](#).

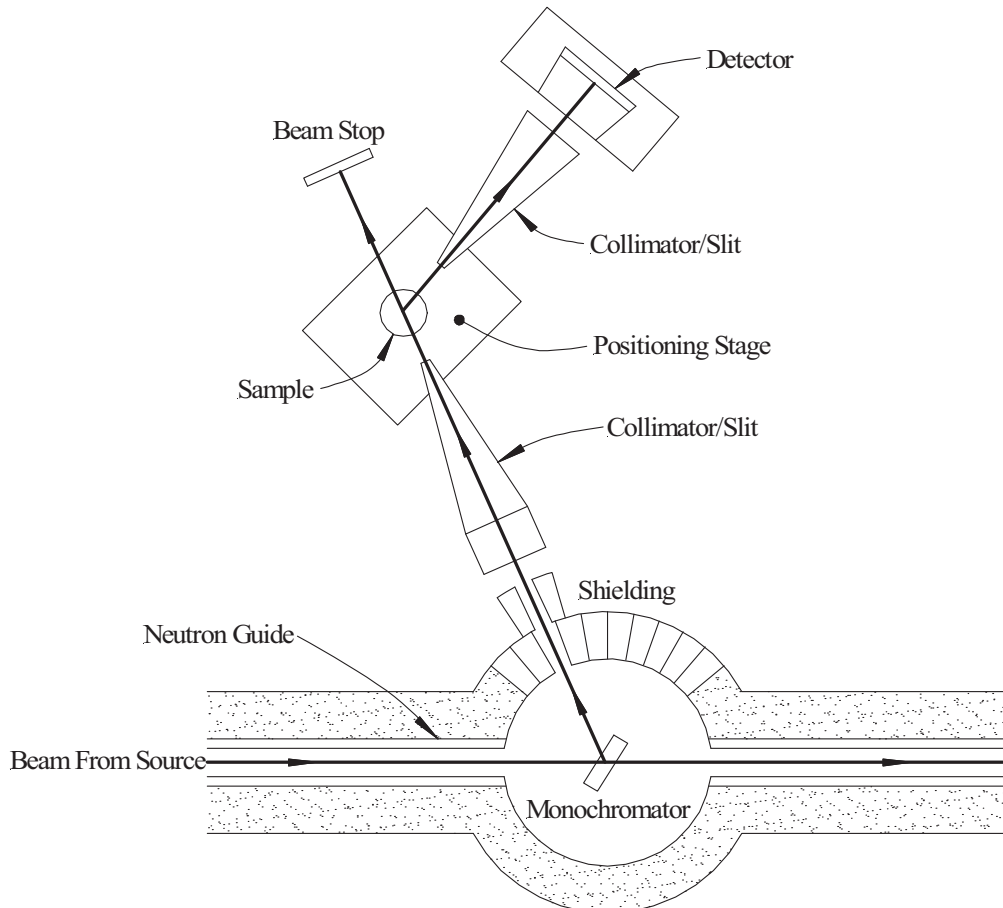


**Figure 1.3:** Experimental geometry for a neutron diffraction strain measurement. [5]

A simplification of the process is as follows:

1. Neutrons with a spectrum of wavelengths are generated at a neutron source (usually a nuclear reactor).
2. A monochromator (typically constructed of single-crystal Copper, Silicon, Beryllium, Carbon, Germanium or Silicon) is used to isolate and redirect neutrons of a specific wavelength toward the crystalline sample to be studied.
3. A collimator (and/or slit) is used to reduce these neutrons into a fixed-size beam of parallel rays.
4. This beam of (known) constant wavelength neutrons irradiates the crystalline sample to be studied.
5. These neutrons interact with the crystal structure as they penetrate the sample, according to the scattering cross-section of the atoms, causing interference.
6. Some rays interact with the structure and do not satisfy Bragg's Law — these destructively interfere. Others do not interact and are transmitted. In both cases, these neutrons have no impact on a diffraction measurement.
7. Other rays, which have constructively interacted with the correctly oriented crystals (as per [Figure 1.4](#)) are reflected outward from the sample. A second collimator is positioned such that only neutrons diffracted within a particular gauge volume within the sample are observed.
8. These neutrons strike a detector, which records their intensity and position.

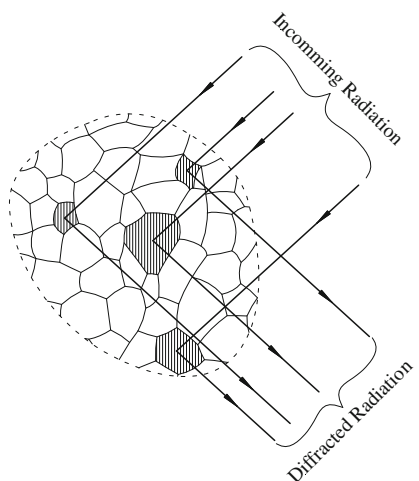


**Figure 1.4:** While the neutron rays penetrate and interact with all crystals in their path, only those oriented such as to satisfy Bragg's Law produce the constructive interference that leads to the diffracted waves [6].

The neutron detector measures the intensity of diffracted neutrons as a function of the scattering angle, which is trigonometrically calculated from the known positions of the detector and sample. A plot of intensity against scattering angle is usually constructed, such as that shown in [Figure 1.5](#). For a set of correctly oriented crystal planes, a characteristic ‘diffraction peak’ of intensity where Bragg’s Law has been satisfied is observed. While this peak should theoretically be infinitesimally thin (i.e: a Dirac delta function occurring at the value of  $\theta$  that satisfies Bragg’s Law), what is instead observed is a diffraction peak of finite width.

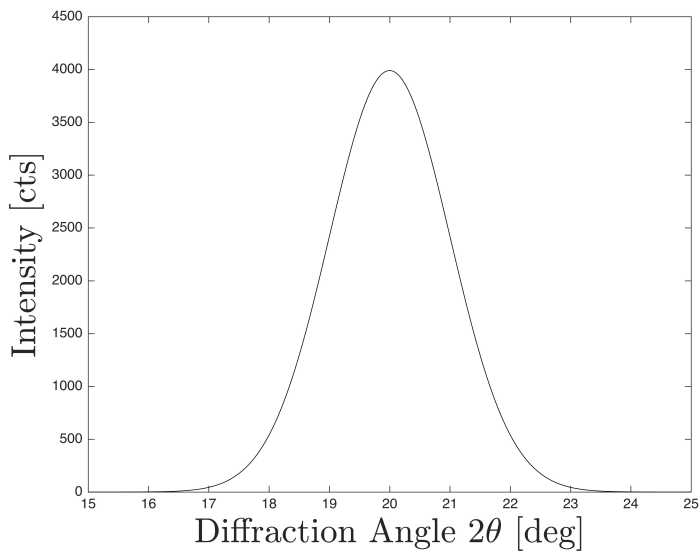


**Figure 1.5:** A characteristic diffraction peak is observed. Intensity is usually measured as a count of detected neutrons.

Peak width is due to nonidealities in the sample and experimental setup, such as:

1. Internal (Type II and III) stresses within the grains [\[7\]](#).
2. Mozaic spread (non-straightness of the atomic planes) and curvature of the monochromator, which permits a range of transmitted wavelengths [\[8\]](#).
3. Mozaic spread in the atomic planes of the sample.
4. Broadening due to smaller encountered grains [\[9\]](#).

These nonidealities will not be discussed in detail. The interested reader is directed to the relevant literature referenced above. Obviously, the controllable experimental nonidealities are minimised as much as possible to preserve the precision of the peak position.

The use of dual collimators to limit the effective neutron ray size and placement of the detector allows for fine-tuning the gauge volume of the sample from which the detected neutrons have emanated. This gauge volume can be made larger or smaller by adjusting

the aperture of the collimators, and the sample can be translated or rotated to change its position. In other words, arbitrarily sized cubic volumes of the sample can be probed, and only neutrons that have been diffracted from within this volume will contribute to a measurement.

The key result for this project is that the scattering angle corresponding to the diffraction peak and the known (nominal) source neutron wavelength can be used with Bragg's Law to determine the average atomic lattice spacing of correctly oriented crystals within the gauge volume. In other words, the crystals are themselves acting as internal strain gauges!

In determining strain, two measurements are taken: an initial lattice spacing  $d_0$ , from an unstrained sample, and a spacing measurement  $d$ , from a strained sample. From this, an average strain can be determined:

$$y = \frac{d - d_0}{d_0}. \quad (1.3)$$

The caveat here is that this measured strain is in a direction normal to the diffracting atomic planes. In other words, the direction bisecting the incident and diffracted radiation (*not* the direction of transmission or reflection).

By rotating the sample, the atomic lattice spacing (and thus strain) in other directions can be measured also. In fact, if at least three measurements are taken from different directions, the average complete strain tensor for a 2D gauge volume can be reconstructed (since there are three unique elements in the 2D strain tensor) [6].

If the strain at only one position is required, great — the job is complete. However, the limitations of our method are clear: only the average strain tensor over a discrete, representative volume can be measured.

To conduct a more thorough investigation, one may wish to reconstruct the *entire* strain field within a sample. Such a reconstruction is said to be *tomographic*. Tomography (from the Greek words *Tomos*, meaning *slice*, and *Graphe*, meaning *drawing*) is a blanket term for any method by which superposition-free information about the internal structures of a solid object can be produced [10].

Strain field tomography has (in one sense) been achieved previously by discretising a sample into cubic elements, and sweeping a gauge volume of fixed size over the sample, probing each element individually using diffraction techniques. To achieve tomography in this way, many measurements have to be made, requiring accurate and precise movement of the sample to many different positions. While currently the only tool available, diffraction methods can be a time consuming and cumbersome means to this end. With limited access to neutron sources and instruments, experimental time is valuable and it is often unreasonable to map out an entire sample.

At this stage, we will conclude our (brief) foray into strain measurement by neutron diffraction. It should be noted that a number of simplifications have been made in the description provided here, and that the interested reader is encouraged to consult [9] for a more thorough explanation. While conventional diffraction is not a time-effective means to achieve full-field tomographic reconstruction, a method that draws inspiration from medical science has recently reached maturity and shows promise in achieving strain tomography.

## 1.2 Computed Tomography (CT)

Computed Tomographic (CT) Imaging, also known as CAT (Computerised Axial Tomography) scanning, produces cross-sectional images of 3D bodies, as opposed to the 2D projections obtained by conventional X-ray radiography.

In medicine, CT scanning is used to obtain a cross sectional image of the human body. Mathematically speaking, CT algorithms are actually working to map a three dimensional scalar field - analogous to density. The patient (a 3D scalar density field) is positioned within a mechanised ring. One side of the ring hosts an X-ray source, and the opposite side a detector, such as in [Figure 1.6](#).

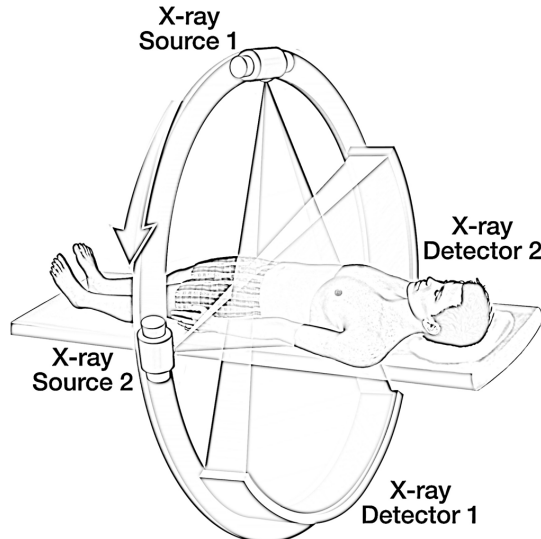


**Figure 1.6:** A medical CT scanner setup [11].

The CT machine projects X-rays from a radioactive source, which then propagate through the body (a 3D scalar density field) and towards the detector. The intensity-wavelength distribution of the source X-rays is known, and this is compared with the distribution measured at the detector. Rays which have propagated through the body are attenuated compared to the source distribution, and this attenuation is related to the total density encountered by a ray.

The detector used is pixelated, meaning that in any one arrangement of the apparatus, many source X-rays can be projected through the body and detected on the other side. In the sequel, we will call each of these detections a measurement. Many measurements can be made from any one arrangement of the apparatus (which we will call a projection). The advantage of the setup shown in [Figure 1.6](#) is that two orthogonal projections can be made in any one arrangement of the apparatus to speed up measurement time [\[12\]](#).

Each single measurement is one piece of the puzzle. After a projection in one arrangement, the apparatus is then rotated relative to the body (scalar field), where another projection (consisting of many more measurements) is taken. This process is repeated through many angles, and the data is fed back to a computer, where a density field is chosen to fit the attenuation data from *all measurements*.

The problem can be thought of like a giant magic square, such as that shown in [Figure 1.7](#). The relationship between attenuation and density is known, and the amount of attenuation in *many single* directions is known. The problem comes in assigning densities to each discretised element of the body so that the right amount of attenuation is present in that one direction, *and* all the other directions. It's like having a completely blank magic square, but knowing the sums of all the numbers in many random directions, and having to fill in the blanks.

2	7	6	$\rightarrow 15$
9	5	1	$\rightarrow 15$
4	3	8	$\rightarrow 15$
15	15	15	15
			15

**Figure 1.7:** A magic square. Entries in each row, column and diagonal must add to the same number. CT reconstruction is a similar problem, but 3D, and the number to which a single direction must sum is not constant, but dependent on the amount of density encountered [\[13\]](#).

Since there are often many more measurements than unknowns, the problem is over-determined. Obviously, there are better and worse fields which can be chosen. The best selection is a field which minimises the error across all measurements – this is often achieved in a least squares sense. Because a continuum is being discretised, and experimental noise introduced, there is never an error-free solution. This is one of the reasons radiographers ask you to keep still during a CT scan! Every movement introduces further error into the measurements and makes it harder for the reconstruction algorithm to select a field which fits the attenuation data well.

In general, the more projections that are taken, the more accurate the reconstructed field will be. In medical CT, a method known as linear back projection aids in the reconstruction process, allowing for increasingly accurate partial reconstructions of the density field. In other words, even with very few measurements, a (far less accurate) reconstruction can be generated [14].

### 1.3 Neutron Transmission Tomography

Equipped with a (very basic) understanding of CT, let us now turn our attention back to the problem at hand: reconstruction of the full *strain tensor* field at every point within a sample:

$$\boldsymbol{\epsilon}(x, y, z) = \begin{bmatrix} \epsilon_{xx} & \epsilon_{xy} & \epsilon_{xz} \\ \epsilon_{yx} & \epsilon_{yy} & \epsilon_{yz} \\ \epsilon_{zx} & \epsilon_{zy} & \epsilon_{zz} \end{bmatrix}. \quad (1.4)$$

In the interests of maintaining simplicity, for the remainder of the thesis, we will exclusively consider the 2D case, where:

$$\boldsymbol{\epsilon}(x, y) = \begin{bmatrix} \epsilon_{xx} & \epsilon_{xy} \\ \epsilon_{yx} & \epsilon_{yy} \end{bmatrix}. \quad (1.5)$$

Of course, the end goal is to compare this reconstructed strain field with finite or discrete element predictions and perform some sort of model validation.

This problem shares many similarities with conventional medical CT, however, there is a significant difference: instead of reconstructing a scalar field as in medicine, our goal is to reconstruct a tensor field, with 4 components (3 of which are unique if the symmetry of the strain tensor is exploited). Thankfully, a class of *Neutron Transmission* strain measurement methods have recently shown promise in the reconstruction of these tensor fields.

These methods are like a middle ground between the diffraction and CT methods previously discussed. The outcome of a transmission measurement is still an average strain  $y$ , but the benefit is that like CT, many measurements can be made per projection, and (conveniently), the measured strain is in the direction of ray propagation.

Unlike diffraction, an entire spectral distribution of neutrons is utilised in transmission measurements, and so the method of production is slightly different. To produce the spectra of neutrons at the intensity required for transmission measurements, protons first are accelerated to near-light speeds in a particle accelerator, such as that at the ISIS neutron source in Europe, or at the J-PARC source in Japan.

These protons are then directed into a heavy metal *target* – usually depleted Uranium, Tantalum or Mercury – using a switching electromagnet. Collision of the protons into the nuclei of the heavy metal atoms results in spallation, and the heavy metal nuclei are decomposed. In the process, several neutrons are liberated from the nucleus and collimators are used to direct these toward the sample [15].

These free neutrons are transmitted in packets (by switching the electromagnet on and off many times per second – typically at 50 Hz). Neutrons have wave-like properties, with characteristic wavelengths that are related to their velocity. During Bragg-Edge strain measurement, a known characteristic incident intensity-wavelength distribution is produced — see, for example that on the left hand side of Figure 1.8. This distribution means that the neutrons spread out as they travel between the source and detector, with the fastest neutrons arriving first. By measuring the neutron time of flight (TOF) across the (known) distance between the source and detector, and calculating from the measured neutron velocity an associated wavelength, the wavelength-intensity distribution at the *detector* can be determined (such as that in the centre of Figure 1.8).

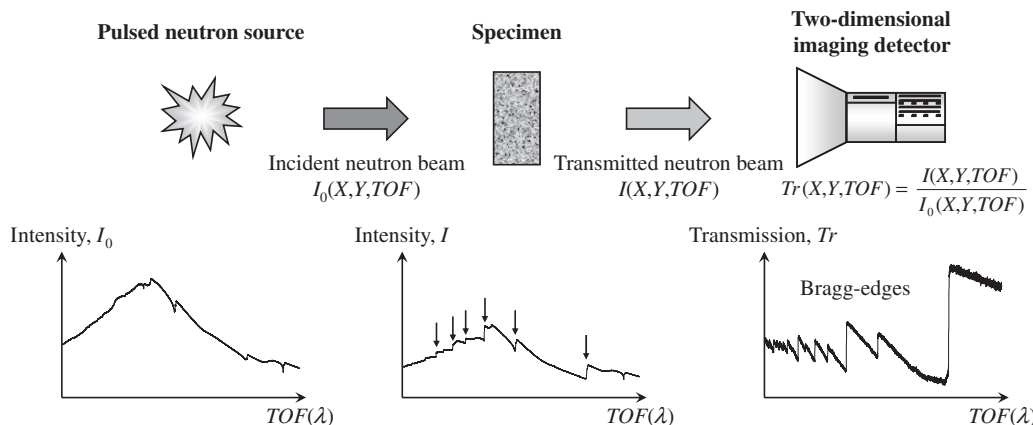


**Figure 1.8:** Incident and transmitted neutron intensity-wavelength distributions, and the transmission distribution showing characteristic Bragg-Edges [16].

When these neutrons impact and penetrate the sample, they interact with the crystal structure and are either transmitted or diffracted constructively according to Bragg's Law. Diffraction of neutrons results in an intensity loss measured at the detector (compared to the source). If the relative transmission of neutrons is observed as a function of wavelength (the right hand image of Figure 1.8), abrupt discontinuities in transmission can be seen at wavelengths corresponding to the peaks previously seen in diffraction.

These discontinuities occur at wavelengths associated with the phenomenon known as *backscattering*. Recall that for a fixed atomic lattice spacing, the constructive diffraction angle  $\theta$  will increase with increasing radiation wavelength  $\lambda$  until  $\lambda/2d = 1$ , where  $\theta = 90^\circ$  and a ray is diffracted back toward the source.

After this critical wavelength is reached, no further constructive diffraction for that atomic spacing can occur, and a sudden jump in transmitted intensity is observed. These discontinuities in transmitted intensity are known as Bragg-Edges. In a similar vein to diffraction, the wavelength associated with these edges provides information about the atomic spacing of the sample  $d$ . As with diffraction peaks, several edges will be observed for a transmission measurement, and for simplicity, care must be taken to ensure that the edge being tracked corresponds to a set of lattice planes that closely model the ensemble average behaviour of the sample [6].

As before, an unstrained sample is measured first, giving an atomic spacing measurement for all accessible planes  $d_0$ . Then, applying an elastic strain, another measurement  $d$  is made. The Bragg-Edges are observed to shift by a wavelength  $\Delta\lambda$  proportional to the change in lattice spacing:

$$\Delta\lambda = 2(d - d_0). \quad (1.6)$$

Unlike with diffraction, the average strain *in the direction of transmission* can be calculated:

$$y = \frac{d - d_0}{d_0} = \frac{\Delta\lambda}{2d_0}. \quad (1.7)$$

Developing approaches that aim to utilise these average strain measurements en masse to reconstruct the tensor field within a sample forms the objective of this thesis. In all cases, the methodology begins with an alternative formulation of the average strain. Referencing the co-ordinate system shown in Figure 1.9, the average strain within a body as measured by Bragg-Edge neutron transmission can be idealised as a line integral [17] of the form:

$$y = \frac{1}{L} \int_0^L \hat{\mathbf{n}}^\top \boldsymbol{\epsilon}(\mathbf{x}_0 + s\hat{\mathbf{n}}) \hat{\mathbf{n}} \, ds \quad (1.8)$$

which captures the component of strain along the line  $s$  that is in the direction of  $\hat{\mathbf{n}}$ . In the following chapters, two such approaches will be discussed. We will discover that in general, the nature of our measurements precludes the existence of a unique solution, and we will discuss two methods by which additional problem constraints can force uniqueness.

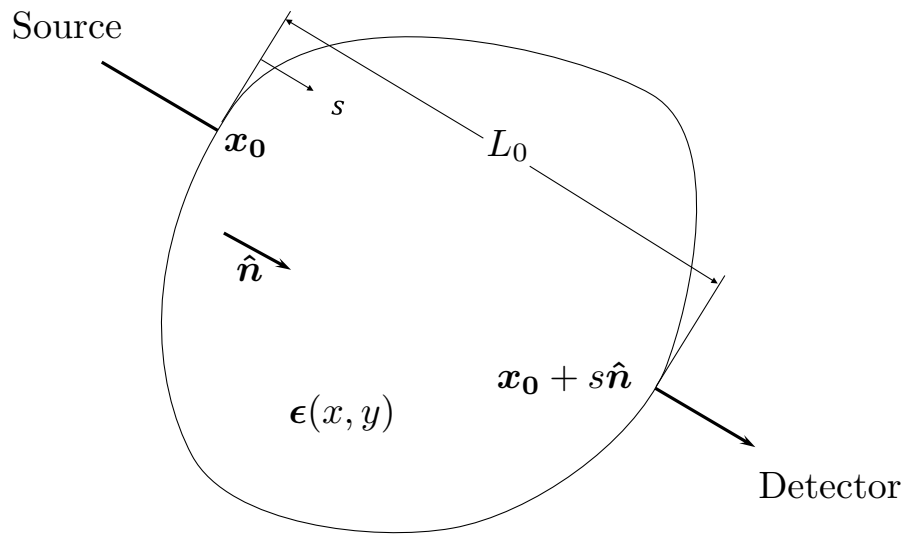


**Figure 1.9:** General system co-ordinate system.

## Chapter 2

# The Boundary Reconstruction Method

In the previous chapter, it was discussed how neutron transmission methods could be used to measure the average strain  $y$  in the direction of a given ray. In this chapter, we will discuss the use of these measurements in the tomographic reconstruction of tensor strain fields under a number of limiting assumptions:

**Assumption 2.1.** *In all cases, two dimensional (2D) strain fields will be considered. Symmetry of the strain tensor will be exploited, such that the strain tensor field to be reconstructed can be thought of as three unknown scalar fields.*

**Assumption 2.2.** *We will assume that the samples under examination are subject only to in-situ loadings — that is, boundary tractions. Specifically, this means that any strain field under examination must be free of plastic strains, thermal strains, or body forces.*

[Assumption 2.1](#) has only been made for the sake of simplicity. There is nothing *physical* precluding the extension of the work undertaken in this chapter (and in the remainder of the thesis) to a 3D case. To limit complexity, however, from here on out the 2D case will be exclusively discussed.

[Assumption 2.2](#) is more forbidding, and indicative of an underlying limitation of our method. An appreciation of this limitation requires a deeper understanding of the reconstruction problem. Rather than immediately delve into the intricacies of the general problem, in this chapter, we will first see how under these limiting assumptions tomographic reconstruction of an unknown strain field within a body can be conducted. After working through this case study, we will extend our knowledge to the general case, and draw upon available literature to formulate a more practical approach.

A useful consequence of [Assumption 2.2](#) is that under these conditions, the deformation of the boundary of a body uniquely defines the strain field within [18]. As the name suggests, the boundary reconstruction method takes advantage of this condition to reduce the tensor field reconstruction problem to a boundary deformation reconstruction problem. In other words, if the deformation of a sample boundary can be reconstructed, determination of the strain field within is a trivial matter. Practically, this is achieved

by utilising the boundary deformation as a Dirichlet condition and either resolving the strain field analytically, or solving the governing partial differential equations via a finite element approach.

## 2.1 Derivation: Boundary Deformation from Measured Average Strain

In this section, a relationship between measured average strain and the deformation of the boundary at the ray entry and exit will be derived. In an attempt to be as thorough as possible in the derivation, we will skip as few steps as possible. A reader uninterested in this derivation is encouraged to skip ahead to the following section.

We will repeatedly reference the sample and co-ordinate system previously shown in Figure 1.9. At the end of [chapter 1](#), we identified that a Bragg-Edge measurement could be idealised as a line integral:

$$y = \frac{1}{L} \int_0^L \hat{\mathbf{n}}^\top \boldsymbol{\epsilon}(\mathbf{x}_0 + s\hat{\mathbf{n}}) \hat{\mathbf{n}} \, ds. \quad (1.8 \text{ revisited})$$

This idealisation makes use of the following assumptions:

**Assumption 2.3.** *Neutron rays are infinitesimally thin.*

**Assumption 2.4.** *Neutron rays are not attenuated as they pass through a sample.*

The validity of these assumptions will be evaluated in [chapter 3](#). To begin our formulation, recall that the total strain field within a body (here, only an elastic component due to [Assumption 2.2](#)) can be written as the gradient of a deformation field. Say that such a deformation vector field  $\phi(x, y)$  exists within the sample, with components:

$$\phi(x, y) = \begin{bmatrix} u \\ v \end{bmatrix} \quad (2.1)$$

Where  $u = u(x, y)$  and  $v = v(x, y)$  are scalar fields. A *displacement gradient tensor*  $\mathbf{H}$  can be formulated:

$$\begin{aligned}
\mathbf{H} &= \nabla \phi^\top \\
&= \begin{bmatrix} \frac{\partial}{\partial x} & \frac{\partial}{\partial y} \end{bmatrix} \begin{bmatrix} u \\ v \end{bmatrix}^\top \\
&= \begin{bmatrix} \frac{\partial u}{\partial x} & \frac{\partial u}{\partial y} \\ \frac{\partial v}{\partial x} & \frac{\partial v}{\partial y} \end{bmatrix}.
\end{aligned}$$

The strain tensor field  $\boldsymbol{\epsilon}(x, y)$  can be written as a function of  $\mathbf{H}$ :

$$\boldsymbol{\epsilon}(x, y) = \frac{1}{2}(\mathbf{H} + \mathbf{H}^\top). \quad (2.2)$$

Where the displacement gradient tensor  $\mathbf{H} = \mathbf{H}(x, y)$  is itself a field. Substituting [Equation 2.2](#) into [Equation 1.8](#):

$$\begin{aligned}
\frac{1}{L} \int_0^L \hat{\mathbf{n}}^\top \boldsymbol{\epsilon}(\mathbf{x}_0 + s\hat{\mathbf{n}}) \hat{\mathbf{n}} \, ds &= \frac{1}{L} \int_0^L \hat{\mathbf{n}}^\top \left( \frac{1}{2} (\mathbf{H} + \mathbf{H}^\top) \right) \hat{\mathbf{n}} \, ds \\
&= \frac{1}{2L} \int_0^L (\hat{\mathbf{n}}^\top \mathbf{H} + \hat{\mathbf{n}}^\top \mathbf{H}^\top) \hat{\mathbf{n}} \, ds
\end{aligned} \quad (2.3)$$

Further, recalling [Figure 1.9](#), the *unit* vector  $\hat{\mathbf{n}}$  can be written in terms of the co-ordinate system by:

$$\begin{aligned}
\hat{\mathbf{n}} &= \frac{d}{ds} \begin{bmatrix} x \\ y \end{bmatrix} \\
&= \begin{bmatrix} \frac{dx}{ds} \\ \frac{dy}{ds} \end{bmatrix}.
\end{aligned} \quad (2.4)$$

This is not obvious at first. To aid our understanding, consider [Figure 2.1](#). The co-ordinate  $s$  points in the direction of the unit vector  $\hat{\mathbf{n}}$ , meaning that at its tip,  $s = 1$ .

Next, identify that  $dx/ds$  represents the change in the co-ordinate  $x$  for a *unit* change in  $s$ . Visually, this is like walking along the  $s$  axis one unit, and measuring that change in the  $x$  co-ordinate of  $\mathbf{x}$ . Since  $\hat{\mathbf{n}}$  is a unit vector, with tip at  $s = 1$ , this rate of change is simply equal to the  $x$  component of  $\hat{\mathbf{n}}$ . A similar formulation follows for the  $y$  co-ordinate.

Substituting [Equation 2.4](#) into [Equation 2.3](#):

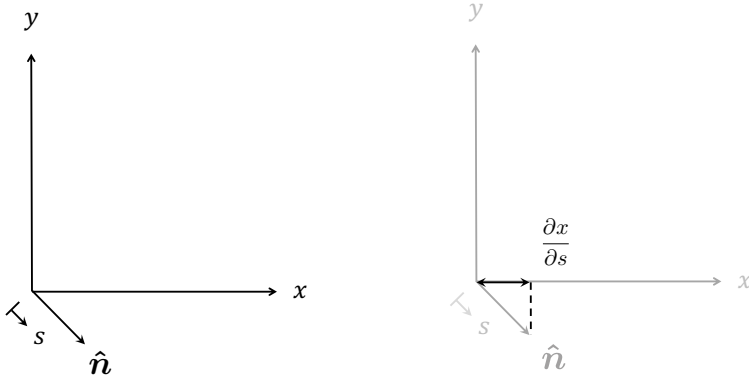


**Figure 2.1:** Since  $\hat{\mathbf{n}}$  is a unit vector, its components are partial derivatives of the position vector  $\mathbf{x}$  components with respect to the co-ordinate  $s$ .

$$\begin{aligned}
 \frac{1}{2L} \int_0^L (\hat{\mathbf{n}}^\top \mathbf{H} + \hat{\mathbf{n}}^\top \mathbf{H}^\top) \hat{\mathbf{n}} \, ds &= \frac{1}{2L} \int_0^L \left( \begin{bmatrix} \frac{dx}{ds} & \frac{dy}{ds} \end{bmatrix} \begin{bmatrix} \frac{\partial u}{\partial x} & \frac{\partial u}{\partial y} \\ \frac{\partial v}{\partial x} & \frac{\partial v}{\partial y} \end{bmatrix} + \begin{bmatrix} \frac{dx}{ds} & \frac{dy}{ds} \end{bmatrix} \begin{bmatrix} \frac{\partial u}{\partial x} & \frac{\partial u}{\partial y} \\ \frac{\partial v}{\partial x} & \frac{\partial v}{\partial y} \end{bmatrix}^\top \right) \begin{bmatrix} \frac{dx}{ds} \\ \frac{dy}{ds} \end{bmatrix} \, ds \\
 &= \frac{1}{2L} \int_0^L \left( \begin{bmatrix} \frac{dx}{ds} & \frac{dy}{ds} \end{bmatrix} \begin{bmatrix} \frac{\partial u}{\partial x} & \frac{\partial u}{\partial y} \\ \frac{\partial v}{\partial x} & \frac{\partial v}{\partial y} \end{bmatrix} + \begin{bmatrix} \frac{dx}{ds} & \frac{dy}{ds} \end{bmatrix} \begin{bmatrix} \frac{\partial u}{\partial x} & \frac{\partial v}{\partial x} \\ \frac{\partial u}{\partial y} & \frac{\partial v}{\partial y} \end{bmatrix} \right) \begin{bmatrix} \frac{dx}{ds} \\ \frac{dy}{ds} \end{bmatrix} \, ds \\
 &= \frac{1}{2L} \int_0^L 2 \left[ \frac{dx}{ds} \frac{\partial u}{\partial x} + \frac{dy}{ds} \left( \frac{\partial v}{\partial x} + \frac{\partial v}{\partial y} \right) - \frac{dy}{ds} \frac{\partial v}{\partial y} + \frac{dx}{ds} \left( \frac{\partial u}{\partial y} + \frac{\partial v}{\partial x} \right) \right] \begin{bmatrix} \frac{dx}{ds} \\ \frac{dy}{ds} \end{bmatrix} \, ds.
 \end{aligned}$$

Expanding, and applying the partial derivative chain rule yields:

$$\begin{aligned}
 &\frac{1}{2L} \int_0^L \left( \left( \frac{\partial u dx}{ds^2} + \frac{\partial v dy}{ds^2} \right) + \left( \frac{\partial u dx}{ds^2} + \frac{\partial v dy}{ds^2} \right) \right) \, ds \\
 &= \frac{1}{L} \int_0^L \left( \frac{\partial u dx}{ds^2} + \frac{\partial v dy}{ds^2} \right) \, ds \\
 &= \frac{1}{L} \int_0^L \partial u \frac{dx}{ds} + \partial v \frac{dy}{ds} \\
 &= \frac{1}{L} \int_0^L \begin{bmatrix} \frac{dx}{ds} & \frac{dy}{ds} \end{bmatrix} \begin{bmatrix} \partial u \\ \partial v \end{bmatrix} \, ds \\
 &= \frac{1}{L} \int_0^L \hat{\mathbf{n}}^\top d\phi.
 \end{aligned}$$

Performing the integral:

$$\begin{aligned}\frac{1}{L} \int_0^L \hat{\mathbf{n}}^\top \partial \phi &= \frac{1}{L} \left[ \hat{\mathbf{n}}^\top \phi(\mathbf{x}_0 + s\hat{\mathbf{n}}) \right]_0^L \\ &= \frac{1}{L} \left[ \hat{\mathbf{n}}^\top \phi(\mathbf{x}_0 + L\hat{\mathbf{n}}) \right] - \left[ \hat{\mathbf{n}}^\top \phi(\mathbf{x}_0) \right].\end{aligned}$$

Define the deformation of the ray exit point (on the sample boundary) as  $\phi_q = \phi(\mathbf{x}_0 + L\hat{\mathbf{n}})$  and the entry point as  $\phi_p = \phi(\mathbf{x}_0)$ . Then:

$$y = \frac{1}{L} \hat{\mathbf{n}}^\top (\phi_q - \phi_p). \quad (2.5)$$

The physical meaning behind [Equation 2.5](#) is not inherently obvious. Essentially, it states that under assumptions [2.1](#) and [2.2](#), a Bragg-Edge measurement  $y$  is intimately linked to the difference in deformation at the entry  $\phi_p$  and exit  $\phi_q$ . This concept is highlighted in [Figure 2.2](#), where these magnitudes are the lengths of the deformation vector projections  $\hat{\mathbf{n}}^\top \phi_p$  and  $\hat{\mathbf{n}}^\top \phi_q$ .

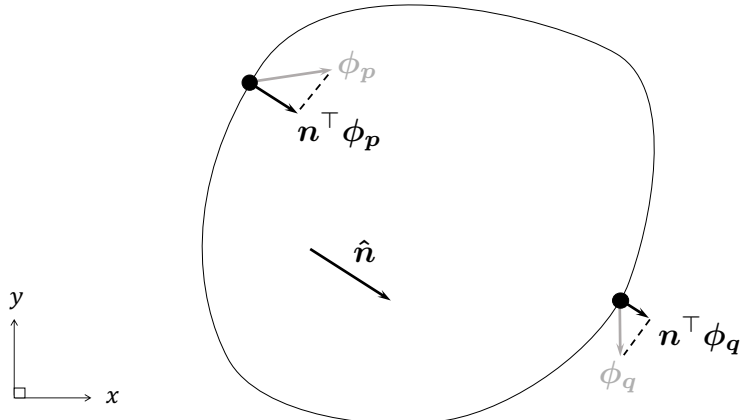


**Figure 2.2:** Sample Geometry and Nodal Boundary Deformations

With this result, the derivation is concluded.

## 2.2 Problem Discretisation

When the boundary of the sample is discretised, a system of equations (each of the form of [Equation 2.5](#)) can be constructed. This discretised problem can then be solved, provided that at least as many equations (measurements) are generated as there are unknown boundary deformations.

In this section, we will discuss how to generate such a system, and the nature of the equations involved. We will consider both the case where a ray passes directly through prescribed boundary nodes, and the case where a ray passes between nodes.

### 2.2.1 Ray-boundary intersection through boundary nodes

Let us initially consider the special case where a ray with unit direction vector  $\hat{\mathbf{n}}$  penetrates a sample under study, entering and exiting at prescribed nodes  $a$  and  $b$  respectively as per [Figure 2.3](#).

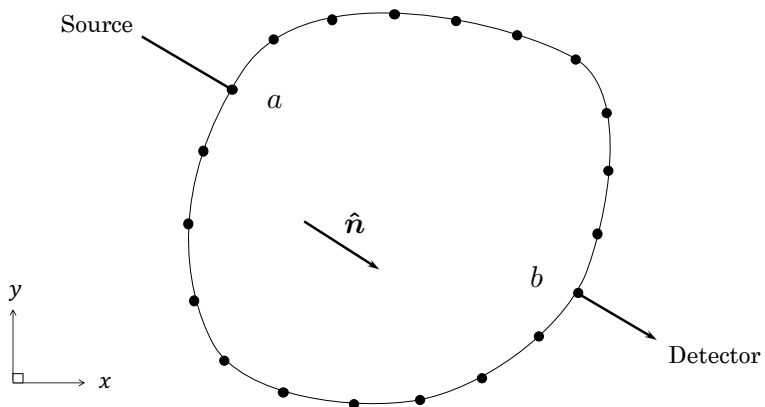


**Figure 2.3:** A ray intersects two nodes on the sample boundary.

Let the deformation of the sample boundary at nodes  $a$  and  $b$  be characterised by the vectors  $\phi_a$  and  $\phi_b$  respectively, each with a  $u$  and  $v$  component. Then, a Bragg-Edge measurement along this ray will be of the form of [Equation 2.5](#), with  $p = a$  and  $q = b$ .

$$y = \frac{1}{L} \hat{\mathbf{n}}^\top (\phi_q - \phi_p) = \frac{1}{L} \hat{\mathbf{n}}^\top (\phi_b - \phi_a) \quad (2.6)$$

Expanding:

$$\begin{aligned} \frac{1}{L} \hat{\mathbf{n}}^\top (\phi_b - \phi_a) &= \frac{1}{L} \begin{bmatrix} n_x & n_y \end{bmatrix} \left( \begin{bmatrix} u_b \\ v_b \end{bmatrix} - \begin{bmatrix} u_a \\ v_a \end{bmatrix} \right) \\ &= \frac{1}{L} \begin{bmatrix} n_x & n_y \end{bmatrix} \begin{bmatrix} u_b - u_a \\ v_b - v_a \end{bmatrix} \\ &= \frac{1}{L} (n_x(u_b - u_a) + n_y(v_b - v_a)) \\ &= \frac{1}{L} (n_x u_b - n_x u_a + n_y v_b - n_y v_a) \end{aligned}$$

$$= \frac{1}{L} \left( \begin{bmatrix} n_x & n_y & -n_x & -n_y \end{bmatrix} \begin{bmatrix} u_b \\ v_b \\ u_a \\ v_a \end{bmatrix} \right).$$

This form of the equation is particularly useful, relating the unknown quantities (the boundary deformation components  $u_b$ ,  $v_b$ ,  $u_a$  and  $v_a$ ) to the (known) components of the ray propagation direction vector  $n_x$  and  $n_y$ , and the irradiated length  $L$ . This equation would form one of the system of equations to be solved (in other words, one row in a co-efficient matrix).

### 2.2.2 Intersection between boundary nodes

The formulation for the case where a ray intersects the sample boundary between prescribed nodes is slightly more involved. Naturally, the simplest approach is to use linear shape functions to relate the deformations of the nodes immediately adjacent to the points of intersection  $p$  and  $q$ . Consider a ray with entry that intersects the boundary at some distance  $d$  between two prescribed nodes,  $a_1$  and  $a_2$ , such as in [Figure 2.4](#).

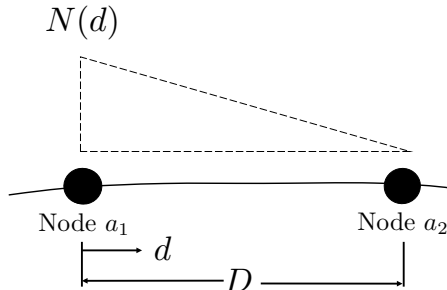


**Figure 2.4:** The linear shape function  $N(d)$  is used to relate deformation at an entry or exit point to the adjacent boundary nodes.

The linear shape function  $N(d)$  describes how the components of the deformation vector at the point of intersection  $u_p$  and  $v_p$  are related to the components of deformation in the adjacent nodes. The co-ordinate  $d$  is used to describe the position of the intersect relative to the first node. The length  $D$  denotes the total distance between the two adjacent boundary nodes. This formulation must be made in both the  $x$  and  $y$  directions, and in both cases,

$$N(d) = \frac{D - d}{D} \tag{2.7}$$

Such that:

$$u_p = N(d_x)u_{a_1} + (1 - N(d_x))u_{a_2} \quad (2.8)$$

and

$$v_p = N(d_y)v_{a_1} + (1 - N(d_y))v_{a_2}. \quad (2.9)$$

A similar formulation is made at the exit. Now let us consider the general case, where a ray is to intersect the boundary between prescribes nodes  $a_1$  and  $a_2$  at the entry, and  $b_1$  and  $b_2$  at the exit. Say the ray intersects between nodes  $a_1$  and  $a_2$  such that  $N(d_x)$  evaluates to  $N_{ax}$  and  $N(d_y)$  evaluates to  $N_{ay}$  at the entry. Similarly, say that  $N(d_x)$  evaluates to  $N_{bx}$  and  $N(d_y)$  evaluates to  $N_{by}$  at the exit. Then, a Bragg-Edge measurement can be written as:

$$\begin{aligned} \frac{1}{L} \hat{\mathbf{n}}^\top (\phi_q - \phi_p) &= \frac{1}{L} \begin{bmatrix} n_x & n_y \end{bmatrix} \left( \begin{bmatrix} u_q \\ v_q \end{bmatrix} - \begin{bmatrix} u_p \\ v_p \end{bmatrix} \right) \\ &= \frac{1}{L} \begin{bmatrix} n_x & n_y \end{bmatrix} \left( \begin{bmatrix} N_{ax}u_{a_1} + (1 - N_{ax})u_{a_2} \\ N_{ay}v_{a_1} + (1 - N_{ay})v_{a_2} \end{bmatrix} - \begin{bmatrix} N_{bx}u_{b_1} + (1 - N_{bx})u_{b_2} \\ N_{by}v_{b_1} + (1 - N_{by})v_{b_2} \end{bmatrix} \right) \\ &= \frac{1}{L} \begin{bmatrix} n_x & n_y \end{bmatrix} \left( \begin{bmatrix} N_{ax}u_{a_1} + (1 - N_{ax})u_{a_2} - N_{bx}u_{b_1} - (1 - N_{bx})u_{b_2} \\ N_{ay}v_{a_1} + (1 - N_{ay})v_{a_2} - N_{by}v_{b_1} - (1 - N_{by})v_{b_2} \end{bmatrix} \right) \\ &= \frac{1}{L} \left( n_x N_{ax}u_{a_1} + n_x(1 - N_{ax})u_{a_2} - n_x N_{bx}u_{b_1} - n_x(1 - N_{bx})u_{b_2} \right. \\ &\quad \left. + n_y N_{ay}v_{a_1} + n_y(1 - N_{ay})v_{a_2} - n_y N_{by}v_{b_1} - n_y(1 - N_{by})v_{b_2} \right). \end{aligned}$$

Which factors to

$$= \frac{1}{L} \begin{bmatrix} n_x N_{ax} & n_y N_{ay} & n_x(1 - N_{ax}) & n_y(1 - N_{ay}) & -n_x N_{bx} & -n_y N_{by} & -n_x(1 - N_{bx}) & -n_y(1 - N_{by}) \end{bmatrix} \begin{bmatrix} u_{a1} \\ v_{a1} \\ u_{a2} \\ v_{a2} \\ u_{b1} \\ v_{b1} \\ u_{b2} \\ v_{b2} \end{bmatrix}$$

Where again, the unknown quantities (here, the eight components of deformation corresponding to the four nodes affected by the intersection of a ray) have been written in terms of the known ray direction vector components, and (easily calculated) shape function evaluations.

### 2.2.3 Constructing a system of equations

With the general formulation derived in subsection 2.2.2, it is possible to — for any sample, under Assumption 2.1 and Assumption 2.2 — discretise the boundary into  $j$  nodes, and relate the magnitude of a Bragg-Edge measurement to the unknown deformations of the nodes intersected by a ray. Now, we apply this concept en masse. If  $k$  Bragg-Edge measurements are taken, and  $k$  equations of the above form are generated, then a system of equations with the following representation may be constructed:

$$\begin{bmatrix} y_1 \\ \vdots \\ y_k \end{bmatrix} = \begin{bmatrix} A_{11} & \cdots & A_{1j} \\ \vdots & \ddots & \vdots \\ A_{j1} & \cdots & A_{kj} \end{bmatrix} \begin{bmatrix} u_1 \\ v_1 \\ \vdots \\ u_j \\ v_j \end{bmatrix}. \quad (2.10)$$

Or, in shorthand:

$$\mathbf{y} = \mathbf{A}\Phi. \quad (2.11)$$

Where  $\mathbf{y}$  is a vector containing all of the Bragg-Edge strain measurements,  $\mathbf{A}$  is a co-efficient matrix with elements that contain unit direction vector components and shape function evaluations, and  $\Phi$  is a vector containing the unknown boundary node deformation components.

## 2.3 Discretised Problem Solution

With the problem formulated, the task is to now select a vector of nodal deformations  $\Phi$  that satisfies Equation 2.11. Unfortunately, the presence of measurement noise, and inaccuracies in our discretisation means that there will be no solution that perfectly satisfies the equation.

However, we can select a  $\Phi$  (say,  $\Phi^*$ ) that minimises the difference between  $\mathbf{A}\Phi^*$  and  $\mathbf{y}$ . Given that the co-efficient matrix  $\mathbf{A}$  is usually very sparse (with many measurements

taken, and only a maximum of eight columns per row with non-zero elements corresponding to four intersected nodes), it is natural to select an optimisation routine that exploits this property.

The LSQR algorithm, described in detail in [19], is well suited to this task. In general, LSQR computes a solution  $\mathbf{x}$  to problems of the following form:

$$\text{minimise} \quad \|\mathbf{Ax} - \mathbf{b}\|_2. \quad (2.12)$$

When the problem co-efficient matrix  $\mathbf{A}$  has more rows than columns (as is often the case with tomographic reconstruction, where more measurements are made than there are unknown boundary deformations), the solution vector  $\Phi$  which best fits the measurements in a linear least squares sense is obtained.

There are two necessary but not sufficient conditions that must be satisfied in order to obtain such a solution vector:

**Condition 2.1.** *When solving for  $\Phi$  in two dimensions, projections must be taken from at least three distinct directions. Here, distinct does not have any special meaning — as long as the three directions from which measurements are taken are not along the same line in space. Since there are three unique components in the 2D strain tensor, we require three directions of measurement in order to capture information about the  $\epsilon_{xx}$ ,  $\epsilon_{xy}$  and  $\epsilon_{yy}$  components. As symmetry of the tensor can be exploited, a fourth direction is not required.*

**Condition 2.2.** *The total number of measurements taken (the length of the  $\mathbf{y}$  vector) must be greater than or equal to the number of deformation components to be determined. That is to say, the  $\mathbf{A}$  matrix must be at least as tall as it is wide. Given that the number of measurements which can be made per projection is known, this allows pre-determination of the approximate number of projections that will be required. Care must be taken in such pre-determination, however, as in any projection, rays may travel from the source to the detector without passing through the sample. In this case, no information is contributed, and that measurement cannot help solve the problem.*

An interesting property of our problem is that even if we satisfy both of these conditions, the co-efficient matrix  $\mathbf{A}$  will always be rank deficient. Under [Assumption 2.2](#), it is only the *deformation* of the boundary that causes strains within our sample. In other words, our method is unable to distinguish between the correctness of the solutions shown in [Figure 2.5](#) (a) and (b), for example — either solution could produce a strain field that fits the measurements equally well. This is because any rigid-body motion of the sample (such as the  $\phi_r$  in [Figure 2.5](#)) does not change the shape of the deformed boundary, or (equivalently) impact the strain field in any way.

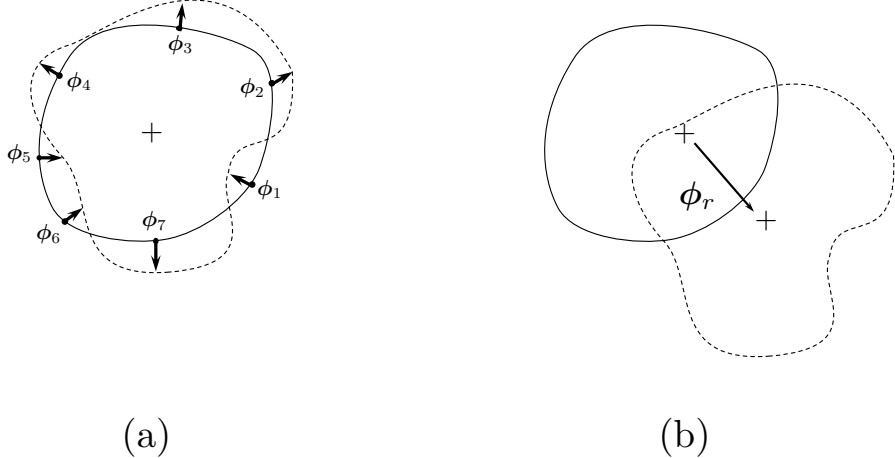


**Figure 2.5:** The solution states (a)  $\Phi = [\phi_1 \dots \phi_7]^\top$  and (b)  $\Phi + \phi_r$  fit the measurements equally well, since the reconstruction is invariant to rigid-body motions of the boundary.

Our discretised problem will always have a family of solutions, which consists of the ‘true’ boundary deformation, plus any rigid body motion of the boundary (that does not cause it to deform). Thankfully, the LSQR algorithm handles the singularity of the  $\mathbf{A}$  matrix that gives rise to this invariance, selecting from the family of possible solutions that which has minimum  $L_2$  norm — in other words, the  $\Phi$  that best fits the measurements with minimum  $\|\Phi\|_2$ . Of course, this solution is not necessarily the true boundary deformation, and post processing is required to remove rigid body motions if the deformed boundary is desired.

No post processing is necessary to obtain the correct strain field, however. The boundary deformations found by LSQR (even in the presence of rigid body motions) can be utilised as Dirichlet boundary conditions in a finite-element model of the system to obtain the strain tensor field within.

The singularity observed in our reconstruction is indicative of a much larger issue with general tomographic reconstruction, which will be addressed in [chapter 4](#).

This concludes our introduction to the boundary reconstruction method. In the following chapter, we will discuss a numerical implementation of this method and will analyse simulation results obtained.



# Chapter 3

## Simulation and Analysis: The Boundary Reconstruction Method

Bragg-Edge strain measurements are difficult to obtain, as a neutron spallation source capable of producing the pulsed wavelength-intensity spectra of neutrons is required. The sole neutron source in Australia, ANSTO, is not currently equipped to perform neutron transmission measurements suitable for strain tomography. Additionally, extension to full-field reconstruction represents a relatively new development in the research field, for which previous measurements have not been taken. The absence of suitable experimental data has prompted the development of a numerical environment that is capable of simulating Bragg-Edge measurements, and reconstructing the full 2D strain field by the boundary method described in [chapter 2](#).

In this chapter, we will discuss the nature and development of this environment, and analyse the results obtained in both the absence and presence of experimental nonidealities. The numerical environment has been developed using the commercial programming language MATLAB. For clarity, when referring to MATLAB code, `typewriter font` will be used, and standard syntax highlighting (e.g: `for`, `'string'`, `%comment`, etc.) implemented.

### 3.1 Measurement Simulation Environment

The numerical environment, developed in MATLAB, simulates Bragg-Edge measurements by applying the integral idealisation:

$$y = \frac{1}{L} \int_0^L \hat{\mathbf{n}}^\top \boldsymbol{\epsilon}(\mathbf{x}_0 + s\hat{\mathbf{n}}) \hat{\mathbf{n}} \, ds. \quad (1.8 \text{ revisited})$$

to a 2D strain field under study. Simulation of Bragg-Edge measurements is realised in three stages:

1. Numerically characterise the sample geometry and strain field under study.
2. Generate measurement geometry, and locate ray intersections.
3. Perform numerical integrals (of the form of [Equation 1.8](#)) of the strain field.

### 3.1.1 Sample and Strain Field Characterisation

To numerically characterise the strain field of the sample under study, the commercial finite-element modelling package STRAND7 has been used. A 2D plate model of the sample is first constructed in STRAND7, and the MATLAB-STRAND7 API has been used to import the model geometry (nodes, plates) and Gauss-point strain tensors. A number of wrapper functions have been refactored, debugged and developed to interact with the STRAND7 API to achieve this data import.

The discrete Gauss-point information is then used to construct `scatteredInterpolant` objects for each sample tensor strain field component (i.e:  $\epsilon_{xx}(x, y)$ ,  $\epsilon_{xy}(x, y)$ , etc.). These objects can be queried at any  $(x, y)$  position within the sample to obtain an interpolated strain, which is necessary for numerical integration. The '`natural`' (natural neighbour) interpolation method has been specified, which provides a smooth approximation to the strain field between Gauss-points, and is  $C^1$  continuous.

### 3.1.2 Measurement Geometry Generation and Ray Intersection Location

Further processing of the node and plate geometry is required before measurements can be simulated. The intrinsic `boundary` function is used to identify which node co-ordinates lie on the boundary of the sample. This implementation limits our analysis to samples with convex boundaries (a restriction imposed for simplicity, rather than physical limitations). Then, measurement geometry is generated as an array of detector pixel co-ordinates and ray propagation direction vectors. Finally, intersections between rays and boundary faces are detected. This is a time consuming process — where possible, parallel processing is used to reduce simulation time.

In a transmission experiment, the source and detector geometry is fixed, and the sample is rotated to take different projections. For ease of implementation in the simulation, the sample geometry location is kept constant, and the detector geometry is superimposed over the sample centre.

Neutron rays are simulated by extending lines from the detector pixels, and intersections with the sample boundary are detected with the intrinsic `polyxpoly` function. The detector pixels and associated ray propagation vectors are then rotated about the centre of the sample to change the direction of projection, as shown in [Figure 3.1](#).

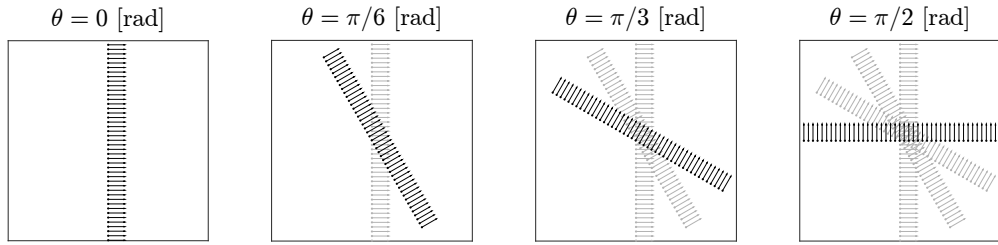


**Figure 3.1:** The detector pixels and associated ray propagation vectors are rotated as projections are taken from different directions.

### 3.1.3 Simulating Bragg-Edge Measurements

After detecting intersections between a ray and the sample boundary, a numerical integral which implements [Equation 1.8](#) is performed, with the co-ordinates of the ray entry and exit as bounds. The intrinsic MATLAB `trapz` routine is used, which performs numerical integrals using the trapezoidal rule. This method of integration is sensitive to the number of sample points used, and care has been taken to ensure systematic error is not introduced in simulated measurements by non-convergence of this routine.

Trapezoidal integration is performed for each successful ray (each ray that has intersected the sample twice — once at the entry, and once at the exit). A column vector  $\mathbf{y}$  is then constructed that contains all of the measured strains.

## 3.2 Reconstruction Algorithm

Once measurements have been simulated, a corresponding system of equations must next be constructed, utilising the relationships developed in [chapter 2](#). The intersect detection process identifies which boundary faces correspond to a given measurement. Thus, at this stage we are only required to perform two tasks:

1. Perform the shape function evaluations necessary to determine the relative weighting of deformation between the two nodes belonging to each face.
2. For each measurement, store entries in the  $\mathbf{A}$  matrix corresponding to the appropriate nodes, and consisting of shape function evaluations and ray propagation direction vector components as per [chapter 2](#).

Again, the considerable number of successful measurements and intermediate calculations that must be performed makes this a time consuming process.  $\mathbf{A}$  is stored to reduce memory overhead.

Finally, after constructing the  $\mathbf{A}$  matrix, the linear system of equations is solved using the intrinsic LSQR optimisation engine. Recall from [chapter 2](#) that  $\mathbf{A}$  is always rank deficient but has many more equations than unknowns.

In this case, LSQR returns the solution vector (a set of boundary deformations) that has minimum  $L_2$  norm and fits the measurements (within a specified tolerance) in a least-squares sense.

This solution vector is then passed back to STRAND7 via the API and utilised as a set of Dirichlet boundary conditions in a finite-element model of the sample. The result is a reconstructed strain field.

To quantify the quality of our reconstruction, we evaluate the error between the true (original) and reconstructed strain fields as follows. The unique strains at the  $j$  Gauss-points of the true field are concatenated and stored in a vector  $\boldsymbol{\varepsilon}_t$ , such that:

$$\boldsymbol{\varepsilon}_t = \begin{bmatrix} \epsilon_{xx_1} \\ \epsilon_{xy_1} \\ \epsilon_{yy_1} \\ \vdots \\ \epsilon_{xx_j} \\ \epsilon_{xy_j} \\ \epsilon_{yy_j} \end{bmatrix}. \quad (3.1)$$

Where  $\epsilon_{xx_1}$  is the  $\epsilon_{xx}$  strain at Gauss-point 1, and so on. A similar concatenation is performed for the reconstructed strains, which are stored in a vector  $\boldsymbol{\varepsilon}_r$ . Then, the *relative error* of the reconstruction is defined as:

$$E_{\text{rel}} = \frac{\|\boldsymbol{\varepsilon}_t - \boldsymbol{\varepsilon}_r\|_2}{\|\boldsymbol{\varepsilon}_t\|_2} \times 100\%. \quad (3.2)$$

### 3.3 Case Study: Cantilevered Beam Problem

To demonstrate a proof of concept and analyse the results produced by the boundary reconstruction method, a classic 2D problem has been examined — the well-known and well understood cantilevered beam. This system is an excellent test bed for our reconstruction — strains developed due to a load can display high gradients in some areas, analytical solutions to the strain field exist, and (most importantly), we can ensure that [Assumption 2.2](#) is satisfied (the foundations of this decision will be explained and justified in [chapter 4](#)). A free-body diagram of the system studied is shown in [Figure 3.2](#).

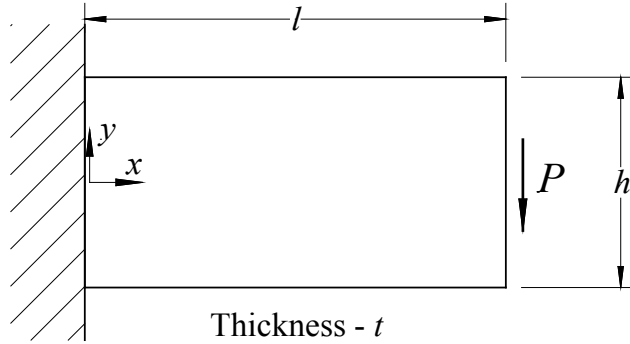


**Figure 3.2:** System free-body diagram.

For analysis, beam geometry was selected to ensure that strains in the order of  $1 \times 10^{-3}$  (giving rise to stresses in the order of 200 MPa) were developed in the sample. Material properties are representative of common steel. Parameters implemented are detailed in [Table 3.1](#).

Parameter	Symbol	Value
Edge Load	$P$	2 kN
Beam Length	$l$	20 mm
Beam Height	$h$	10 mm
Beam Thickness	$t$	6 mm
Young's Modulus	$E$	200 GPa
Poisson's Ratio	$\nu$	0.3

**Table 3.1:** Cantilevered beam system parameters

A finite-element model of the system was constructed, with the mesh consisting of nominally square, 0.5 mm wide quad4 plate elements. This discretisation was chosen to ensure a manageable number of boundary nodes were imported for reconstruction. The resultant strain fields (as solved by FEA) are shown in [Figure 3.3](#). The solution was obtained from a linear-static solve. Note that deviation from the theoretical solution to this problem is observed toward the left-hand side of the beam, due to the physical restraints imposed on the nodes at the left-hand boundary — the finite element model more accurately models a ‘real’ (physical) field.

The components of the biaxial strain tensor at the Gauss-points of each element were imported into MATLAB via the STRAND7 API. Simulated measurements were made with a detector pixel spacing of 55  $\mu\text{m}$  (representative of current generation technology at J-PARC [\[18\]](#)), and width of 30 mm. 200 sample points were used in the `trapz` integration algorithm, which was observed to be within the convergence band of this routine.

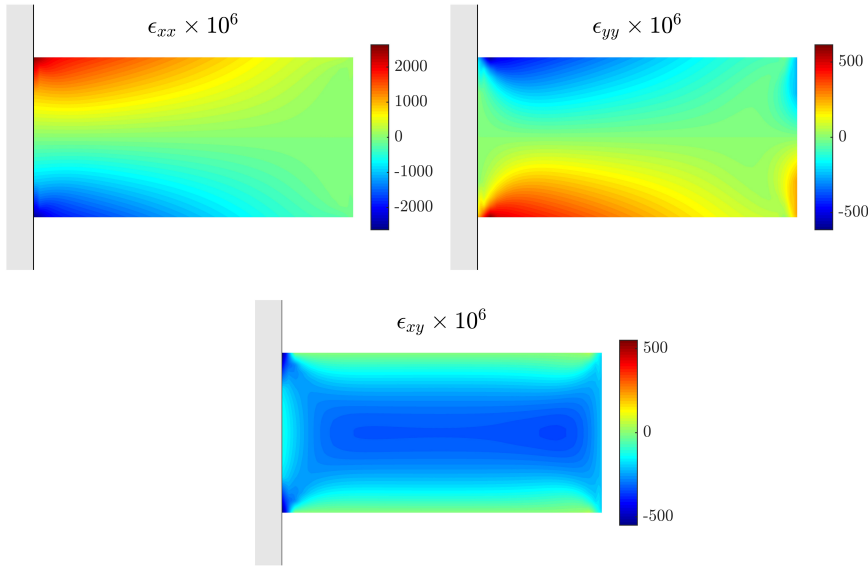


**Figure 3.3:** Finite element solutions to the strain field.

After constructing the system of simultaneous equations associated with our simulated measurements, the intrinsic `svd` function was used to confirm that the co-efficient matrix  $\mathbf{A}$  was indeed rank deficient, with three ‘degrees of freedom’ present (corresponding to the  $x$  and  $y$  rigid-body translation, and in-plane rotation that a boundary can be subject to without changing the strain field within). This singularity was visible in the solution, which displayed rigid body motion in addition to boundary deformation.

A simple optimisation routine (utilising the `fmincon` intrinsic engine) was developed to rotate and translate the resolved deformation field until the left hand edge aligned with its original position (since this edge was restrained and known not to deform). Once rotated and translated, these reconstructed deformations were exported to STRAND7 to obtain a reconstructed strain field.

### 3.3.1 Simulation Results: Ideal Measurements

To identify systematic error present within the measurement environment and reconstruction algorithm, tomographic strain reconstruction was first attempted in the absence of any experimental nonideality. That is, under the following assumptions:

**Assumption 2.3 (revisited).** *Neutron rays are infinitesimally thin.*

**Assumption 2.4 (revisited).** *Neutron rays are not attenuated as they pass through a sample.*

and

**Assumption 3.3.** *That measurements are taken in the absence of experimental noise.*

The validity of these assumptions will be discussed in the following sections. In order to evaluate the convergence of the algorithm under these conditions, simulations were conducted where only the number of projections (and thus measurements) was varied.

Rapid convergence of the reconstruction to the true strain field was observed as the number of projections was increased from the minimum (5, to satisfy [Condition 2.1](#) and [Condition 2.2](#)). The original and reconstructed principal strain fields are shown in [Figure 3.4](#).

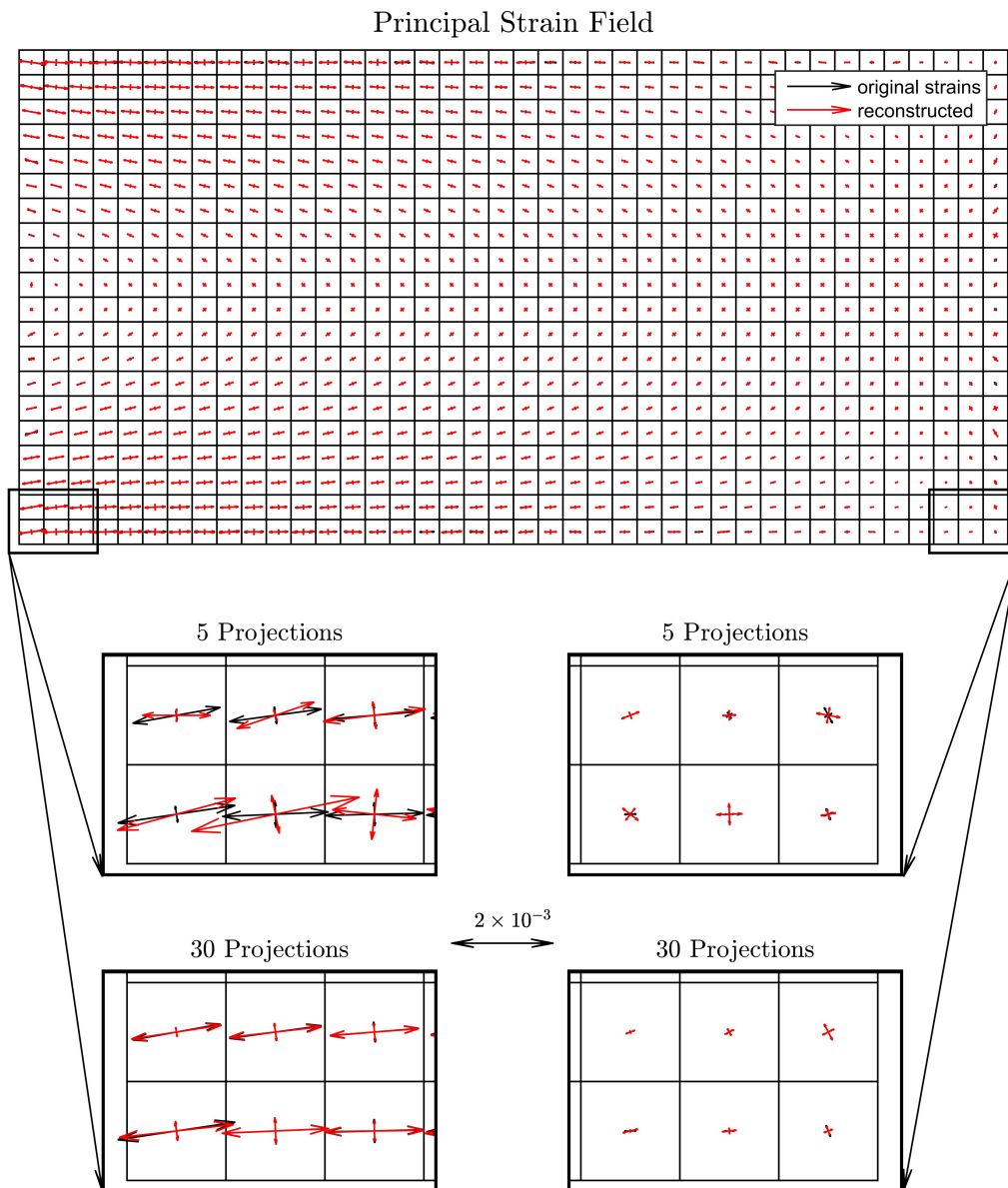


**Figure 3.4:** Reconstructed principal strain distributions within the cantilevered beam. Original strain fields are black, reconstructed strain fields are red.

It was observed that by 30 projections, enough information had been gathered to arrive at a solution within 5 % magnitude of the final simulated value, indicating convergence. However, even when the number of projections taken was increased well past the convergence state (to 200 — a number that would be impractical to achieve experimentally), a floor of approximately 2% relative error (as calculated in [Equation 3.2](#)) was present.

While problem discretisation and numerical error can certainly contribute to an imperfect reconstruction, it was found that this error floor was largely caused by systematic error in the measurement environment. STRAND7 interpolates strain within plate elements using finite-element shape functions. This discrete data is then transferred to MATLAB for analysis. This interpolation method differs from the natural-neighbour interpolation utilised in the construction of the `scatteredInterpolant` objects which are probed in our measurement simulation.

Minor differences between the two have resulted in simulated measurement of a field that differs slightly from what the boundary deformation would imply.

With the problem being so minor, and found to lie in the measurement environment rather than the reconstruction algorithm (meaning that such a problem would not develop with real-world data) it was determined that eliminating this error was not a time-effective endeavour.

In summary, it was found that the reconstruction algorithm was extremely effective at achieving strain field reconstruction in ideal conditions.

### 3.3.2 Simulation Results: Measurement Uncertainty

Real Bragg-Edge measurements are plagued with uncertainty. To evaluate the ability of the reconstruction algorithm to cope with this experimental nonideality, [Assumption 3.3](#) was relaxed.

For Bragg-Edge neutron transmission measurements, a strain uncertainty characterised by a standard deviation in the order of  $1 \times 10^{-4}$  is a conservative estimate, with instruments able to resolve strains in some materials of the order of  $1 \times 10^{-5}$  [6].

In evaluating the robustness of our algorithm, normally distributed (Gaussian) noise with a mean value zero and standard deviation  $\sigma$  was introduced to the simulated Bragg-Edge measurements  $\mathbf{y}$  as follows:

$$\mathbf{y}' = \mathbf{y} + \mathcal{N}(0, \sigma) \quad (3.3)$$

The reconstruction algorithm was not modified to compensate for the noisy measurements. Simulations were run to analyse the convergence of the reconstruction with increasing projections for  $\sigma = \{0.25 \times 10^{-4}, 0.5 \times 10^{-4}, 0.75 \times 10^{-4}, 1 \times 10^{-4}, 1.25 \times 10^{-4}\}$ .

Results are shown in [Figure 3.5](#). Since the solution error was largely normal, and to more closely compare the quality of the reconstruction as a function of the ‘amount’ of noise in the measurements, solution error here has been reported as a standard deviation, and calculated as:

$$E_{\text{std}} = \text{std}(\boldsymbol{\varepsilon}_t - \boldsymbol{\varepsilon}_r). \quad (3.4)$$

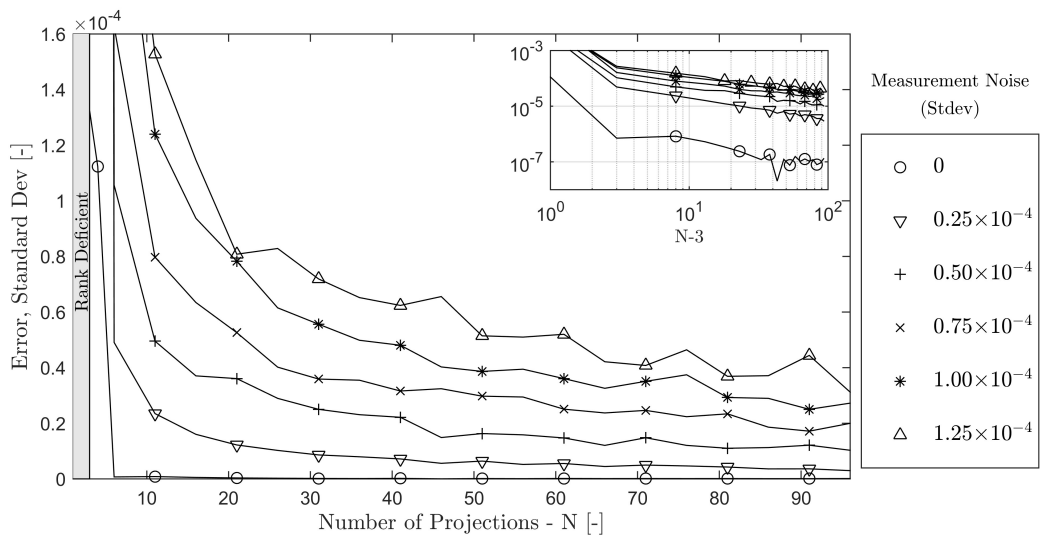


**Figure 3.5:** Uncertainty in reconstructed strains as a function of the number of projections taken and magnitude of measurement noise applied.

Irrespective of the amount of noise applied, the reconstruction algorithm was able to converge to a solution when enough projections were taken. As expected, increasing the magnitude of measurement noise (by increasing the standard deviation  $\sigma$ ) resulted in slower convergence to a more erroneous solution.

It was observed that in all cases, once 30 projections had been taken, the standard deviation of the reconstruction error was less than that in the measurements. These results demonstrate that the reconstruction algorithm is able to reject simulated normally distributed measurement noise. This provides confidence in the ability of the algorithm to converge to a correct reconstruction in the presence of real experimental uncertainty.

### 3.3.3 Simulation Results: Ray Attenuation

In addition to experimental uncertainty, real neutron rays are subject to attenuation as they travel through a sample. The magnitude of this attenuation depends on the

material properties of the irradiated body. The result is that strains closer to the entry point of the ray path have more impact on the measurement than those closer to the exit. As was done for experimental uncertainty, [Assumption 2.4](#) was relaxed to evaluate the ability of the reconstruction algorithm to converge in the presence of attenuated measurements.

With respect to the co-ordinate system shown in [Figure 1.9](#), attenuation can be modelled by an exponential decay function [18] of the form:

$$\chi(s) = e^{-\mu s} \quad (3.5)$$

With attenuation present, a Bragg-Edge measurement can be approximated by:

$$y = \frac{1}{\int_0^L \chi(s) ds} \int_0^L \chi(s) \hat{\mathbf{n}}^\top \boldsymbol{\epsilon}(\mathbf{x}_0 + s\hat{\mathbf{n}}) \hat{\mathbf{n}} ds. \quad (3.6)$$

The measurement environment was modified to apply [Equation 3.6](#) in the numerical integration stage. Simulations were run to observe the converge of the reconstruction with increasing projections for  $\mu = \{5 \text{ m}^{-1}, 15 \text{ m}^{-1}, 30 \text{ m}^{-1}, 60 \text{ m}^{-1}, 90 \text{ m}^{-1}, 120 \text{ m}^{-1}, 500 \text{ m}^{-1}\}$ . For context: for neutrons with energy in the order of 25meV, Iron has a characteristic attenuation coefficient of  $11.9 \text{ m}^{-1}$ , Aluminium has  $10 \text{ m}^{-1}$ , and Mercury has  $162 \text{ m}^{-1}$  [20].

A baseline level of noise (standard deviation  $\sigma = 1 \times 10^{-4}$ ) was applied to the measurements. Results are shown in [Figure 3.6](#).

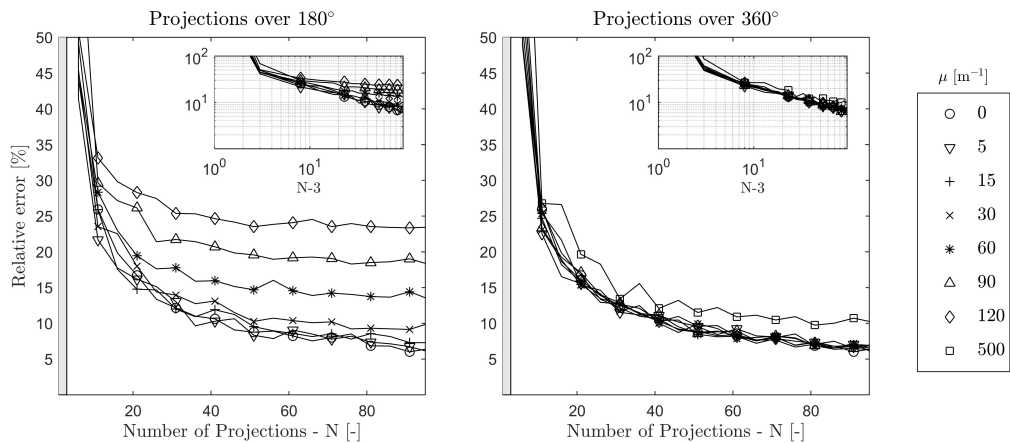


**Figure 3.6:** Relative error in reconstructed strains as a function of the number of projections taken and magnitude of attenuation applied.

Since non attenuated Bragg-Edge measurements have the same magnitude when taken in the forward or backward directions, it was not previously necessary to take measurements over more than  $180^\circ$ . Here, interestingly, significantly more error in the reconstruction

was observed when projections were taken over  $180^\circ$  rather than the full  $360^\circ$  of the sample. This error is primarily caused by non-complete sampling of the strain field — when projections are only taken over  $180^\circ$ , the same area of the sample (furthest from the incident radiation) is always contributing less information to the measurement than that closest to the ray entry.

It was observed that this problem was largely rectified by taking projections over the entire  $360^\circ$  of the sample. Accordingly, directions of measurement were alternated to ensure the sample was uniformly measured. Specifically, for a set of  $N$  projections; angles over  $180^\circ$  were chosen as  $\frac{\pi}{N}n$ , while corresponding angles over  $360^\circ$  were  $\frac{\pi}{N}n + \frac{\pi}{2}(1 - (-1)^n)$ , where  $n = \{0, 1, \dots, N-1\}$ . Measurement directions are shown in Figure 3.7.

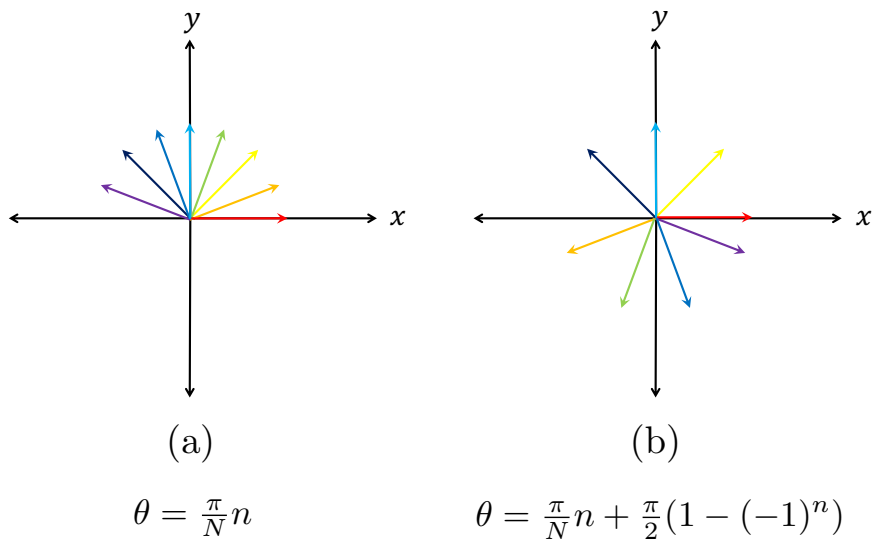


**Figure 3.7:** Projection directions for (a) projections over  $180^\circ$  and (b) over  $360^\circ$ .

For  $\mu = 120\text{m}^{-1}$  (characteristic of common steel at the energies typically associated with Bragg-Edge measurement), with measurements taken over  $360^\circ$ , convergence to a solution state with less than 10% relative error was observed with only 60 projections taken. Additionally, this reconstruction was within 1% relative error of the results obtained for non-attenuated (but equally noisy) measurements.

It was observed that absurdly high levels of attenuation (in the order of  $500\text{ m}^{-1}$ , an order of magnitude higher than that for materials typically studied) were required to reduce the effectiveness of the algorithm to converge to a satisfactory solution. Even for this level of attenuation, convergence to a solution with approximately 11% relative error was observed. Note that over the length of the sample studied here, this level of attenuation results in a transmission rate of less than 1%.

In summary, simulation results suggest that the reconstruction algorithm is able to converge to an adequate reconstruction in the presence of expected and severe attenuation, provided that measurements are taken over the entire  $360^\circ$  of a sample.

### 3.3.4 Simulation Results: Ray Width

In reality, neutron rays are not infinitesimally thin. While collimators can limit effective ray size, there is a finite width over which atomic planes within the sample can contribute to diffraction due to the dispersion of neutrons as they travel toward and through the sample. The finite width of detector pixels also limits the maximum resolution available.

Instrument scientists at neutron sources are able to control the effective ray width, ‘smoothing’ measurements by treating detections over several adjacent pixels as a single entity. This is often necessary, as the minute size of the pixels often means that significant time must elapse to detect enough neutrons on each pixel to form an accurate measurement.

In the absence of attenuation, and with respect to the co-ordinate system shown in [Figure 3.9](#), a Bragg-Edge measurement of width  $W$  can be approximated by the surface integral:

$$\begin{aligned} y &= \frac{1}{W} \int_0^W \frac{1}{L} \int_0^L \hat{\mathbf{n}}^\top \boldsymbol{\epsilon}(\mathbf{x}_0 + s\hat{\mathbf{n}} + t\hat{\mathbf{n}}^\perp) \hat{\mathbf{n}} \, ds \, dt \\ &= \frac{1}{LW} \int_0^W \int_0^L \hat{\mathbf{n}}^\top \boldsymbol{\epsilon}(\mathbf{x}_0 + s\hat{\mathbf{n}} + t\hat{\mathbf{n}}^\perp) \hat{\mathbf{n}} \, ds \, dt \end{aligned} \quad (3.7)$$

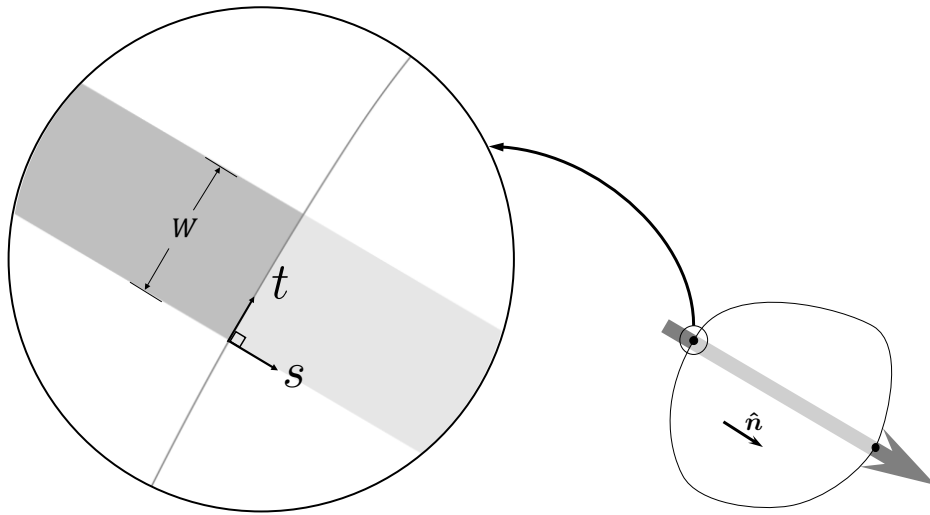


**Figure 3.8:** The  $s - t$  co-ordinate system used for Ray-Width analysis.

To evaluate the ability of the (unmodified) reconstruction algorithm to converge in the presence of measurements of finite ray width, [Assumption 2.3](#) was relaxed, and the measurement environment was modified to apply [Equation 3.7](#) in the numerical integration stage.

The surface integral is performed using nested `trapz` functions. As such, it becomes necessary to define a resolution in both the  $s$  and  $t$  directions. As was the case previously, a mesh independence study was undertaken to ensure that the  $t$  resolution was sufficient to achieve independence.

To perform the surface integral with the potentially troublesome boundary geometry, the measurement process requires slight modification:

1. A grid of integration sample points is created with the previously defined  $s$  and  $t$  resolutions. The grid width is the ray width, and length is selected to be greater than that of the sample to ensure complete coverage.
2. The grid origin is aligned to the outside of the ray entry point, offset sufficiently far to ensure complete coverage, as shown in [Figure 3.9](#).
3. Nested `trapz` functions are used to evaluate [Equation 3.7](#) over the span of the grid.

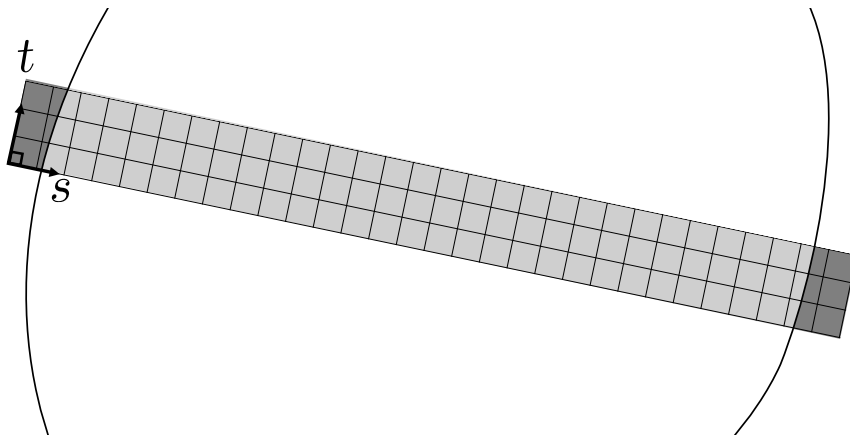


**Figure 3.9:** A grid aligned with the local  $s - t$  co-ordinate system is created to perform a surface integral.

The conservative placement of the grid allows for integration points to lie outside the sample. The `inpolygon` intrinsic function is used to determine whether a point is outside the sample boundary, and conditional programming is used to assign zero magnitude strain values at these points.

Simulations were run to observe the convergence of the reconstruction with increasing projections for a ray with  $W = \{26\mu\text{m}, 52\mu\text{m}, 104\mu\text{m}, 156\mu\text{m}, 208\mu\text{m}\}$ , corresponding to 0.5, 1, 2, 3 and 4 pixel widths respectively. Again, a baseline level of noise (standard deviation  $\sigma = 1 \times 10^{-4}$ ) was applied to the measurements. Results are shown in [Figure 3.10](#).

It was found that the unmodified reconstruction algorithm was able to reject nonideality introduced by the simulated finite width of the neutron rays extremely well. Convergence

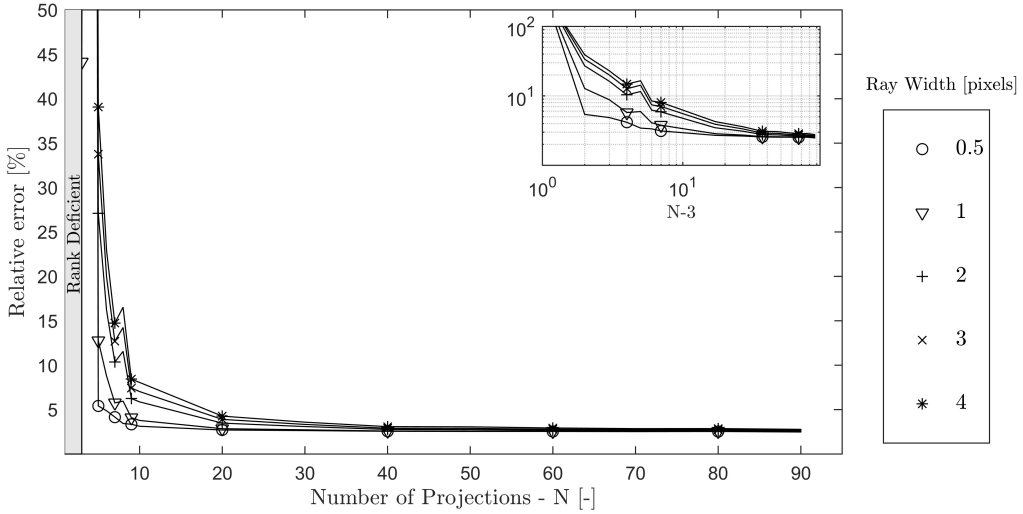


**Figure 3.10:** A negligible increase in relative error was observed as the measurement ray width was increased.

to a solution with less than 5% relative error in all cases was observed with only 40 projections taken. Additional error of less than 1% was observed for the largest ray when compared to the non-attenuated (but equally noisy) case.

In summary, it was found that the ability of the reconstruction algorithm to converge to an adequate solution was largely insensitive to ray-width effects at up to four pixel widths.

### 3.4 Conclusions

The boundary reconstruction method has shown promise in the tomographic reconstruction of elastic strain fields for samples subject to in-situ loadings only. Tomographic reconstruction has been achieved for simulated Bragg-Edge measurements in the absence and presence of experimental uncertainty, measurement attenuation, and neutron ray width.

In all cases, the reconstruction algorithm was able to reliably converge to a solution with very little error. This encouraging result suggests that when experimental data becomes available, the algorithm will be of value in achieving strain tomography. Additionally, the developed simulation environment should be of use in the planning and execution of Bragg-Edge experiments, as a more accurate pre-determination of the number of projections required can be made.

However, [Assumption 2.2](#) is extremely limiting in the types of strain fields that can be studied using this method. In the following chapters, we will discuss the nature of this limitation, the more general reconstruction problem, and another potential approach.

The work undertaken and described in this chapter formed the foundation of a journal article co-authored by the author of this thesis, which has since been submitted and accepted [17]. This article has been included in [Appendix B](#).



## Chapter 4

# General Tomographic Reconstruction

At this stage, we have simulated Bragg-Edge strain tomography under a set of limiting assumptions, the most restrictive of which was:

**Assumption 2.2 (revisited).** *We will assume that the samples under examination are subject only to in-situ loadings — that is, boundary tractions. Specifically, this means that any strain field under examination must be free of plastic strains, thermal strains, or body forces.*

Clearly, this assumption severely restricts the types of strain field we may wish to examine. For example, the presence of plastic or other locked-in strains — even in carefully prepared samples — is an unfortunate reality in many cases. In this chapter, we will extend our understanding to general tomographic reconstruction. We will discuss why Assumption 2.2 was required to formulate the boundary reconstruction method, and the implications of relaxing this assumption. We will also briefly discuss the work previously undertaken in this field of research.

### 4.1 Prerequisite: Eigen Strains and Compatibility

Assumption 2.2 specifically precludes the presence of strains that are plastic, thermal, or due to body forces in a sample under study. In general, any ‘total’ strain field within a sample  $\epsilon(x, y)$  can be decomposed into the superposition of a field of elastic strains  $\epsilon_E(x, y)$ , a field of thermal strains  $\epsilon_T(x, y)$  and a field of other inelastic strains (referred to as *Eigen* strains), arising from plasticity or interference  $\epsilon_P(x, y)$ , such that:

$$\epsilon(x, y) = \epsilon_E(x, y) + \epsilon_T(x, y) + \epsilon_P(x, y). \quad (4.1)$$

Now, recall from chapter 2 that our ability to relate the boundary deformation of a sample to a Bragg-Edge measurement relied on writing the total strain  $\epsilon(x, y)$  in terms of the deformation gradient tensor  $H$  by:

$$\boldsymbol{\epsilon}(x, y) = \frac{1}{2}(\mathbf{H} + \mathbf{H}^\top). \quad (\text{2.2 revisited})$$

A total strain field can be written this way as a consequence of the field being *compatible*. Compatibility is a condition that ensures that the infinitesimal volume elements that comprise a body remain connected in such a way that gaps or overlaps between elements do not develop. In a 2D, plane-stress situation, the compatibility constraint takes the form:

$$2\frac{\partial^2 \epsilon_{xy}}{\partial x \partial x} - \frac{\partial^2 \epsilon_{xx}}{\partial y^2} - \frac{\partial^2 \epsilon_{yy}}{\partial x^2} = 0 \quad (4.2)$$

Within continuum mechanics, all physical total strain fields (in samples that do not experience cracking or tearing)  $\boldsymbol{\epsilon}(x, y)$  are compatible. When working under [Assumption 2.2](#), we have exclusively considered the case where there are no Eigen strains or thermal strains present, which has allowed us to write:

$$\begin{aligned} \underbrace{\boldsymbol{\epsilon}(x, y)}_{\text{compatible}} &= \underbrace{\boldsymbol{\epsilon}_E(x, y) + \boldsymbol{\epsilon}_T(x, y) + \boldsymbol{\epsilon}_P(x, y)}_{\text{compatible}} \\ &= \underbrace{\boldsymbol{\epsilon}_E(x, y) + \boldsymbol{\epsilon}_T(x, y) + \boldsymbol{\epsilon}_P(x, y)}_{\text{compatible}}^0 \\ \implies \underbrace{\boldsymbol{\epsilon}(x, y)}_{\text{compatible}} &= \underbrace{\boldsymbol{\epsilon}_E(x, y)}_{\text{compatible}}. \end{aligned}$$

Substituting [Equation 2.2](#):

$$\implies \boldsymbol{\epsilon}_E(x, y) = \frac{1}{2}(\mathbf{H} + \mathbf{H}^\top). \quad (4.3)$$

Since our Bragg-Edge measurements only detect strains which cause diffraction by the stretching apart of lattice planes, they only measure the  $\boldsymbol{\epsilon}_E(x, y)$  component of strain.

When we assume that  $\boldsymbol{\epsilon}_P(x, y) = \boldsymbol{\epsilon}_T(x, y) = 0$ , we ensure [Equation 4.3](#) holds, allowing us to relate our Bragg-Edge measurements to the deformation of the boundary.

If we are to relax [Assumption 2.2](#), we no longer guarantee the ability to write [Equation 4.3](#) and can only say:

$$\underbrace{\epsilon(x, y)}_{\text{compatible}} = \underbrace{\overbrace{\epsilon_E(x, y)}^{\text{compatible}} + \overbrace{\epsilon_P(x, y)}^{\text{compatible}} + \overbrace{\epsilon_T(x, y)}^{\text{compatible}}}_{\text{compatible}} \quad (4.4)$$

or

$$\underbrace{\epsilon(x, y)}_{\text{compatible}} = \underbrace{\overbrace{\epsilon_E(x, y)}^{\text{incompatible}} + \overbrace{\epsilon_P(x, y)}^{\text{incompatible}} + \overbrace{\epsilon_T(x, y)}^{\text{incompatible}}}_{\text{compatible}} \quad (4.5)$$

Where in [Equation 4.4](#), the elastic and inelastic strain field components are each compatible, and in [Equation 4.5](#) both the elastic and inelastic components are incompatible (but in such a way that the total strain is compatible).

In the case of [Equation 4.4](#), where the elastic component is compatible, the boundary reconstruction method can in fact be formulated and used to achieve reconstruction of the elastic component.

In the case of [Equation 4.5](#), the elastic component (seen by our Bragg-Edge measurements) is incompatible and cannot by itself be written as a gradient of a displacement field, meaning the boundary reconstruction method cannot be applied.

Nevertheless, it is difficult to identify whether developed plastic strains are compatible or incompatible, and an approach that is not sensitive to this condition is desirable.

Is it then possible to achieve tomography in the general sense? How can such a problem be approached? To answer these questions, let us first recount the work undertaken by others in this area.

## 4.2 Literature Review: Previous Work

In recent years, there has been significant headway made in this research area. While development of Bragg-Edge time-of-flight imaging has been ongoing over the past decade, the work most relevant to our goal of achieving general tomographic reconstruction is that pioneered by Associate Professor Brian Abbey and Mr Henry Kirkwood at La Trobe University. In this section, we will discuss their findings. We will also discuss the findings of Professors William Lionheart and Philip Withers at The University of Manchester, who have examined mathematically the problem of general tomographic strain reconstruction (in the absence of attenuation).

### 4.2.1 Feasibility study of neutron strain tomography

In 2009, the feasibility of conducting strain tomography via neutron transmission was demonstrated [21]. Under the assumptions of compatibility and axisymmetry, reconstruction of the plane-strain, 2D tensor residual strain field within a quenched, cylindrical, stainless steel bar was achieved. The assumption of compatibility reduced the two dimensional unknown field to a scalar reconstruction problem. Only the hoop strain required reconstruction, as compatibility provided an explicit relationship between that and the radial strain.

Axisymmetry of the problem meant that projections from only a single direction were required to characterise the strain field. The strain — now only a function of radius — was modelled by a linear combination of exponential basis functions, such that:

$$\epsilon_{\theta\theta}(r) = c_n + \sum_{i=0}^{n-1} c_i e^r r^i \quad (4.6)$$

This model was chosen based on strain field predictions obtained from finite-element analysis. In a similar vein to our construction of a system of equations to determine unknown boundary deformations, the authors here used the Bragg-Edge measurements to determine the unknown co-efficients of this model. Co-efficients were selected using a least-squares optimisation routine.

Reconstruction results showed close agreement with validation experiments performed via diffraction, and finite-element model predictions. The authors concluded that tomography via neutron transmission (at least in axisymmetric cases) was feasible.

### 4.2.2 Reconstruction of axisymmetric strain distributions via neutron strain tomography

In 2012, alternate approaches to the axisymmetric reconstruction problem were published [22]. Again, the authors identified and exploited that the two-dimensional problem could be reduced to a scalar reconstruction problem by assuming strain field compatibility. In this case, an axisymmetric ‘ring and plug’ system (where a plug is pressed into a ring of smaller inner diameter) was examined.

Novelly, the authors achieved tomography with a (finite element) model-free approach, that fit 1D, piecewise-linear radial ‘tent’ functions to the Bragg-Edge measurements. Basis functions that included these ‘tent’ functions were selected to enforce compatibility, and a least-squares optimisation engine with Tikhonov regularisation was used to determine the unknown parameters. Practically, this new method largely resembled the

previous approach, with the exception that the basis functions used were not based on finite-element predictions.

As before, reconstruction centering around the previously developed exponential model was also attempted. The method remained largely unchanged from the previous work.

Results were encouraging, with close agreement noted between reconstructed strain fields, diffraction measurements, and well known analytical solutions to the strain field.

In this work, the authors also showcased a new method in which compatibility was not assumed. Here, diffraction measurements were utilised to resolve one of the unknown strain component fields, leaving only one unknown to reconstruct via transmission. This method was applied to the previously reconstructed stainless-steel cylinder. Results showed that even the inclusion of only two diffraction measurements aided immensely in the quality of the reconstruction obtained.

#### **4.2.3 Bragg Edge Neutron Strain Tomography**

In 2013, a conference paper published by Abbey and Kirkwood demonstrated that further improvement in the reconstruction could be seen by implementing a maximum-entropy method of co-efficient regression, and higher order (B-spline) basis functions [23]. Maximum entropy optimisation essentially selects the simplest possible solution (here, basis function parameters) that will fit the measurements.

B-spline basis functions were compared with triangular (tent) functions to achieve reconstruction on the ring and plug system previously examined. It was found that a trade-off existed between the smooth behaviour of strain distributions and the stability of the reconstruction in the presence of noise. The authors concluded that while B-splines could result in a reconstruction that was closer to the expected results, the numerical stability of the triangular basis functions meant that they provided the most reliable approach to tomography.

Again, compatibility and axisymmetry were assumed.

#### **4.2.4 Neutron Strain Tomography using the Radon Transform**

Published as a conference proceeding in 2015 [24], this work describes and demonstrates another approach to the tomographic reconstruction problem. Here, no prior knowledge or model of the strain field is required in the reconstruction. Axisymmetry was assumed, and a scalar field composed of components of the underlying strain defined as:

$$\mathbf{E}_T(r, \theta) = \epsilon_{rr}(r) \sin^2(\theta) + \epsilon_{\theta\theta}(r) \cos^2(\theta) \quad (4.7)$$

The benefit of this formulation was that certain measurements through this field could be represented by the Radon transform, meaning that algorithms suited to solving regular CT problems could be utilised to reconstruct this scalar field. Finally, examination of this reconstructed scalar field at  $\theta = 0$  and  $\theta = \pi/2$  resolves the  $\epsilon_{\theta\theta}$  and  $\epsilon_{rr}$  components respectively.

Reconstruction of the familiar ring-and-plug system was again achieved, with simulated measurements. Reconstruction of the residual strain within a fillet-rolled Nickel bolt was also achieved with experimental measurements. In both cases, reconstruction closely matched theoretical predictions or validation measurements.

While this result was significant in that compatibility was not explicitly assumed in the formulation, problem axisymmetry was still required to achieve reconstruction. This method was formulated using linear elasticity theory, and it was noted that extension to non-axisymmetric reconstruction would require a more sophisticated deformation model.

#### 4.2.5 *Diffraction tomography of strain*

In contrast to previous approaches which have relied on axisymmetry and compatibility, in 2015, [25] Professors William Lionheart and Philip Withers at The University of Manchester examined the general reconstruction problem from a mathematicians perspective.

They demonstrated that the general tomographic strain reconstruction (at least under assumed idealities, including the absence of attenuation) is not possible. It was shown that the magnitude of a Bragg-Edge measurement (as modelled by [Equation 1.8](#)) is only sensitive to changes in the path length of a neutron ray through a body, and not (directly) to the strain field within. This discovery agrees with our [chapter 2](#) formulation that related the measurement magnitude to the relative boundary deformation.

Consider, as an example a class of problems where the sample boundary is restrained, and a load is applied to the interior, developing a strain field. The key result from Lionheart and Withers is that an idealised Bragg-Edge projection (of the form of [Equation 1.8](#) through one of these fields will produce a measurement of zero magnitude (as a result of the fixed boundary), irrespective of the strain field within.

Of course, this means that a projection of measurements within this class (containing only zero magnitude measurements) has no unique corresponding strain field — any number of fixed-boundary fields could have produced these measurements. This non-uniqueness lies at the heart of what makes the general tomographic problem extremely difficult, and is worth discussing on its own.

### 4.3 Existence and Uniqueness, Problem Null Space

Recall from [chapter 1](#) that a Bragg-Edge measurement can be modelled by the integral:

$$y = \frac{1}{L} \int_0^L \hat{\mathbf{n}}^\top \boldsymbol{\epsilon}(\mathbf{x}_0 + s\hat{\mathbf{n}}) \hat{\mathbf{n}} \, ds. \quad (1.8 \text{ revisited})$$

Alternatively, written as:

$$y = T(\boldsymbol{\epsilon}, \mathbf{x}_0, \hat{\mathbf{n}}) = \frac{1}{L} \int_0^L \hat{\mathbf{n}}^\top \boldsymbol{\epsilon}(\mathbf{x}_0 + s\hat{\mathbf{n}}) \hat{\mathbf{n}} \, ds \quad (4.8)$$

Where  $T(\boldsymbol{\epsilon}, \mathbf{x}_0, \hat{\mathbf{n}})$  is a linear transformation. The *null space* (or *kernel*) of a linear transformation is the subset of inputs (here strain fields  $\boldsymbol{\epsilon}(x, y)$ ) that are mapped to zero. When a linear transformation is *injective* (or *one-to-one*), there is only one input that corresponds to each output. In this case, it can be shown that such a transformation has a trivial kernel (only containing the zero vector).

The key result identified by Lionheart and Withers is that the transformation in [Equation 4.8](#) is certainly not injective — any number of fixed-boundary strain fields map to zero. This non-trivial null space means that without further constraints, there are an infinite number of strain fields  $\boldsymbol{\epsilon}$  that will fit a set of measurements.

For example, consider the existence of a fixed-boundary elastic strain field  $\boldsymbol{\epsilon}_n$  (for **null**). Under the transformation modelling our neutron transmission measurements, and the [Assumption 2.2](#), this strain field would produce zero-magnitude measurements for any ray inlet position  $\mathbf{x}_0$  or propagation direction  $\hat{\mathbf{n}}$ :

$$T(\boldsymbol{\epsilon}_n, \mathbf{x}_0, \hat{\mathbf{n}}) = 0 \quad (4.9)$$

This is in contrast to a measurement through a non-zero strain field that is not in the kernel of the transform:

$$T(\boldsymbol{\epsilon}, \mathbf{x}_0, \hat{\mathbf{n}}) = y. \quad (4.10)$$

The superposition of these measurements is:

$$T(\boldsymbol{\epsilon}_n, \mathbf{x}_0, \hat{\mathbf{n}}) + T(\boldsymbol{\epsilon}, \mathbf{x}_0, \hat{\mathbf{n}}) = 0 + y. \quad (4.11)$$

Since  $T$  is a linear transformation:

$$T(\epsilon_n + \epsilon, \mathbf{x}_0, \hat{\mathbf{n}}) = y = T(\epsilon, \mathbf{x}_0, \hat{\mathbf{n}}). \quad (4.12)$$

In other words, if a strain field  $\epsilon$  produces a measurement  $y$ , then any of the fields  $\epsilon + \epsilon_n$  will also produce the same measurement. This means that given a measurement and the model of the transformation, there are an infinite number of fields of the form  $\epsilon + \epsilon_n$  that could have produced it.

This non-uniqueness has an analogue in the magic-square example described in [chapter 1](#). If a magic square (such as that shown in [Figure 4.1a](#)) is analogous to a ‘true’ strain field  $\epsilon$ , then a null strain field  $\epsilon_n$  is analogous to a magic square which sums to zero ([Figure 4.1b](#)). The superposition of these fields ([Figure 4.1c](#)) is then one that gives the same ‘measurements’ (row, column and diagonal sums) as the first field, despite containing other elements.

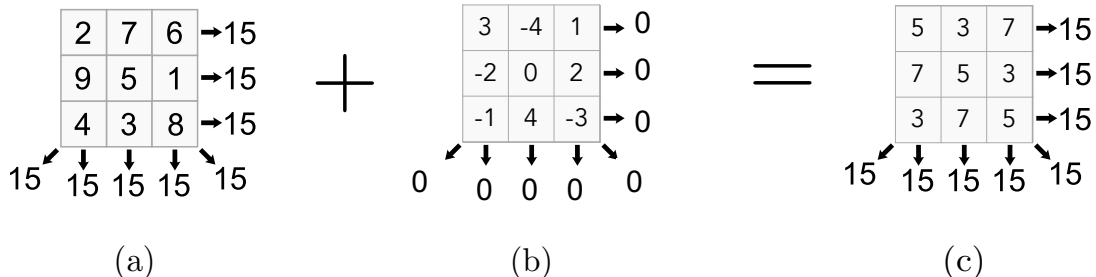


**Figure 4.1:** Magic Squares representing the effect of null strain fields.

This class of problem, for which a set of measurements have no unique solution, is relatively common. In fact, in some fields of research, characterisation and exploitation of a problem null space can be used for practical purposes, such as UAV fault detection [[26](#)].

In our case, however, this rank deficiency indicates that to achieve general tomographic reconstruction, we either require further problem constraints, or an alternative measurement model. A possible approach has been developed and investigated, and will be discussed in the coming chapters.

# Chapter 5

## A New Approach: Internal Strain Method

The boundary reconstruction approach described in the previous chapters is a viable means of reconstructing non-axisymmetric strain fields when compatibility of the elastic field can be ensured. To achieve reconstruction in the general case, however, a new method — dubbed the *Internal Strain Method* — has been developed, in which a sample may contain thermal or residual (Eigen) strains, leading to incompatibility.

In this chapter, we will discuss the formulation of this method, utilising the idealised integral model for a Bragg-Edge measurement as described in [chapter 1](#).

We again begin with a convex sample, in which a two-dimensional strain tensor field  $\epsilon(x, y)$  exists. The co-ordinate system adopted here is the same as that in [chapter 2](#), which referenced [Figure 1.9](#).

In this formulation, we do not preclude the presence of any Eigen-strains  $\epsilon_P(x, y)$ , however it is known that these do not play a part in our measurements. What matters is that an *elastic* field  $\epsilon_E(x, y)$  exists within the sample.

### 5.1 Non-Attenuated Measurement Model

As in [chapter 2](#), we begin by assuming that a neutron ray of infinitesimal width, and not subject to measurement noise and attenuation passes through the field.

Rather than discretise the sample boundary, as was previously done, we now discretise the field within the sample. Like a finite element model, the sample is divided into  $N$  rectangular voxels, with each assigned a constant elastic strain tensor  $\epsilon_i$ . The subscript  $i$  indexes each voxel (i.e.  $i = 1, 2, 3 \dots N$ ). One such discretisation is shown in [Figure 5.1](#).

As in previous formulations, we relate our Bragg-Edge measurements to the unknowns of our problem — here, the constant strain tensors at each voxel intersected by a ray. Initially, we will formulate this relationship by discretising the integral in terms of the

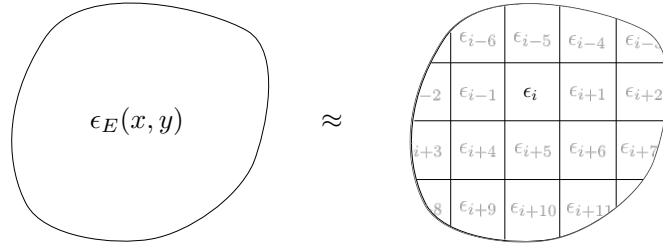


**Figure 5.1:** The elastic strain tensor field  $\epsilon_E(x, y)$  is discretised into a number of finite elements — called *voxels* — each said to posses a constant strain tensor.

constant strain tensor voxels encountered. Recall the integral model of a Bragg-Edge measurement from [chapter 1](#):

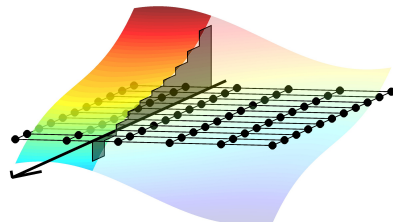
$$y = \frac{1}{L} \int_0^L \hat{\mathbf{n}}^\top \boldsymbol{\epsilon}(\mathbf{x}_0 + s\hat{\mathbf{n}}) \hat{\mathbf{n}} \, ds. \quad (1.8 \text{ revisited})$$

The *integrand* is essentially a surface of the form  $\hat{\mathbf{n}}^\top \boldsymbol{\epsilon}(\mathbf{x}_0 + s\hat{\mathbf{n}}) \hat{\mathbf{n}}$ . This surface can be imagined as a scalar field, which is different for each measurement direction (since  $\hat{\mathbf{n}}$  changes with direction). Geometrically, this line integral resembles the area of a fence extending from the  $(x, y)$  plane to the surface, over the line formed by the ray path. A visualisation of such a field over a rectangular sample discretised into square voxels is shown in the bottom of [Figure 5.2](#).

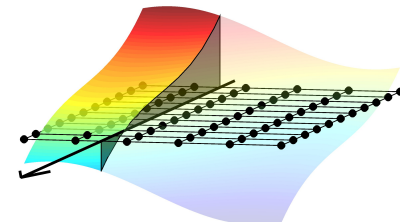
Our formulation discretises this integral in terms of the information stored in a finite number of intersected voxels. In this chapter, we will discuss two methods by which [Equation 1.8](#) may be related to the discrete intersected voxel strains  $\epsilon_i$ :

1. An *Euler* approximation to the integral, where (in a similar vein to a Riemann sum) the area of the ‘fence’ is approximated by the sum of a finite number of rectangular bars.
2. A *Trapezoidal* approximation to the integral, where the area is instead approximated by the sum of a number of trapezoidal bars, effectively modelling the space between discrete data points as straight lines.

Euler



Trapezoidal



→ Measurement Direction

Measurement Integrand

True Integrand

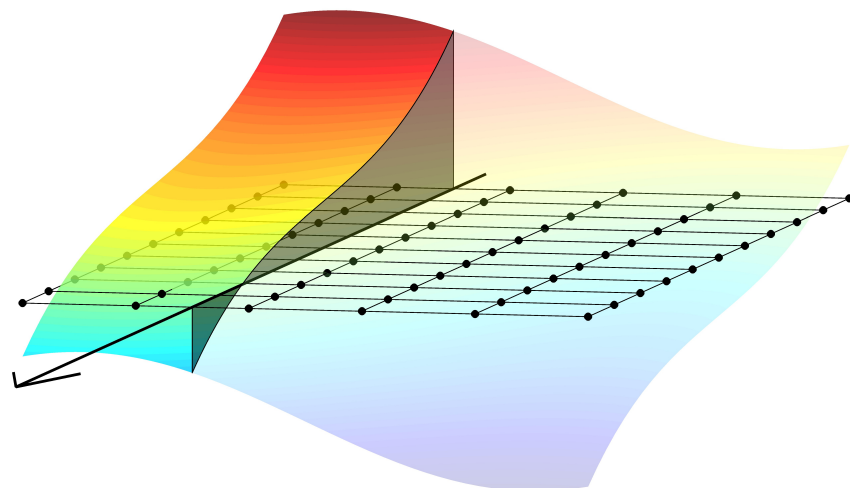


**Figure 5.2:** The integrand of a Bragg-Edge measurement is a scalar field, and the line integral measurement model essentially calculates the face area of a ‘fence’ formed between the  $(x, y)$  plane and the field magnitude along the ray path. Euler (top left) and Trapezoidal (top right) approximations to the integral can be seen.

### 5.1.1 Euler (Riemann Sum) Integral Approximation.

An Euler approximation to the integral is perhaps the simplest discretisation, with the form:

$$y \approx \frac{1}{L} \sum_{i \in M} \hat{\mathbf{n}}^\top \boldsymbol{\epsilon}_i \hat{\mathbf{n}} \Delta L_i \quad (5.1)$$

Where  $M$  is the set of all voxels intersected by a given measurement.  $\Delta L_i$  is the length of a voxel  $i$  that is irradiated by the neutron ray as it passes through it, as shown in Figure 5.3.

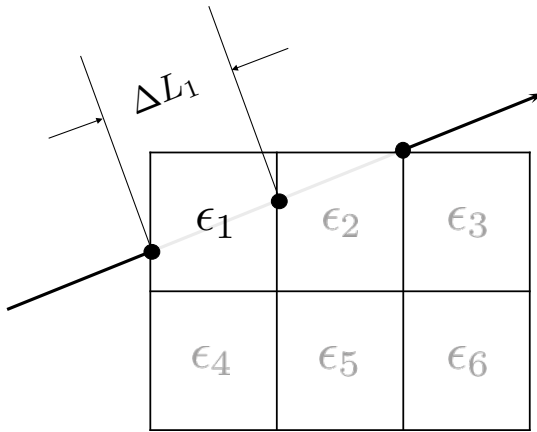


**Figure 5.3:** Each voxel intersected by the neutron ray has an associated irradiated length  $\Delta L$  that is included in the sum argument.

Let us begin by considering a simple example. Take the sample and discretisation shown in Figure 5.3. The ray here intersects voxels 1 and 2 — that is,  $M = \{1, 2\}$ . Thus, this measurement can be approximated by:

$$y \approx \frac{1}{L} \sum_{i \in \{1,2\}} \hat{\mathbf{n}}^\top \boldsymbol{\epsilon}_i \hat{\mathbf{n}} \Delta L_i \quad (5.2)$$

Expanding...

$$\begin{aligned} y &\approx \frac{1}{L} \left( \hat{\mathbf{n}}^\top \boldsymbol{\epsilon}_1 \hat{\mathbf{n}} \Delta L_1 + \hat{\mathbf{n}}^\top \boldsymbol{\epsilon}_2 \hat{\mathbf{n}} \Delta L_2 \right) \\ &\approx \frac{1}{L} \left( \Delta L_1 (\epsilon_{1xx} n_x^2 + 2\epsilon_{1xy} n_x n_y + \epsilon_{1yy} n_y^2) + \Delta L_2 (\epsilon_{2xx} n_x^2 + 2\epsilon_{2xy} n_x n_y + \epsilon_{2yy} n_y^2) \right) \end{aligned}$$

$$\approx \frac{1}{L} \begin{bmatrix} \Delta L_1 n_x^2 & 2\Delta L_1 n_x n_y & \Delta L_1 n_y^2 & \Delta L_2 n_x^2 & 2\Delta L_2 n_x n_y & \Delta L_2 n_y^2 \end{bmatrix} \begin{bmatrix} \epsilon_{1xx} \\ \epsilon_{1xy} \\ \epsilon_{1yy} \\ \epsilon_{2xx} \\ \epsilon_{2xy} \\ \epsilon_{2yy} \end{bmatrix}$$

As before, this represents one of a system of equations that can be generated by taking a number of measurements. This system of equations is of the form:

$$\mathbf{A}\boldsymbol{\varepsilon}_r = \mathbf{y} \quad (5.3)$$

Where  $\boldsymbol{\varepsilon}_r$  is a concatenated vector of unknown unique voxel strain components,  $\mathbf{y}$  is a vector of corresponding Bragg-Edge measurements, and  $\mathbf{A}$  is a co-efficient matrix that contains unit ray propagation direction vector components and irradiated voxel lengths. Like in the boundary reconstruction method,  $\mathbf{A}$  is a large, sparse co-efficient matrix (since only some of the total number of voxels can be irradiated by a single ray).

### 5.1.2 Trapezoidal Integral Approximation

Alternatively, a trapezoidal approximation to [Equation 1.8](#) can be used. We will discover that this only affects the construction of the problem  $\mathbf{A}$  matrix.

Almost as simple as the Euler approximation, the trapezoidal rule estimates the value of the integrand between discrete data points with a straight-line approximation. Without a doubt, more accurate numerical integration algorithms exist, but the trapezoidal rule is particularly useful here in its simplicity, and satisfies the requirements of variably spaced, discrete function evaluations.

Consider first a general example, where the integral to be performed is:

$$\int_a^b f(x) dx \quad (5.4)$$

This is shown graphically in [Figure 5.4](#).

For a series of  $N$  non uniformly sampled  $(x, y)$  pairs, the trapezoidal approximation to [Equation 5.4](#) can be written as:

$$\int_a^b f(x) dx \approx \frac{1}{2} \sum_{k=1}^{N-1} (x_{k+1} - x_k)(f(x_{k+1}) + f(x_k)) \quad (5.5)$$

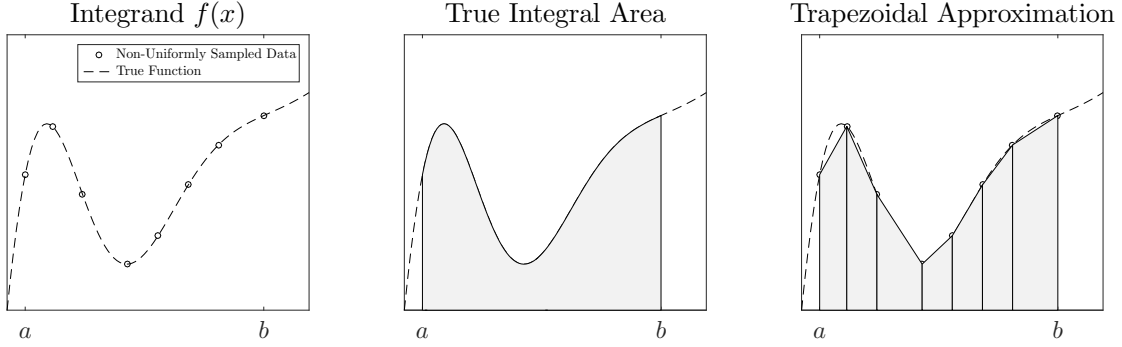


**Figure 5.4:** The trapezoidal provides a discrete approximation to the integral of  $f(x)$ .

This derivation will not be shown — an unsure reader is encouraged to revise the wealth of knowledge available online ([27] is an excellent resource).

As with the Euler method, the integral to be approximated is the familiar:

$$y = \frac{1}{L} \int_0^L \hat{\mathbf{n}}^\top \boldsymbol{\epsilon}(\mathbf{x}_0 + s\hat{\mathbf{n}})\hat{\mathbf{n}} \, ds. \quad (1.8 \text{ revisited})$$

Where now, the integrand function is  $\hat{\mathbf{n}}^\top \boldsymbol{\epsilon}(\mathbf{x}_0 + s\hat{\mathbf{n}})\hat{\mathbf{n}}$ , which is to be integrated over the variable  $s$ . That is:

$$f(s) = \hat{\mathbf{n}}^\top \boldsymbol{\epsilon}(\mathbf{x}_0 + s\hat{\mathbf{n}})\hat{\mathbf{n}} \quad (5.6)$$

and

$$y \approx \frac{1}{2L} \sum_{k=1}^{N-1} (s_{k+1} - s_k)(f(s_{k+1}) + f(s_k)) \quad (5.7)$$

Let us begin by deriving the equivalent trapezoidal approximation to this integral for the case where at least four voxels are irradiated by a neutron ray ( $N = 4$ ). Where more than four voxels are intersected, a similar pattern is followed. Suppose that we call the irradiated (intersected) voxels 1, 2, 3 and 4 — in the order they were intersected. The approximation is then of the form:

$$\begin{aligned} y &\approx \frac{1}{2L} \sum_{k=1}^3 (s_{k+1} - s_k) (f(s_{k+1}) + f(s_k)) \\ &\approx \frac{1}{2L} \left\{ \left[ (s_2 - s_1)(f(s_2) + f(s_1)) \right] + \left[ (s_3 - s_2)(f(s_3) + f(s_2)) \right] + \left[ (s_4 - s_3)(f(s_4) + f(s_3)) \right] \right\} \end{aligned}$$

$$\begin{aligned}
&\approx \frac{1}{2L} \left\{ f(s_1) \begin{bmatrix} s_2 - s_1 \end{bmatrix} + f(s_2) \begin{bmatrix} s_3 - s_2 + s_2 - s_1 \end{bmatrix} + f(s_3) \begin{bmatrix} s_4 - s_3 + s_3 - s_2 \end{bmatrix} + f(s_4) \begin{bmatrix} s_4 - s_3 \end{bmatrix} \right\} \\
&\approx \frac{1}{2L} \left\{ f(s_1) \begin{bmatrix} s_2 - s_1 \end{bmatrix} + f(s_2) \begin{bmatrix} s_3 - s_2 + s_2 - s_1 \end{bmatrix} + f(s_3) \begin{bmatrix} s_4 - s_3 + s_3 - s_2 \end{bmatrix} + f(s_4) \begin{bmatrix} s_4 - s_3 \end{bmatrix} \right\} \\
&\approx \frac{1}{2L} \left\{ f(s_1) \begin{bmatrix} s_2 - s_1 \end{bmatrix} + f(s_2) \begin{bmatrix} s_3 - s_1 \end{bmatrix} + f(s_3) \begin{bmatrix} s_4 - s_2 \end{bmatrix} + f(s_4) \begin{bmatrix} s_4 - s_3 \end{bmatrix} \right\}
\end{aligned}$$

In other words, there is a contribution for each intersected voxel. It can be shown that a pattern emerges for  $N \geq 2$  intersected voxels:

1. The first voxel intersected contributes  $f(s_1) \begin{bmatrix} s_2 - s_1 \end{bmatrix}$  to the sum.
2. The last ( $N^{\text{th}}$ ) voxel intersected contributes  $f(s_N) \begin{bmatrix} s_N - s_{N-1} \end{bmatrix}$  to the sum.
3. Any  $n^{\text{th}}$  voxel intersected (where  $2 < n < N$ ) contributes  $f(s_k) \begin{bmatrix} s_{k+1} - s_{k-1} \end{bmatrix}$  to the sum.

In the special case where only one voxel is intersected, the trapezoidal approximation simplifies to an Euler approximation.

Substituting [Equation 5.6](#) into our approximation:

$$\begin{aligned}
\epsilon_k \approx \frac{1}{2L} &\left\{ \hat{\mathbf{n}}^\top \boldsymbol{\epsilon}(\mathbf{x}_0 + s_1 \hat{\mathbf{n}}) \hat{\mathbf{n}} \begin{bmatrix} s_2 - s_1 \end{bmatrix} + \hat{\mathbf{n}}^\top \boldsymbol{\epsilon}(\mathbf{x}_0 + s_2 \hat{\mathbf{n}}) \hat{\mathbf{n}} \begin{bmatrix} s_3 - s_1 \end{bmatrix} \right. \\
&\left. + \hat{\mathbf{n}}^\top \boldsymbol{\epsilon}(\mathbf{x}_0 + s_3 \hat{\mathbf{n}}) \hat{\mathbf{n}} \begin{bmatrix} s_4 - s_2 \end{bmatrix} + \hat{\mathbf{n}}^\top \boldsymbol{\epsilon}(\mathbf{x}_0 + s_4 \hat{\mathbf{n}}) \hat{\mathbf{n}} \begin{bmatrix} s_4 - s_3 \end{bmatrix} \right\}
\end{aligned}$$

There is an element of choice in selecting which value of  $s$  is to be used for each voxel - that is,  $s_1 \dots s_4$ . A simple solution is to select the midway point of each intersected voxel, that is  $s_1 = 1/2\Delta L_1$ ,  $s_2 = \Delta L_1 + 1/2\Delta L_2$  and so on. Since the strain tensor within each voxel is assumed to be constant in this approximation, this choice has no effect on the evaluation of  $\hat{\mathbf{n}}^\top \boldsymbol{\epsilon}(\mathbf{x}_0 + s_k \hat{\mathbf{n}}) \hat{\mathbf{n}}$ .

Adopting the shorthand:

$$\hat{\mathbf{n}}^\top \boldsymbol{\epsilon}(\mathbf{x}_0 + s_k \hat{\mathbf{n}}) \hat{\mathbf{n}} = \hat{\mathbf{n}}^\top \boldsymbol{\epsilon}_k \hat{\mathbf{n}}$$

Then:

$$y \approx \frac{1}{2L} \left\{ \hat{\mathbf{n}}^\top \boldsymbol{\epsilon}_1 \hat{\mathbf{n}} \left[ \Delta L_1 + \frac{\Delta L_2}{2} - \left( \frac{\Delta L_1}{2} \right) \right] \right. \\ \left. + \hat{\mathbf{n}}^\top \boldsymbol{\epsilon}_2 \hat{\mathbf{n}} \left[ \Delta L_1 + \Delta L_2 + \frac{\Delta L_3}{2} - \left( \frac{\Delta L_1}{2} \right) \right] \right. \\ \left. + \hat{\mathbf{n}}^\top \boldsymbol{\epsilon}_3 \hat{\mathbf{n}} \left[ \Delta L_1 + \Delta L_2 + \Delta L_3 + \frac{\Delta L_4}{2} - \left( \Delta L_1 + \frac{\Delta L_2}{2} \right) \right] \right. \\ \left. + \hat{\mathbf{n}}^\top \boldsymbol{\epsilon}_4 \hat{\mathbf{n}} \left[ \Delta L_1 + \Delta L_2 + \Delta L_3 + \frac{\Delta L_4}{2} - \left( \Delta L_1 + \Delta L_2 + \frac{\Delta L_3}{2} \right) \right] \right\}$$

Which simplifies to:

$$y \approx \frac{1}{2L} \left\{ \hat{\mathbf{n}}^\top \boldsymbol{\epsilon}_1 \hat{\mathbf{n}} \left[ \frac{\Delta L_1 + \Delta L_2}{2} \right] + \hat{\mathbf{n}}^\top \boldsymbol{\epsilon}_2 \hat{\mathbf{n}} \left[ \frac{\Delta L_1}{2} + \Delta L_2 + \frac{\Delta L_3}{2} \right] \right. \\ \left. + \hat{\mathbf{n}}^\top \boldsymbol{\epsilon}_3 \hat{\mathbf{n}} \left[ \frac{\Delta L_2}{2} + \Delta L_3 + \frac{\Delta L_4}{2} \right] + \hat{\mathbf{n}}^\top \boldsymbol{\epsilon}_4 \hat{\mathbf{n}} \left[ \frac{\Delta L_3 + \Delta L_4}{2} \right] \right\}$$

Expanding the tensor product gives:

$$y \approx \frac{1}{2L} \left\{ \epsilon_{1xx} n_x^2 + 2\epsilon_{1xy} n_x n_y + \epsilon_{1yy} n_y^2 \left[ \frac{\Delta L_1 + \Delta L_2}{2} \right] \right. \\ \left. + \epsilon_{2xx} n_x^2 + 2\epsilon_{2xy} n_x n_y + \epsilon_{2yy} n_y^2 \left[ \frac{\Delta L_1}{2} + \Delta L_2 + \frac{\Delta L_3}{2} \right] \right. \\ \left. + \epsilon_{3xx} n_x^2 + 2\epsilon_{3xy} n_x n_y + \epsilon_{3yy} n_y^2 \left[ \frac{\Delta L_2}{2} + \Delta L_3 + \frac{\Delta L_4}{2} \right] \right. \\ \left. + \epsilon_{4xx} n_x^2 + 2\epsilon_{4xy} n_x n_y + \epsilon_{4yy} n_y^2 \left[ \frac{\Delta L_3 + \Delta L_4}{2} \right] \right\}$$

And (for brevity) defining the constant terms for each voxel as:

$$\begin{aligned}\alpha_1 &= \frac{1}{2} (\Delta L_1 + \Delta L_2) \\ \alpha_2 &= \Delta L_2 + \frac{1}{2} (\Delta L_1 + \Delta L_3) \\ \alpha_3 &= \Delta L_3 + \frac{1}{2} (\Delta L_2 + \Delta L_4) \\ \alpha_4 &= \frac{1}{2} (\Delta L_3 + \Delta L_4)\end{aligned}$$

We can then write a single Bragg-Edge measurement as:

$$\frac{1}{2L} \begin{bmatrix} \alpha_1 n_x^2 & 2\alpha_1 n_x n_y & \alpha_1 n_y^2 & \alpha_2 n_x^2 & 2\alpha_2 n_x n_y & \alpha_2 n_y^2 & \alpha_3 n_x^2 & 2\alpha_3 n_x n_y & \alpha_3 n_y^2 & \alpha_4 n_x^2 & 2\alpha_4 n_x n_y & \alpha_4 n_y^2 \end{bmatrix} \begin{bmatrix} \epsilon_{1xx} \\ \epsilon_{1xy} \\ \epsilon_{1yy} \\ \epsilon_{2xx} \\ \epsilon_{2xy} \\ \epsilon_{2yy} \\ \epsilon_{3xx} \\ \epsilon_{3xy} \\ \epsilon_{3yy} \\ \epsilon_{4xx} \\ \epsilon_{4xy} \\ \epsilon_{4yy} \end{bmatrix}$$

As before, the above forms one row of the system of equations generated by taking many measurements over many projection directions. A measurement that intersects less or more voxels is similar. Of course, at least as many unique measurements must be taken (rows generated) as unknown voxel strain components exist within the sample, and care must be taken in the construction of the very sparse  $\mathbf{A}$  matrix to ensure that elements of  $\mathbf{A}$  are assigned to their corresponding strain tensor component in  $\boldsymbol{\epsilon}_r$ .

## 5.2 Simulation and Analysis

To compare the effectiveness of this method against the successful Boundary Reconstruction approach, the cantilevered beam problem and associated parameters were maintained as per [chapter 3](#). Again, the absence of appropriate experimental data has led to the simulation of Bragg-Edge measurements through a fabricated strain field. To eliminate issues encountered with the finite resolution interpolation obtained from

FEA based strain field characterisations, the analytical solution to the problem strain field was utilised:

$$\begin{aligned}\epsilon_{xx}(x, y) &= \frac{P}{EI}(l - x)y \\ \epsilon_{xy}(x, y) &= -\frac{(1 + \nu)P}{2EI} \left( \left(\frac{h}{2}\right)^2 - y^2 \right) \\ \epsilon_{yy}(x, y) &= -\frac{\nu P}{EI}(l - x)y\end{aligned}$$

In implementing this method, the simulation measurement environment required modification to capture information necessary to formulate the  $\mathbf{A}$  matrix. Namely, the intersect finding code has been modified to detect intermediate intersections of a neutron ray with voxel boundaries within the sample internals.

First, we discuss the simulation results in the absence of attenuation, with additional problem constraints specified with the aim of achieving convergence, before discussing the effects of attenuation on the uniqueness of solutions.

As before, the convergence of the reconstruction algorithm as a function of the number of projections taken was observed. In this implementation, compatibility constraints were not enforced, and in the absence of additional information, the routine was unable to converge within the vicinity of a correct solution, even with up to ten times more measurements than unknowns.

Examination of the singular values of the formulated  $\mathbf{A}$  matrix confirmed that, as predicted by Lionheart and Withers [25], the transform (and consequently the discretised problem) has a sizeable null space.

It was determined that despite there being many more measurements than unknowns, the problem  $\mathbf{A}$  matrix was rank deficient, meaning that a family of solutions existed that fit the measurements equally well (within a tolerance band).

### 5.3 Additional Constraints

As a result of the rank-deficiency of the problem, additional constraints were implemented in an attempt to achieve reconstruction of the physical strain field. In keeping with our goal of achieving general tomographic reconstruction, these methods do not enforce or exploit compatibility or axisymmetry.

### 5.3.1 Coupled Optimisation: Strain Energy Minimisation

All elastic strain fields, compatible or not, must obey the principle of minimum potential energy. Recall that as a body is deformed elastically, energy is stored as the atomic structure is stretched or compressed. This principle ensures that the way in which the system behaves minimises this stored energy at all times.

Since only a conceptual understanding is required here, we will not delve too far into detail. The (complicated) tensor equation that characterises this energy storage can take many forms, depending on the engineering assumptions made.

Let us consider one such form — a 2D (Plane Stress) situation, in which an element is subject to a general stress state, such as in [Figure 5.5](#). Here, normal and shear stresses are present. Strain energy  $W_0$  (which will from now be described as an energy density — that is, normalised by volume) is stored due to normal loading in the  $x$  direction as:

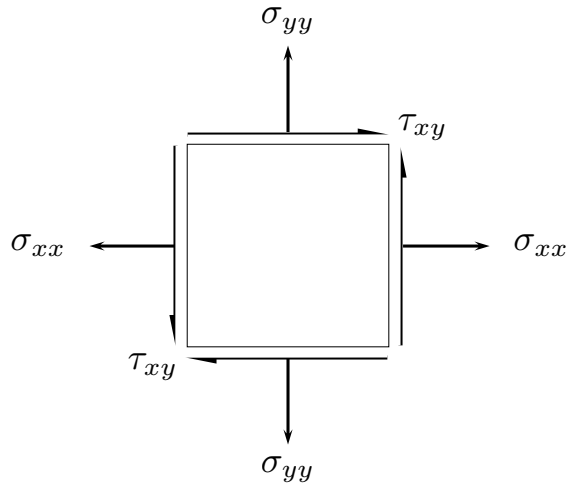


**Figure 5.5:** A plane-stress element in a general loading scenario.

$$W_{0x} = \frac{1}{2} \sigma_{xx} \epsilon_{xx} \quad (5.8)$$

and due to normal loading in the  $y$  direction as:

$$W_{0y} = \frac{1}{2} \sigma_{yy} \epsilon_{yy}. \quad (5.9)$$

Energy is also stored due to the presence of shear strains, as:

$$W_{0xy} = \frac{1}{2} \tau_{xy} \gamma_{xy}. \quad (5.10)$$

Where the engineering shear strain  $\gamma_{xy} = 2\epsilon_{xy}$ .

Under general plane-stress loading, the strain energy (density) within an element is given by:

$$W_0 = \frac{1}{2} (\sigma_{xx}\epsilon_{xx} + \sigma_{yy}\epsilon_{yy} + \tau_{xy}\gamma_{xy}) \quad (5.11)$$

Hooke's law (under plane stress conditions) allows us to write the normal and shear stresses in terms of their corresponding strains, by:

$$\sigma_{xx} = \frac{E}{1-\nu^2}(\epsilon_{xx} + \nu\epsilon_{yy}) \quad (5.12)$$

and

$$\sigma_{yy} = \frac{E}{1-\nu^2}(\epsilon_{yy} + \nu\epsilon_{xx}) \quad (5.13)$$

and

$$\tau_{xy} = G\gamma_{xy}. \quad (5.14)$$

Substituting these relations into [Equation 5.11](#) yields:

$$\begin{aligned} W_0 &= \frac{1}{2} \left( \left( \frac{E}{1-\nu^2}(\epsilon_{xx} + \nu\epsilon_{yy}) \right) \epsilon_{xx} + \left( \frac{E}{1-\nu^2}(\epsilon_{yy} + \nu) \right) \epsilon_{yy} + (G\gamma_{xy}) \gamma_{xy} \right) \\ &= \frac{1}{2} \left( \frac{E}{1-\nu^2} (\epsilon_{xx}^2 + 2\nu\epsilon_{xx}\epsilon_{yy} + \epsilon_{yy}^2) + G\gamma_{xy}^2 \right) \end{aligned}$$

Finally, the shear modulus  $G$  can be written in terms of  $E$  and  $\nu$  [28]. This gives the following expression for strain energy:

$$\begin{aligned} W_0 &= \frac{1}{2} \left( \frac{E}{1-\nu^2} (\epsilon_{xx}^2 + 2\nu\epsilon_{xx}\epsilon_{yy} + \epsilon_{yy}^2) + \frac{E}{2(1+\nu)} \gamma_{xy}^2 \right) \\ &= \frac{E}{2(1+\nu)} \left( \frac{1}{1-\nu} (\epsilon_{xx}^2 + 2\nu\epsilon_{xx}\epsilon_{yy} + \epsilon_{yy}^2) + 2\epsilon_{xy}^2 \right) \quad (5.15) \end{aligned}$$

The strain energy density (as expressed in [Equation 5.15](#)) can be written in terms of the unknown strains in a voxel  $i$  as:

$$W_{0i} = \frac{E}{2(1+\nu)} \begin{pmatrix} [\epsilon_{ixx} & \epsilon_{ixy} & \epsilon_{iyy}] & \begin{bmatrix} \frac{1}{1-\nu} & 0 & \frac{\nu}{1-\nu} \\ 0 & 2 & 0 \\ \frac{\nu}{1-\nu} & 0 & \frac{1}{1-\nu} \end{bmatrix} & [\epsilon_{ixx} \\ \epsilon_{ixy} \\ \epsilon_{iyy}] \end{pmatrix} \quad (5.16)$$

An optimisation routine that utilised this additional objective in hope of reconstructing a discretised strain field has been implemented. The approach taken involves solving the problem using *quadratic programming*. Problems of this nature are usually written as:

$$\operatorname{argmin}_{\mathbf{x}} \quad \frac{1}{2} \mathbf{x}^T \mathbf{H} \mathbf{x} + \mathbf{f}^T \mathbf{x} \quad (5.17)$$

Where  $\mathbf{x}$  is a vector of variables to be determined,  $\mathbf{H}$  is a symmetric matrix (called a *Hessian*), and  $\mathbf{f}$  is vector.  $\mathbf{H}$  and  $\mathbf{f}$  specify quadratic and linear cost functions respectively. In our case,  $\mathbf{x}$  is the vector of voxel centroid strains  $\boldsymbol{\epsilon}_r$ .

The simplest approach by which to solve our problem via quadratic programming is to minimise the measurement residual in a least squares sense, while also implementing a cost on the minimisation of strain energy. The residual minimisation term of linear system of equations can be written as:

$$\mathbf{H}_R = 2\mathbf{A}^T \mathbf{A} \quad (5.18)$$

and

$$\mathbf{f}_R^T = -2\mathbf{y}^\top \mathbf{A} \quad (5.19)$$

This derivation has been covered extensively in literature [29]. Additionally, we can utilise [Equation 5.16](#) to write the strain energy (density) of each voxel in a form suitable for quadratic programming.

It can be shown that the strain energy density for the entire system can be written as one block diagonal matrix, with the entries being strain matrices of the form [Equation 5.16](#):

$$\mathbf{H}_S = \frac{2E}{2(1+\nu)} \times \begin{bmatrix} \begin{bmatrix} \frac{1}{1-\nu} & 0 & \frac{\nu}{1-\nu} \\ 0 & 2 & 0 \\ \frac{\nu}{1-\nu} & 0 & \frac{1}{1-\nu} \end{bmatrix} & & 0 \\ & \ddots & \\ 0 & & \begin{bmatrix} \frac{1}{1-\nu} & 0 & \frac{\nu}{1-\nu} \\ 0 & 2 & 0 \\ \frac{\nu}{1-\nu} & 0 & \frac{1}{1-\nu} \end{bmatrix} \end{bmatrix} \quad (5.20)$$

Then, the strain energy density of the entire system can be written as:

$$W_0 = \frac{1}{2} \boldsymbol{\varepsilon}_r^T \mathbf{H}_S \boldsymbol{\varepsilon}_r \quad (5.21)$$

A weighted sum of the Hessian matrices for least-squares residual minimisation and strain energy minimisation can then be taken to formulate the quadratic programming optimisation problem:

$$\operatorname{argmin}_{\boldsymbol{\varepsilon}_r} \quad \frac{1}{2} \boldsymbol{\varepsilon}_r^T (\mathbf{H}_R + w \mathbf{H}_S) \boldsymbol{\varepsilon}_r + (-2 \mathbf{y}^T \mathbf{A}) \boldsymbol{\varepsilon}_r \quad (5.22)$$

Where  $w$  is a regularisation weighting parameter that weights the emphasis of the optimisation.

The MATLAB intrinsic `quadprog` engine was used to implement this multi-objective optimisation. The routine was unable to converge to the physical strain field solution. It was found that results were extremely sensitive to the value of the weighting parameter  $w$ . With careful tuning, stain fields exhibiting relative error in the order of 40% could be obtained. It was determined that poor conditioning of the problem precluded the success of this approach. Here, a trade-off existed between the two objectives being optimised — least squares fitting of a solution to the measurements and strain energy minimisation.

### 5.3.2 Null Space Characterisation via Singular Value Decomposition

Recall from [chapter 4](#) that any solution  $\boldsymbol{\varepsilon}_r$  that fits the measurements can be written as the superposition of the true solution  $\boldsymbol{\varepsilon}_t$  and a strain field from the null space  $\boldsymbol{\varepsilon}_n$  (as per [section 4.3](#)).

An alternative approach was developed in the hope of isolating and removing this null component  $\boldsymbol{\varepsilon}_n$  from  $\boldsymbol{\varepsilon}_r = \boldsymbol{\varepsilon}_t + \boldsymbol{\varepsilon}_n$ .

A vector space of dimension  $n$  can be characterised by  $n$  linearly independent vectors that span the space, called a basis. Singular Value Decomposition is one method by which the basis vectors of the null space of our problem can be identified. It can be shown that any matrix  $\mathbf{A}$  of dimensions  $m \times n$  can be written in a factored form:

$$\mathbf{A} = \mathbf{U}\Sigma\mathbf{V}^T \quad (5.23)$$

By definition,  $\Sigma$  is an  $n \times n$  diagonal matrix. The elements on the diagonal are the so-called singular values of  $\mathbf{A}$ .

Analogous to eigenvalues, singular values of zero magnitude indicate rank deficiency (or *singularity*). The more zero magnitude singular values present, the greater the rank-deficiency (equivalently: the larger the null space).

We will not detail the process by which the matrices  $\mathbf{U}$ ,  $\Sigma$  and  $\mathbf{V}$  are obtained — the interested reader is encouraged to visit resources such as [30] to learn more. We are however greatly interested in the following property:

The columns of  $\mathbf{V}$  (rows of  $\mathbf{V}^T$ ) which correspond to *zero magnitude* singular values form an orthonormal basis for the null space of  $\mathbf{A}$ . This means that if we find  $\mathbf{V}^T$  by singular value decomposition, its rows — vectors we will call  $v_1 \dots v_n$ , which form an orthonormal basis for the null space — can be extracted and utilised in the isolation and removal of the null space solution component  $\boldsymbol{\varepsilon}_r$ .

The process was as follows:

1. Obtain a solution that fits the measurements via LSQR. This solution  $\boldsymbol{\varepsilon}_r$  is known to be a superposition of the true solution  $\boldsymbol{\varepsilon}_t$  and a contribution from the null space  $\boldsymbol{\varepsilon}_n$ .
2. Perform the following optimisation to minimise strain energy:

$$\underset{\{\beta_1 \dots \beta_n\}}{\operatorname{argmin}} \quad \left( \boldsymbol{\varepsilon}_r - (\beta_1 \mathbf{v}_1 + \dots + \beta_n \mathbf{v}_n) \right)^T \mathbf{H}_S \left( \boldsymbol{\varepsilon}_r - (\beta_1 \mathbf{v}_1 + \dots + \beta_n \mathbf{v}_n) \right) \quad (5.24)$$

3. Obtain the true solution by:

$$\boldsymbol{\varepsilon}_t = \boldsymbol{\varepsilon}_r - (\beta_1 \mathbf{v}_1 + \dots + \beta_n \mathbf{v}_n) \quad (5.25)$$

The intrinsic MATLAB `svd` function was used to perform a singular value decomposition on the problem  $\mathbf{A}$  matrix. The basis vectors for the kernel of  $\mathbf{A}$  ( $\mathbf{v}_1 \dots \mathbf{v}_n$ ) were then extracted. The intrinsic `fmincon` optimisation engine was utilised to perform the optimisation in [Equation 5.24](#).

Unfortunately, the implementation was unable to converge within the vicinity of a correct solution. In an effort to troubleshoot, the validity of the method was checked by altering the optimisation to see whether (given perfect knowledge of the true solution) this approach could isolate the null component of the solution for removal.

Here the difference between the (known) true solution  $\boldsymbol{\epsilon}_t$  and reconstructed solution  $\boldsymbol{\epsilon}_r$  was utilised as a cost function, such that the second stage of the optimisation was as follows:

$$\operatorname{argmin}_{\{\beta_1 \dots \beta_n\}} \|\boldsymbol{\epsilon}_t - \boldsymbol{\epsilon}_r - (\beta_1 \mathbf{v}_1 + \dots + \beta_n \mathbf{v}_n)\|_2$$

Even with this information, the algorithm was unable to isolate the null component. Further investigation revealed that mesh refinement significantly affected the resemblance of the discretised problem ( $\mathbf{A}$  matrix) null space to that of the transform.

The conclusion reached was that our problem was ill-posed, namely in that:

1. Significant mesh refinement was necessary to ensure resemblance and convergence of the null component removal optimisation routine.
2. In refining the reconstruction mesh, significantly more unknowns were introduced to the initial measurement-based optimisation.
3. The introduction of more unknowns meant that many more measurements were required to allow LSQR to converge to a solution.
4. The discrete nature of these additional measurements introduced contradiction in the  $\mathbf{A}$  matrix (as several rays could pass through the same voxels but give different measurements, especially in areas of high strain gradients).
5. This contradiction reduced the ability of LSQR to converge to a correct solution, precluding the determination of  $\boldsymbol{\epsilon}_t$  even if  $\boldsymbol{\epsilon}_n$  was found.

This trade-off in stability between routines and lack of convergence precluded achievement of a less erroneous reconstruction, and indicated that this approach was not practical.

## 5.4 Conclusions

As predicted by Lionheart and Withers [25], our discretised transform was found to have a sizeable null space. Unfortunately, efforts to work around this null space were largely

in vain, with the numerical nature of our simulation environment largely precluding this approach.

In the following chapter, we will discuss a method by which the attenuation of a neutron ray as it passes through sample may be used to develop a more sophisticated measurement model, with a far smaller kernel.



# Chapter 6

## Attenuated Bragg-Edge Reconstruction

With attempts to work around the sizeable null space of [Equation 1.8](#) largely fruitless, we will now turn our attention toward an alternative approach. In this chapter, we will discuss the utilisation of a measurement model that incorporates the effects of ray attenuation, in the hope that this may help to trivialise the null space.

### 6.1 Conceptual Introduction

Recall that the key result from Lionheart and Withers [\[25\]](#) was that the null space of [Equation 1.8](#) encompasses — at the very least — all fixed-boundary strain fields. The presence of attenuation removes the symmetry that makes this claim possible. Consider, for example the  $\epsilon_{xx}$  component of a fixed-boundary strain field shown in [Figure 6.1](#).

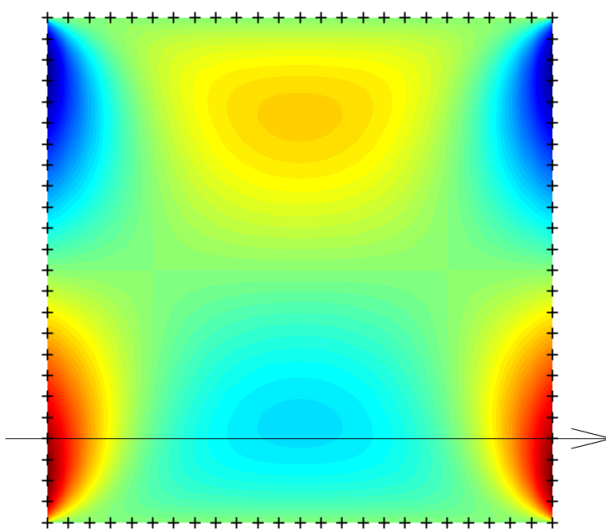


**Figure 6.1:** This fixed boundary strain field is in the kernel of [Equation 1.8](#), meaning that any measurement of that form through this field (such as the one shown by the black arrow) will have zero magnitude.

This field was generated by applying a gravitational force to a fixed-boundary strain field. Simulated Bragg-Edge measurements of this field with varying levels of attenuation applied are shown as integrals in [Figure 6.2](#).

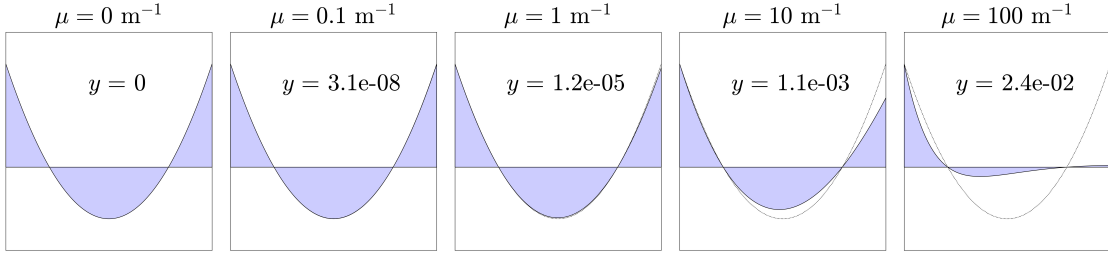


**Figure 6.2:** Increasing the amount of attenuation changes the magnitude of a Bragg-Edge measurement significantly, preventing fixed-boundary strain fields lying in the null of the transform.

Where  $\mu = 0 \text{ m}^{-1}$ , the simulated Bragg-Edge measurement is (as predicted by Lionheart and Withers) zero magnitude. As the attenuation co-efficient is increased, it can be seen that the magnitude of the simulated measurement deviates from this ideal value, with the transform no longer mapping to zero under the same strain field conditions at high attenuation levels.

Additionally, as the amount of attenuation present is increased, only the strains close to the ray entry have a significant effect on the *magnitude* of a measurement.

At this stage, attempts to conclusively, mathematically prove that attenuation trivialises the transform kernel have not been successful. However, it is clear that the null space of such a transform must be smaller than that of [Equation 1.8](#), as the class of fixed-boundary strain fields that were previously in the kernel map to non-zero magnitudes at appreciable levels of attenuation.

## 6.2 Problem Formulation

With the aim of utilising attenuation in reconstruction, minor modification to the Internal Strain Method formulation is required. Recall from [chapter 3](#) that an attenuated Bragg-Edge measurement can be modelled as:

$$y = \frac{1}{\int_0^L \chi(s) \, ds} \int_0^L \chi(s) \hat{\mathbf{n}}^\top \boldsymbol{\epsilon}(\mathbf{x}_0 + s\hat{\mathbf{n}}) \hat{\mathbf{n}} \, ds. \quad (3.6 \text{ revisited})$$

Repeating the derivation from [chapter 5](#) for this attenuated model gives an Euler approximation to the integral of:

$$y \approx \frac{\mu}{1 - \chi(L)} \sum_{i \in M} \chi(s_i) \hat{\mathbf{n}}^\top \boldsymbol{\epsilon}_i \hat{\mathbf{n}} \Delta L_i. \quad (6.1)$$

And a trapezoidal approximation of:

$$y \approx \frac{\mu}{2(1 - \chi(L))} \sum_{k=1}^{N-1} (s_{k+1} - s_k) (\chi(s_{k+1}) \hat{\mathbf{n}}^\top \boldsymbol{\epsilon}_{k+1} \hat{\mathbf{n}} + \chi(s_k) \hat{\mathbf{n}}^\top \boldsymbol{\epsilon}_k \hat{\mathbf{n}}). \quad (6.2)$$

As before, these derivations allow for a system of equations relating the Bragg-Edge measurements to the unknown voxel strains to be constructed. The key difference here is that for the first time, our method is utilising ray attenuation to help solve for an unknown strain field, rather than working in spite of it.

### 6.3 Simulation and Analysis

The Internal Strain Method, now utilising the attenuated measurement model ([Equation 3.6](#)) and associated  $\mathbf{A}$  matrix construction was implemented in the reconstruction of the cantilevered beam strain field. No additional constraints (strain energy minimisation, null space characterisation, compatibility or axisymmetry) were specified. After obtaining promising initial results with the Euler routine, the more complicated trapezoidal formulation was implemented, with minor modification to capture information extending to the ray boundary.

A mesh independence study was conducted, and the reconstruction mesh refined until convergence was observed at a resolution of  $80 \times 40$  (horizontal  $\times$  vertical) square voxels, each of characteristic length 0.25 mm. Simulation results were far more promising than those obtained in the previous chapter, and convergence with respect to number of projections taken for varying levels of attenuation observed. These results are shown in [Figure 6.3](#).

It was observed that increasing the magnitude of the attenuation applied resulted in faster convergence to a less erroneous solution. It is suspected that this behaviour is due to the numerical nature of the simulation environment.

With increasing attenuation, the problem becomes more and more well posed, as strain fields that were previously in the kernel of the unattenuated transform no longer fit the measurements (as was shown in [Figure 6.2](#)).

Holistically, it has been observed that over the length of the cantilevered beam, for example, significant attenuation is required to ensure that strain measurements taken with an attenuated model differ significantly from those taken with an unattenuated model. In other words, significant attenuation is required before this alternative model can appreciably reduce the size of the null space.

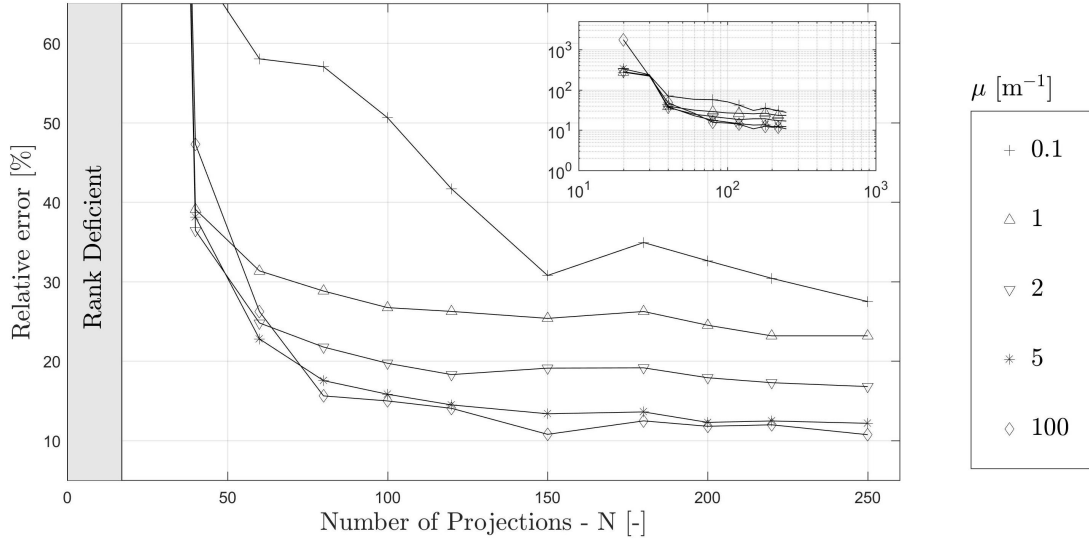


**Figure 6.3:** Convergence of the reconstruction algorithm was observed in the presence of attenuation.

Further intuition about the effects of attenuation can be gained by qualitatively examining the reconstruction. The reconstruction for  $\mu = 0.1$  (an almost negligible amount of attenuation), at  $N = 250$  projections is shown in [Figure 6.4](#).

### 6.3.1 Reconstruction Results

Much of the nearly 30% relative error observed in this reconstruction (as defined in [chapter 3](#), was in the shear component,  $\epsilon_{xy}$ . Since any measurement in the  $x$  direction contributes information that directly helps to resolve the  $\epsilon_{xx}$  strains, and any measurement in the  $y$  direction acts in a similar way, it is no surprise that the reconstructed shear component (which is never ‘seen’ by itself by a measurement) displays the most error.

Further investigation revealed that the problem  $\mathbf{A}$  matrix at this level of attenuation was still rank-deficient. Suspecting that insufficient attenuation had been applied to trivialise the problem null space, simulated measurements of the reconstruction error fields  $\boldsymbol{\varepsilon}_t - \boldsymbol{\varepsilon}_r$  (on the right of [Figure 6.4](#)) were performed.

These measurements revealed that the error fields for this reconstruction bear close resemblance to those in the kernel of the unattenuated transform, with 90% of these measurements being at least three orders of magnitude lower than the strains in the sample<sup>1</sup>, as shown in [Figure 6.5](#).

---

<sup>1</sup>To be in the kernel of the unattenuated transform, these fields should give rise to zero-magnitude measurements, but here numerical error and remaining non-convergence are also contributing to the error seen.

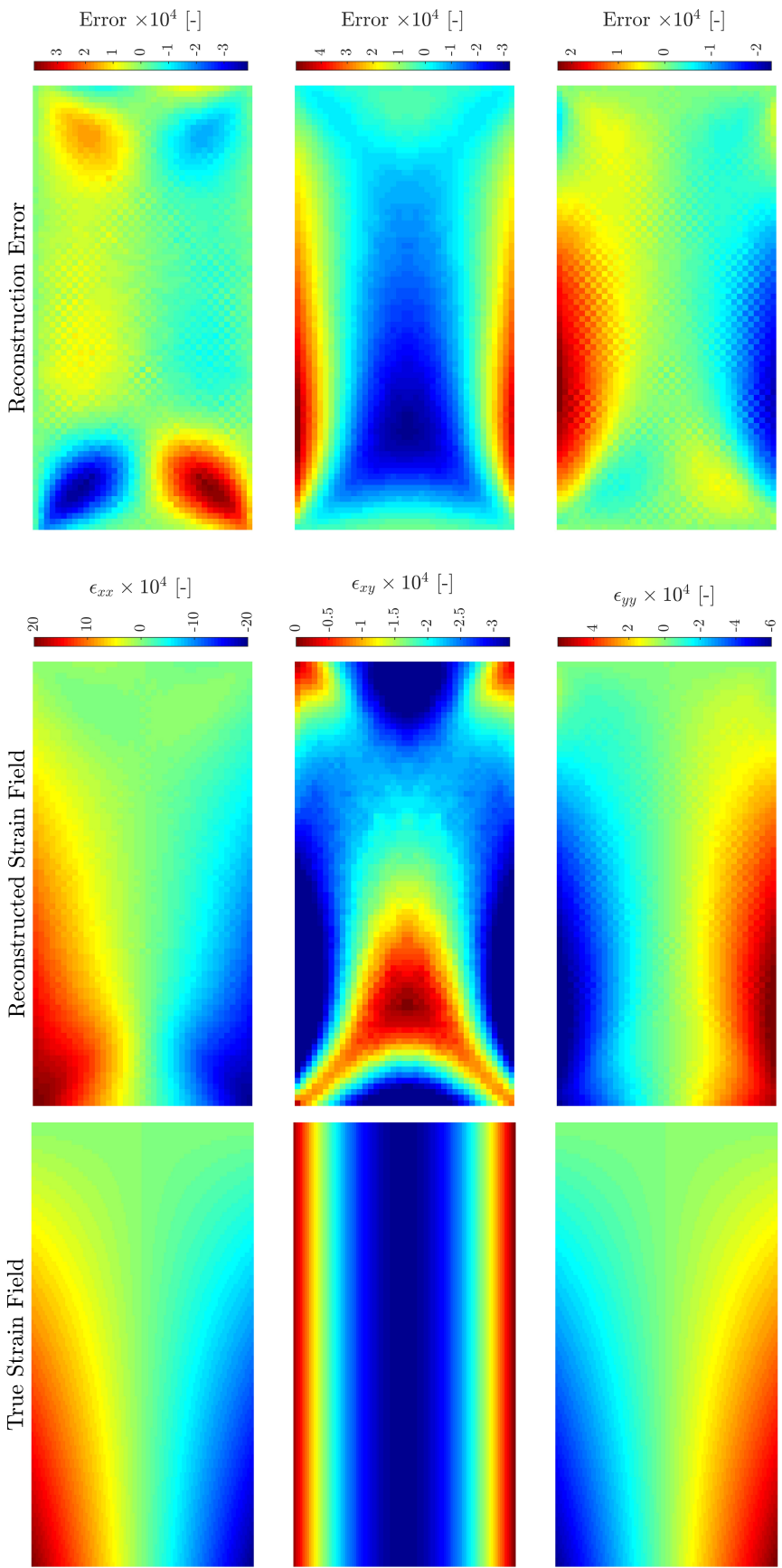
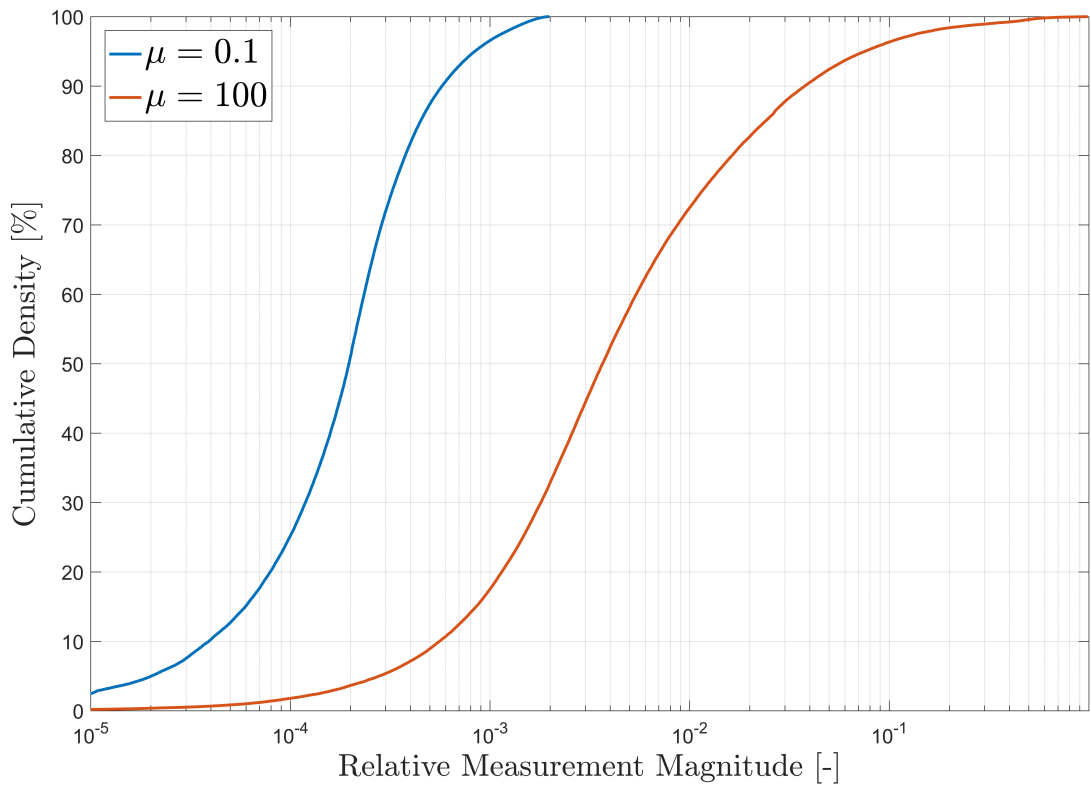


Figure 6.4: Left: True and Reconstructed cantilevered beam  $\epsilon_{xx}$ ,  $\epsilon_{xy}$  and  $\epsilon_{yy}$  strain field components. Right: Reconstruction error fields

As the magnitude of attenuation was increased, a significant change in the structure and magnitude of the reconstruction error was observed. The reconstruction results for  $\mu = 100$ , and  $N = 250$  projections (where a total reconstruction relative error of approximately 10% was seen), are shown in [Figure 6.6](#).

While quantitatively, significantly lower error was seen in the reconstruction at this higher level of attenuation, the error fields that remained still exhibited the behaviour of those in the kernel of the unattenuated transform, though an appreciable change in the proportion of ‘apparently null’ measurements was observed. For this level of attenuation, only 20% of measurements were at least three orders of magnitude lower than the strains present in the sample, though 70 % were at least two orders of magnitude smaller (as shown in [Figure 6.5](#)).

It is suspected that as the magnitude of attenuation is increased, the condition of our problem improves rapidly, up to a limit, where the impact of the unattenuated transform null space is greatly reduced. It is believed that the numerical nature of the reconstruction precludes elimination of this ill conditioning.



**Figure 6.5:** Cumulative density function showing the relative magnitude of measurements through the reconstruction error fields to that of measurements through the sample strain field.

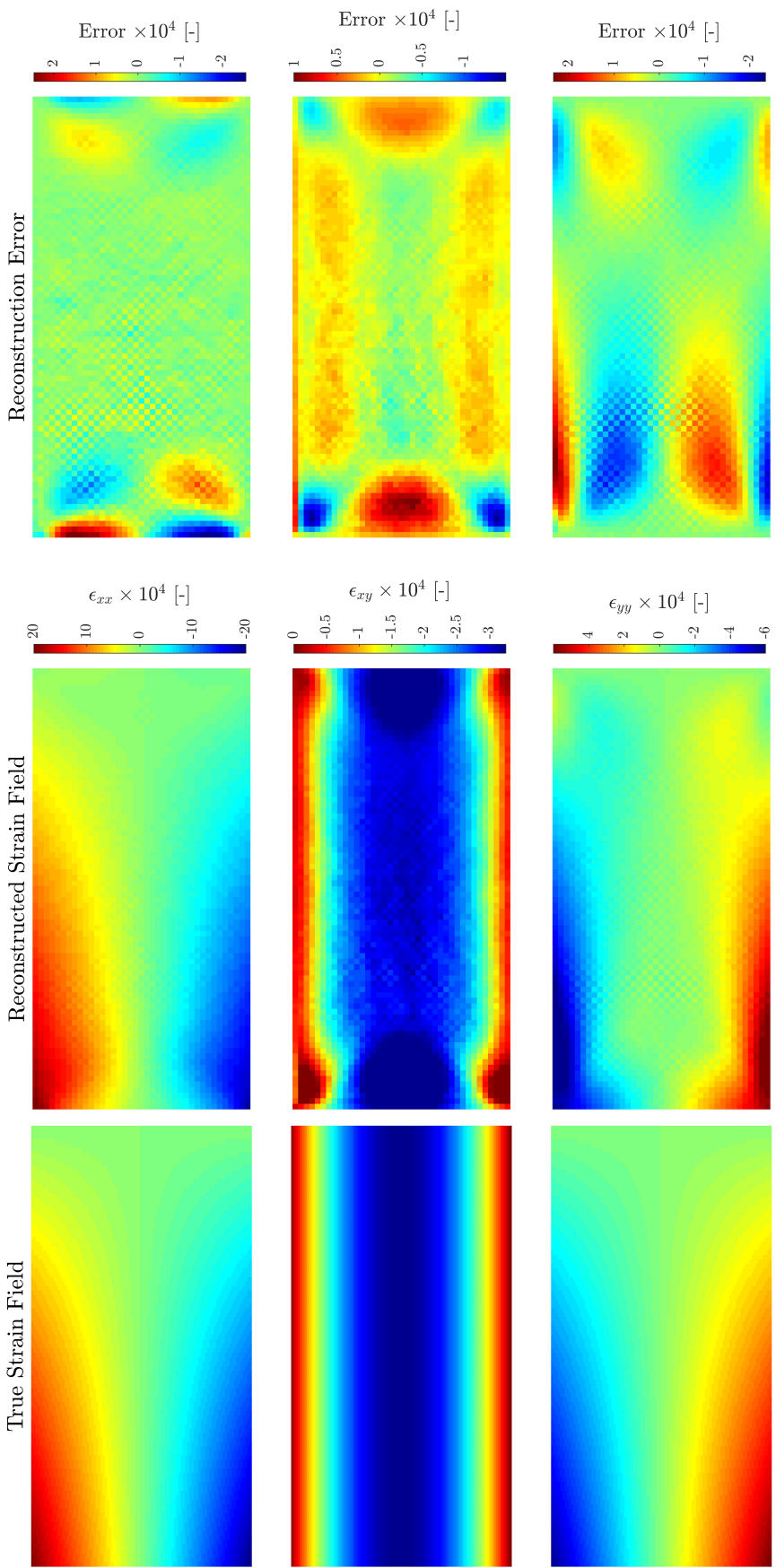


Figure 6.6: As the magnitude of attenuation is increased, the reconstruction error fields (right) undergo significant changes.

## 6.4 Error Field Compatibility

With simulation results potentially providing the clearest picture of the null space to date, further study of the reconstruction error fields was undertaken. Of particular interest was the compatibility of these (seemingly) null fields, as previously published results [25, 18] have led to the suspicion that the null space of the unattenuated transform consists of compatible strain fields. Recall from [chapter 4](#) that in a 2D, plane stress situation, a strain field is said to be compatible if it satisfies:

$$2\frac{\partial^2 \epsilon_{xy}}{\partial x \partial x} - \frac{\partial^2 \epsilon_{xx}}{\partial y^2} - \frac{\partial^2 \epsilon_{yy}}{\partial x^2} = 0 \quad (4.2 \text{ revisited})$$

A measure of incompatibility was thus defined as:

$$I(x, y) = 2\frac{\partial^2 \epsilon_{xy}}{\partial x \partial y} - \frac{\partial^2 \epsilon_{xx}}{\partial y^2} - \frac{\partial^2 \epsilon_{yy}}{\partial x^2}. \quad (6.3)$$

With  $I(x, y) = 0$  characteristic of a compatible field. To enable comparisons between strain fields of different magnitudes, a measure of relative incompatibility  $I_r(x, y)$  was defined, whereby  $I(x, y)$  was scaled by the maximum strain gradient in the field under study.

### 6.4.1 Numerical Differentiation

Numerical differentiation of the reconstruction error fields was required to calculate  $I_r(x, y)$ . A central difference routine was first utilised in an attempt to perform the required derivatives, and a validation simulation was conducted by calculating the relative incompatibility of the cantilevered beam sample strain field, as defined in [chapter 5](#)<sup>2</sup>.

Unfortunately, this method displayed significant deviation from the expected zero value (largely at the strain field concavity change along the beam centreline).

In an effort to achieve a more valid estimate of incompatibility, an alternative approach was taken. Drawing inspiration from a method outlined in [31], an algorithm was developed that fits piecewise quadratic surfaces to sections of a strain field, for which analytical derivatives could be evaluated. Surfaces fit were of the form:

---

<sup>2</sup>It can be shown that this strain field is compatible by taking the appropriate partial derivatives of the analytical expressions.

$$\begin{aligned}\epsilon_{xx}(x, y) &= a_{xx} + b_{xx}x + c_{xx}y + d_{xx}x^2 + e_{xx}y^2 + f_{xx}xy \\ \epsilon_{xy}(x, y) &= a_{xy} + b_{xy}x + c_{xy}y + d_{xy}x^2 + e_{xy}y^2 + f_{xy}xy \\ \epsilon_{yy}(x, y) &= a_{yy} + b_{yy}x + c_{yy}y + d_{yy}x^2 + e_{yy}y^2 + f_{yy}xy\end{aligned}$$

Such that the appropriate derivatives could be taken as multiples of the fit co-efficients:

$$\begin{aligned}\frac{\partial^2 \epsilon_{xx}}{\partial y^2} &= 2e_{xx} \\ \frac{\partial^2 \epsilon_{yy}}{\partial x^2} &= 2d_{yy} \\ \frac{\partial^2 \epsilon_{xy}}{\partial x \partial y} &= f_{xy}\end{aligned}$$

The fitting process is shown in [Figure 6.7](#), where 16 surrounding voxels are used to evaluate the numerical derivatives of the shown component of strain at the highlighted node (in red).

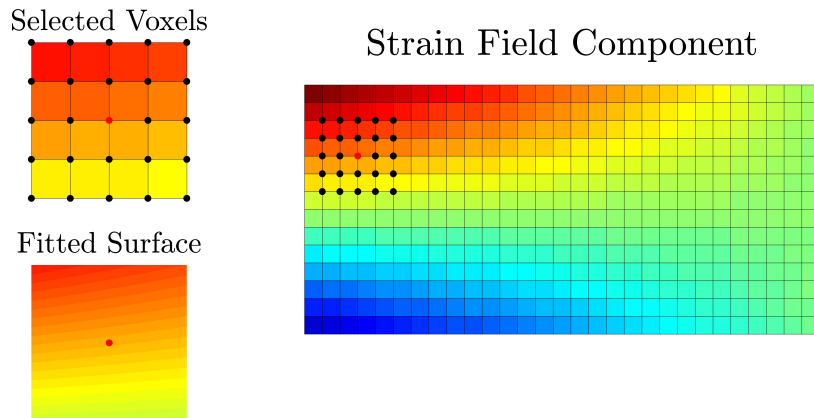


**Figure 6.7:** The numerical derivative algorithm developed works by fitting surfaces to localised segments of the strain field.

Results obtained with this new routine were very promising, calculating a maximum relative incompatibility significantly closer to the theoretical prediction than that from the central difference routine.

The true relative incompatibility field  $I_r(x, y)$ , and those predicted by the central difference and curve-fitting routines for this validation are shown in [Figure 6.8](#). The improvement in calculated incompatibility between methods can be seen. Note that neglecting the peak areas where strain field concavity change occurs, the maximum relative incompatibility seen was in the order of  $1 \times 10^{-9}$ .

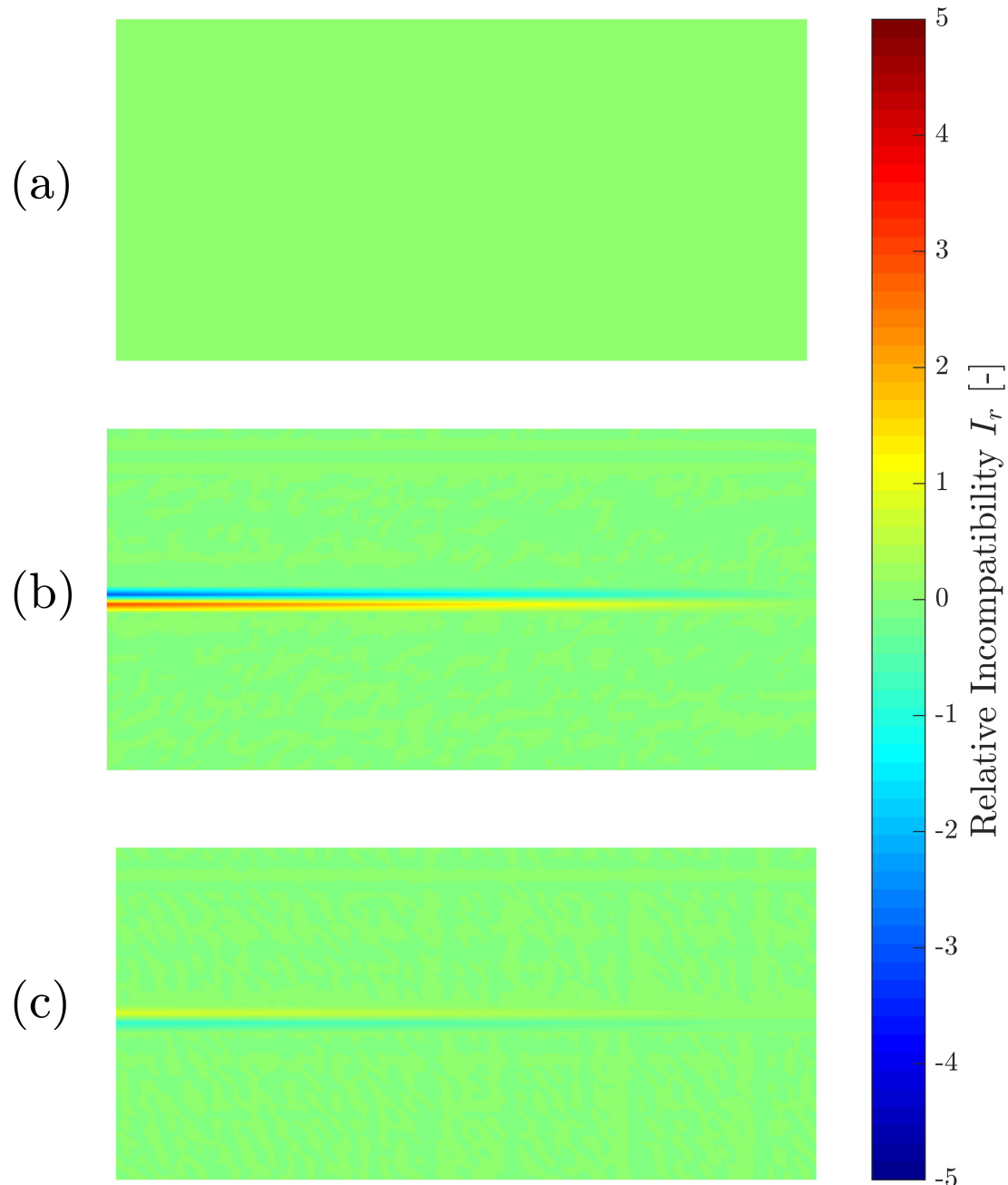


**Figure 6.8:** Relative Incompatibility of the cantilevered beam strain field. (a) True solution. (b) Solution found by central difference algorithm. (c) Solution found by curve-fitting.

Following this validation, the incompatibility of the reconstruction error field for  $\mu = 0.1$  and  $N = 250$  projections was evaluated. It was found that this (null) field was comparably compatible, with maximum relative incompatibility  $I_r$  in the order of  $1 \times 10^{-6}$  observed. Further reduction in this incompatibility was observed with more projections taken (as the reconstruction converged further, though diminishing returns were seen).

With this discovery lending credence to the suspicion that fields in the kernel of the unattenuated transform are compatible, a second case study was examined to further examine this hypothesis.

## 6.5 Reconstruction Results: Incompatible Strain Field

A fabricated, incompatible strain field of the following form was next reconstructed:

$$\begin{aligned}\epsilon_{xx} &= 8000y^3 \\ \epsilon_{xy} &= 4.45(x + y)^2 \\ \epsilon_{yy} &= 1000x^3\end{aligned}$$

The co-ordinate system and problem geometry of the cantilevered beam were maintained. Co-efficients of this strain field were selected so as to ensure that strains in the order of  $1 \times 10^{-3}$  (similar magnitudes to the cantilevered beam problem) were seen. The incompatibility of this strain field can be shown analytically:

$$\begin{aligned}I(x, y) &= 2 \frac{\partial^2 \epsilon_{xy}}{\partial x \partial y} - \frac{\partial^2 \epsilon_{xx}}{\partial y^2} - \frac{\partial^2 \epsilon_{yy}}{\partial x^2} \\ &= 2(2 \times 4.45) - (6 \times 8000y) - (6 \times 1000x) \\ &\neq 0(x, y)\end{aligned}$$

The incompatibility of this field was confirmed by the numerical differentiation algorithms described in the previous section, and the relative incompatibility  $I_r(x, y)$  is shown in [Figure 6.9](#). Interestingly, the central difference routine was again proved invalid as it indicated that this field was largely compatible, while the curve fitting routine arrived at a solution very close to the analytical result.

The attenuated measurement model and Internal Strain Method were used to reconstruct this strain field, and simulations were run until convergence with respect to the number of projections taken was achieved ( $N = 250$ ). The reconstruction results are shown in [Figure 6.10](#).

As with the cantilevered beam example, more than 80 % of simulated measurements through the reconstruction error fields were at least three orders of magnitude smaller than the strains under study, suggesting again that the error fields seen were from the null space of the unattenuated transform. Again supporting the suspicion that null space strain fields are compatible, numerical differentiation of these error fields revealed a relative incompatibility in the order of  $1 \times 10^{-8}$ .

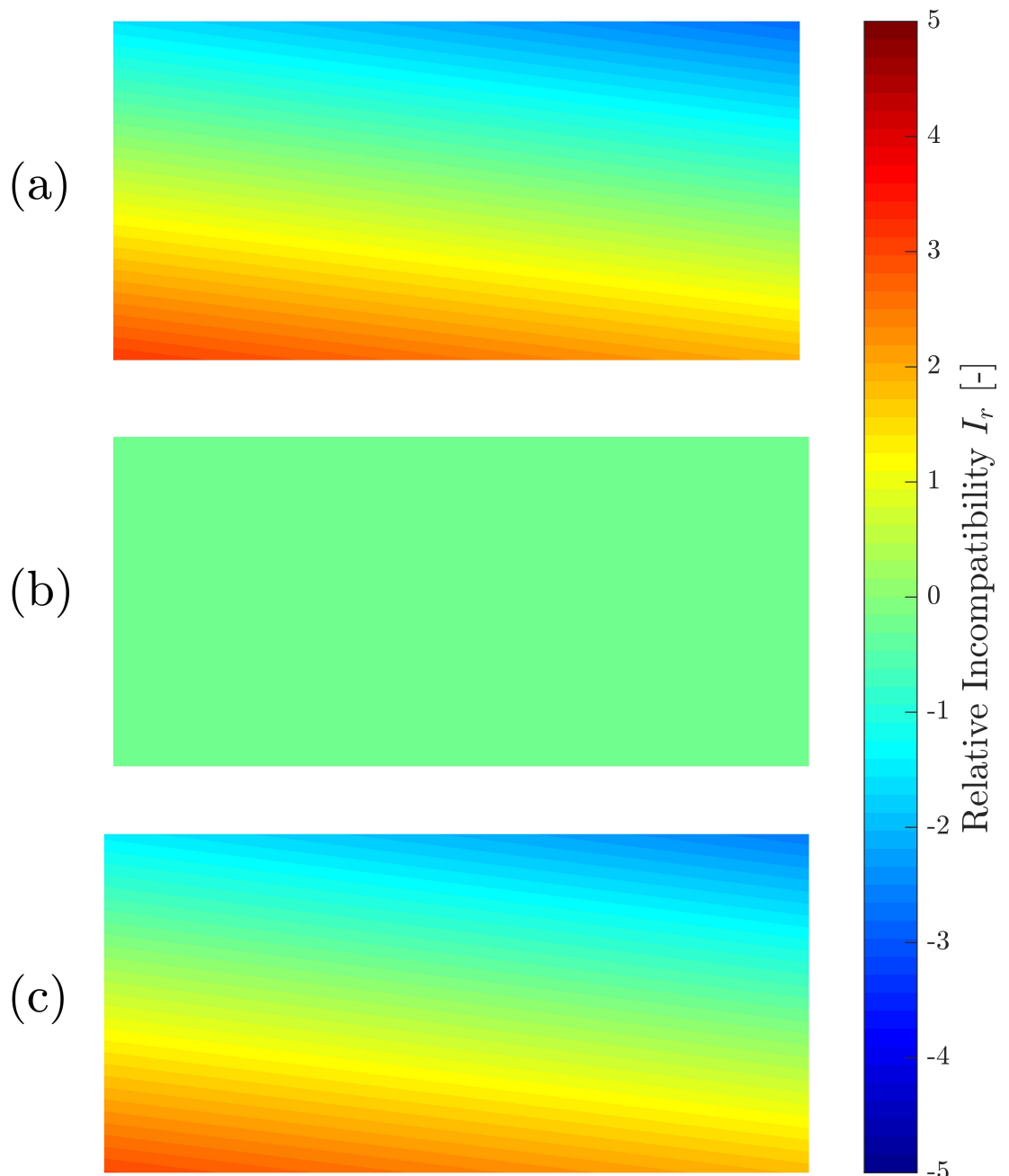


**Figure 6.9:** Relative Incompatibility of the known-incompatible strain field. (a) True solution. (b) Solution found by central difference algorithm (clearly incorrect). (c) Solution found by curve-fitting.

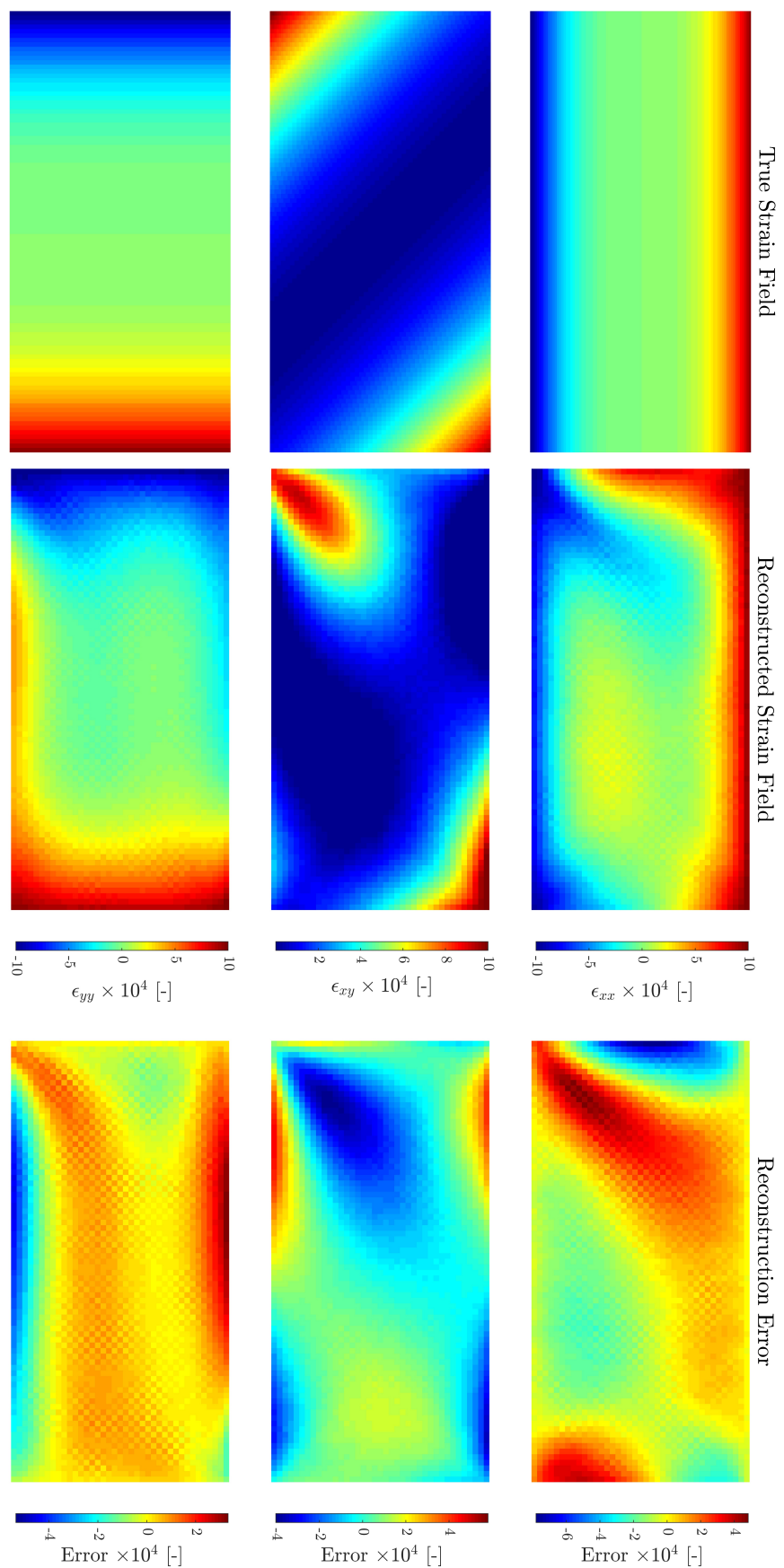


Figure 6.10: Reconstruction of an incompatible strain field has been achieved in the presence of attenuation.

### 6.5.1 Reconstruction Results: Experimental Nonideality

The poor conditioning of our problem, even at high levels of attenuation, has severely impacted the ability of the reconstruction algorithm to converge in the presence of experimental nonideality.

While ray attenuation is being utilised to obtain a solution, convergence in the presence of experimental uncertainty has also been evaluated.

Initial studies undertaken indicated that the convergence of the algorithm was highly sensitive to this nonideality. Reconstructions were observed to display relative error in the order of 40% for both the cantilevered beam and incompatible strain field examples in the presence of expected experimental uncertainty ( $\sigma = 1 \times 10^{-4}$ ).

This result largely precludes application of this method in achieving strain field reconstruction with real experimental measurements.

## 6.6 Conclusions

Unfortunately, the Internal Strain Method has not shown promise as a practical approach for reconstructing unknown strains from experimental data. However, simulated reconstruction of a non-axisymmetric, incompatible elastic strain field, has significantly extended upon the existing capability of Bragg-Edge neutron strain tomography.

While the poor conditioning of our problem has precluded reconstruction with less than 10% relative error, it was found that the errors seen were largely from the null space of the unattenuated transform. This result has allowed us to observe the null space with an unprecedented resolution, and incompatibility studies support the hypothesis that fields in this space are compatible.

There is much work yet to be done to confirm this hypothesis, however; if found to be true, this result will largely pave the way for future approaches to strain tomography.



## Chapter 7

# Conclusions, Future Work

This project represents a significant extension to the body of knowledge concerning Bragg-Edge neutron strain tomography, with a number of key results obtained. With a scarcity of experimental data in existence, significant effort has been expended in the development of a numerical environment in which Bragg-Edge measurements can be simulated.

By first applying a number of limiting assumptions, we were able to reconstruct an elastic strain field within a sample subject only to in-situ loadings by relating (simulated) Bragg-Edge measurements to the deformation of the sample boundary. Reconstruction results were extremely promising, with minimal systematic error observed in validation studies. While only applicable to a limited number of cases, this approach has shown great promise and robustness in the face of experimental nonideality (noise, attenuation, ray width). The results of this work have resulted in a journal article co-authored by the author of this thesis. This article has been accepted and published [17], and is included in [Appendix B](#).

To further validate this method, it is to be used to attempt strain field reconstruction from experimental data collected at a suitable Neutron source in Japan in December 2016. If successful, this will be the first time that a reconstruction of this kind will have been achieved. This work will form the basis of postgraduate studies in the future.

Additionally, significant progress has been made toward general tomographic reconstruction in this project. Initial attempts to achieve simulated general tomographic reconstruction centred around implementing additional physical constraints (such as strain energy minimisation) to help isolate and remove the effects of the problem null space as described by Lionheart and Withers [25]. These attempts were largely unsuccessful, with the numerical nature of the simulation environment precluding accurate characterisation of the problem kernel.

However, by implementing a reconstruction measurement model that incorporated information about ray attenuation, simulated reconstruction of an incompatible, non-axisymmetric strain field has, for the first time been achieved. The developed method

requires no additional problem constraints (such as strain energy minimisation, axisymmetry or compatibility). This algorithm has shown promise in the successful reconstruction of strain in the absence of experimental nonideality, and has provided an unprecedented view of the null space of our reconstruction problem.

Initial analysis of the problem kernel lends credence to the suspicion that fields in the kernel of our transform are compatible. Following these results, future research in this area will begin with an alternative characterisation of the kernel, obtained via finite-element solution of the fixed-boundary membrane natural modes of a sample under study. These studies will also form the basis of postgraduate studies going forward.

Unfortunately, as a consequence of the poor conditioning of the problem, our algorithm was unable to reconstruct studied strain fields, in the presence of simulated experimental uncertainty, meaning that it is largely non-viable for experimental data. The results of this work have formed the basis of a second journal article, which has been submitted for publication. A copy of this manuscript, which is in the process of being submitted, is included in [Appendix C](#).

While not described in detail in the body of this thesis, a major component of this project has been the development of the Bragg-Edge measurement simulation environment. More than 60 MATLAB scripts and functions have been written to simulate Bragg-Edge strain tomography. In doing so, problems such as the implementation of the STRAND7 API, generation of measurement geometry, the efficient detection of ray-sample intersections, construction of sparse co-efficient matrices, optimisation and linear systems analysis, numerical differentiation and integration and null space characterisation have been approached.

A comprehensive library of MATLAB code has been uploaded to the git repository for this project, which can be accessed via the project supervisor ([christopher.wensrich@newcastle.edu.au](mailto:christopher.wensrich@newcastle.edu.au)).

# References

- [1] M. I. Friswell and J. E. Mottershead. *Finite Element Modelling*, pages 7–35. Springer Netherlands, Dordrecht, 1995. ISBN 978-94-015-8508-8. doi: 10.1007/978-94-015-8508-8\_2. URL [http://dx.doi.org/10.1007/978-94-015-8508-8\\_2](http://dx.doi.org/10.1007/978-94-015-8508-8_2).
- [2] Data Aquisition Systems Engineering. Temperature effects in strain measurement, 2013. URL <https://ueidaq.files.wordpress.com/2013/08/strain-gauge-figure1.jpg>.
- [3] Michael Eckhert. Max von laue and the discovery of x-ray diffraction in 1912. *Annalen der physik*, 524(5):83–85, 2012.
- [4] W. H. Bragg and W. L. Bragg. The reflection of x-rays by crystals. *Proceedings of the Royal Society of London A: Mathematical, Physical and Engineering Sciences*, 88(605):428–438, 1913. ISSN 0950-1207. doi: 10.1098/rspa.1913.0040. URL <http://rspa.royalsocietypublishing.org/content/88/605/428>.
- [5] C. M. Wensrich, E. H. Kisi, V. Luzin, and O. Kirstein. Non-contact measurement of the stress within granular materials via neutron diffraction. *AIP Conference Proceedings*, 1542(1):441–444, 2013. doi: <http://dx.doi.org/10.1063/1.4811962>. URL <http://scitation.aip.org/content/aip/proceeding/aipcp/10.1063/1.4811962>.
- [6] C. M. Wensrich, E. H. Kisi, and V. Luzin. Non-contact stress measurement in granular materials via neutron and x-ray diffraction: theoretical foundations. *Granular Matter*, 15(3):275–286, 2013. ISSN 1434-7636. doi: 10.1007/s10035-013-0416-x. URL <http://dx.doi.org/10.1007/s10035-013-0416-x>.
- [7] P Kesavan Nair and R Vasudevan. Residual stresses of types ii and iii and their estimation. *Sadhana*, 20(1):39–52, 1995.
- [8] J. K. Cockcroft. Monochromators, 2006. URL <http://pd.chem.ucl.ac.uk/pdnn/inst1/monoc.htm>.
- [9] Erich H Kisi and Christopher J Howard. *Applications of neutron powder diffraction*, volume 15. Oxford University Press, 2012.

- [10] U.S Food and Drug Administration. Medical x-ray imaging - what is computed tomography?, 2016. URL <http://www.fda.gov/Radiation-EmittingProducts/RadiationEmittingProductsandProcedures/MedicalImaging/MedicalX-Rays/ucm115318.htm>. chapter1.
- [11] Marv Ruona. New dual head ct, January 13 2016. URL <http://www.artandsciencegraphics.com/wp-content/uploads/2014/09/New-Dual-Head-CT.jpg>. chapter1.
- [12] National Institute of Biomedical Imaging and Bioengineering. Computed tomography (ct) — national institute of biomedical imaging and bioengineering, 2012. URL <http://www.ncbi.nlm.nih.gov/pubmed/>. chapter1.
- [13] Phidaux. Magic square example, April 6 2008. URL <https://commons.wikimedia.org/wiki/File:Magicsquareexample.svg>. chapter1.
- [14] American Association of Physicists in Medicine. Tomographic image reconstruction, 1999. URL <https://www.aapm.org/meetings/99AM/pdf/2806-57576.pdf>. chapter1.
- [15] Jeremy Karl Cockcroft and Simon Jaques. Production of spallation neutrons, 2006. URL <http://pd.chem.ucl.ac.uk/pdnn/inst3/pulsed.htm>. chapter1.
- [16] Hirotaka Sato, Takashi Kamiyama, and Yoshiaki Kiyanagi. A rietveld-type analysis code for pulsed neutron bragg-edge transmission imaging and quantitative evaluation of texture and microstructure of a welded. alpha.-iron plate. *Materials transactions*, 52(6):1294–1302, 2011. ISSN 1345-9678. chapter1.
- [17] C.M. Wensrich, J.N. Hendriks, A. Gregg, M.H. Meylan, V. Luzin, and A.S. Tremsin. Bragg-edge neutron transmission strain tomography for in situ loadings. *Nuclear Instruments and Methods in Physics Research Section B: Beam Interactions with Materials and Atoms*, 383:52 – 58, 2016. ISSN 0168-583X. doi: <http://dx.doi.org/10.1016/j.nimb.2016.06.012>. URL <http://www.sciencedirect.com/science/article/pii/S0168583X16302774>.
- [18] CM Wensrich, JN Hendriks, and MH Meylan. Bragg edge neutron transmission strain tomography in granular systems. *Strain*, 52(1):80–87, 2016.
- [19] Christopher C Paige and Michael A Saunders. Lsqr: An algorithm for sparse linear equations and sparse least squares. 1982.
- [20] Paul Sherrrer Insitute. Thermal neutron data. URL [https://www.psi.ch/niag/LinksEN/Thermal\\_Attenu\\_Coeff.pdf](https://www.psi.ch/niag/LinksEN/Thermal_Attenu_Coeff.pdf).
- [21] Brian Abbey, Shu Yan Zhang, Wim.J.J. Vorster, and Alexander M. Korsunsky. Feasibility study of neutron strain tomography. *Procedia Engineering*, 1(1):185 – 188,

2009. ISSN 1877-7058. doi: <http://dx.doi.org/10.1016/j.proeng.2009.06.043>. URL <http://www.sciencedirect.com/science/article/pii/S1877705809000447>.
- [22] Brian Abbey, Shu Yan Zhang, Wim Vorster, and Alexander M. Korsunsky. Reconstruction of axisymmetric strain distributions via neutron strain tomography. *Nuclear Instruments and Methods in Physics Research Section B: Beam Interactions with Materials and Atoms*, 270:28 – 35, 2012. ISSN 0168-583X. doi: <http://dx.doi.org/10.1016/j.nimb.2011.09.012>. URL <http://www.sciencedirect.com/science/article/pii/S0168583X11008767>.
  - [23] Henry J Kirkwood, Brian Abbey, Harry M Quiney, Shu Yan Zhang, Anton S Tremsin, and Alexander Korsunsky. Bragg edge neutron strain tomography.
  - [24] Henry J. Kirkwood, Shu Yan Zhang, Anton S. Tremsin, Alexander M. Korsunsky, Nikolaos Baimpas, and Brian Abbey. Neutron strain tomography using the radon transform. *Materials Today: Proceedings*, 2:S414 – S423, 2015. ISSN 2214-7853. doi: <http://dx.doi.org/10.1016/j.matpr.2015.05.057>. URL <http://www.sciencedirect.com/science/article/pii/S2214785315001285>.
  - [25] W R B Lionheart and P J Withers. Diffraction tomography of strain. *Inverse Problems*, 31(4):045005, 2015. URL <http://stacks.iop.org/0266-5611/31/i=4/a=045005>.
  - [26] Johannes Hendriks. *Null Space Signal Injection for Fault Diagnosis*. PhD thesis, The University of Newcastle, 2014.
  - [27] Erik Talvila and Matthew Wiersma. A simple derivation of the trapezoidal rule for numerical integration. 2012.
  - [28] J. Salencon. *Handbook of Continuum Mechanics: General Concepts - Thermoelasticity*. Physics and astronomy online library. Springer, 2001. ISBN 9783540414438. URL <https://books.google.com.au/books?id=H3xIED8ctfUC>.
  - [29] Eric B. Laber & Hua Zhou. Advanced computing, February 2013. URL <http://www.stat.ncsu.edu/people/zhou/courses/st810/notes/lect09QP.pdf>.
  - [30] Singular value decomposition, Fall 2011. URL [http://ocw.mit.edu/courses/mathematics/18-06sc-linear-algebra-fall-2011/positive-definite-matrices-and-applications/singular-value-decomposition/MIT18\\_06SCF11\\_Ses3.5sum.pdf](http://ocw.mit.edu/courses/mathematics/18-06sc-linear-algebra-fall-2011/positive-definite-matrices-and-applications/singular-value-decomposition/MIT18_06SCF11_Ses3.5sum.pdf).
  - [31] H.B. Said T.N.T. Goodman and L.H.T. Chang. Local derivative estimation for scattered data interpolation. *Applied Mathematics and Computation*, 68(1):41 – 50, 1995. ISSN 0096-3003. doi: [http://dx.doi.org/10.1016/0096-3003\(94\)00086-J](http://dx.doi.org/10.1016/0096-3003(94)00086-J). URL <http://www.sciencedirect.com/science/article/pii/009630039400086J>.



# Appendices



## Appendix A

# Turnitin Originality Report

Gregg\_Thesis

ORIGINALITY REPORT

% 13	% 4	% 10	% 3
SIMILARITY INDEX	INTERNET SOURCES	PUBLICATIONS	STUDENT PAPERS

PRIMARY SOURCES

- |   |   |      |
|---|---|------|
| 1 | Wensrich, C.M., J.N. Hendriks, A. Gregg, M.H. Meylan, V. Luzin, and A.S. Tremsin. "Bragg-edge neutron transmission strain tomography for in situ loadings", Nuclear Instruments and Methods in Physics Research Section B Beam Interactions with Materials and Atoms, 2016. | % 10 |
|   | Publication   |      |
| 2 | www.engineersaustralia.org.au   | % 2  |
|   | Internet Source   |      |

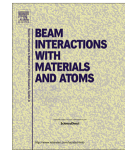
EXCLUDE QUOTES OFF  
EXCLUDE OFF  
BIBLIOGRAPHY

EXCLUDE MATCHES < 2%



## **Appendix B**

# **Boundary Reconstruction Paper**



## Bragg-edge neutron transmission strain tomography for *in situ* loadings



C.M. Wensrich <sup>a,\*</sup>, J.N. Hendriks <sup>a</sup>, A. Gregg <sup>a</sup>, M.H. Meylan <sup>b</sup>, V. Luzin <sup>c</sup>, A.S. Tremsin <sup>d</sup>

<sup>a</sup>School of Engineering, The University of Newcastle, Callaghan, NSW 2308, Australia

<sup>b</sup>School of Mathematical and Physical Sciences, The University of Newcastle, Callaghan, NSW 2308, Australia

<sup>c</sup>Bragg Institute, Australian Nuclear Science and Technology Organisation (ANSTO), Kirrawee, NSW 2232, Australia

<sup>d</sup>Space Sciences Laboratory, University of California, Berkeley, CA 94720, USA

### ARTICLE INFO

#### Article history:

Received 6 May 2016

Received in revised form 17 June 2016

Accepted 19 June 2016

#### Keywords:

Strain tomography

Bragg-edge imaging

Neutron diffraction

Neutron transmission strain measurement

### ABSTRACT

An approach for tomographic reconstruction of three-dimensional strain distributions from Bragg-edge neutron transmission strain images is outlined and investigated. This algorithm is based on the link between Bragg-edge strain measurements and the Longitudinal Ray Transform, which has been shown to be sensitive only to boundary displacement. By exploiting this observation we provide a method for reconstructing boundary displacement from sets of Bragg-edge strain images. In the case where these displacements are strictly the result of externally applied tractions, corresponding internal strain fields can then be found through traditional linear-static finite element methods. This approach is tested on synthetic data in two-dimensions, where the rate of convergence in the presence of measurement noise and beam attenuation is examined.

© 2016 Published by Elsevier B.V.

### 1. Bragg-edge strain measurement and the Longitudinal Ray Transform (LRT)

Bragg-edges are a term given to discrete jumps in the relative transmission rate of neutrons through polycrystalline samples as a function of wavelength,  $\lambda$  [1]. These edges are formed through diffraction with their positions related to lattice spacings within the sample through Bragg's law. In simple terms, in a polycrystalline sample neutrons can be coherently scattered by crystal planes of a certain spacing up until their wavelength corresponds to a scattering angle of 180° (i.e. backscattered). This wavelength is given by two times the corresponding lattice 'd-spacing', and no further (coherent) scattering by this lattice plane occurs above this value. This creates an abrupt increase in the relative transmission rate.

Multiple Bragg-edges can be found from a typical sample corresponding to various lattice spacings within the crystal structure. This can provide a wealth of structural information, or in the case of this paper, minute shifts in the position of edges can be used to measure strain within the sample of the form;

$$\langle \epsilon \rangle = \frac{d - d_0}{d_0}, \quad (1)$$

where  $\langle \epsilon \rangle$  is the normal stain in the direction of transmission averaged over the irradiated volume,  $d$  is the measured lattice spacing and  $d_0$  is the same spacing in an unstressed sample. Like all diffraction techniques, strain measured in this way refers only to the elastic portion of deformation which is related to stress through Hooke's law (see [2–5]).

While other approaches exist (e.g. [6]), the most common experimental technique for measuring Bragg-edges relies on the use of energy-resolved, or 'time-of-flight', neutron detectors at pulsed neutron sources [1,3]. This technology has undergone significant development with pixelated detectors being in existence for more than 10 years [7]. The current generation of detectors consist of an array of up to  $512 \times 512$  pixels with spatial resolution of 55 μm and temporal resolution of 100 ps<sup>1</sup>; each one capable of simultaneously measuring a transmission spectra [8]. This has allowed the possibility of high resolution strain imaging, where two dimensional projections of the strain field within a sample can be made in an analogous way to a traditional radiograph [9].

From the outset, the first demonstration of strain imaging raised the tantalising prospect of tomographic reconstruction of three-dimensional strain fields. As opposed to conventional tomographic imaging of scalar fields (e.g. X-ray CT and MRI), the problem here is the reconstruction of tensor fields – a significantly

\* Corresponding author.

E-mail address: [christopher.wensrich@newcastle.edu.au](mailto:christopher.wensrich@newcastle.edu.au) (C.M. Wensrich).

<sup>1</sup> The corresponding energy/wavelength resolution depends on the length of the instrument. For example, with a flight tube 40 m in length, 100 ps corresponds to a wavelength resolution of around 10<sup>-8</sup> Å.

more complex problem. Initial work in this area focused on the special case of axisymmetric systems (e.g. [10–12]), however it was recently shown by Lionheart and Withers [13] that a general solution to the reconstruction problem is not possible. An overview of this argument is as follows:

Say we have a body,  $B$ , subject to a displacement field  $\phi(\mathbf{x})$  as shown in Fig. 1. In the absence of attenuation effects and assuming a ray of infinitesimal cross section, a single strain measurement from a given pixel in an energy-resolved detector can be expressed as;

$$\langle \epsilon \rangle = I_\epsilon(\mathbf{x}_0, \hat{\mathbf{n}}) = \frac{1}{L} \int_0^L \epsilon_{ij}(\mathbf{x}_0 + s\hat{\mathbf{n}})\hat{n}_i \hat{n}_j ds, \quad (2)$$

where the corresponding ray in the direction  $\hat{\mathbf{n}}$  enters  $B$  at the point  $\mathbf{x}_0 \in \partial B$  and exits at  $\mathbf{x}_0 + L\hat{\mathbf{n}} \in \partial B$ , with internal strain defined as  $\epsilon_{ij} = \frac{1}{2}(\phi_{ij} + \phi_{ji})$ .<sup>2</sup>  $I_\epsilon$  is a form of ray transform, specifically known as the Longitudinal Ray Transform (LRT) [13].

Along the ray, we can write  $\frac{d\phi_i}{ds} = \phi_{ij} \frac{dx_j}{ds} = \phi_{ij} n_j$ , and (2) becomes;

$$I_\epsilon(\mathbf{x}_0, \hat{\mathbf{n}}) = \frac{1}{L} \int_0^L \frac{1}{2} (d\phi_i \hat{n}_i + d\phi_j \hat{n}_j) = \frac{1}{L} (\phi_i(\mathbf{x}_0 + L\hat{\mathbf{n}}) - \phi_i(\mathbf{x}_0)) \hat{n}_i \quad (3)$$

This result indicates that  $I_\epsilon$  is only sensitive to displacement of the boundary of  $B$ . Given that multiple strain fields exist that result in no boundary deformation, it implies that the LRT has a non-trivial kernel and therefore has no inverse. For a simple example; consider the case of a uniform two-dimensional plate that is fully constrained at its perimeter. Under the action of a body force such as gravity, the strain field within this plate would be non-zero; however, in terms of the LRT, this would be indistinguishable from the undeformed case ( $I_\epsilon = 0$  in both cases).

As was pointed out by Lionheart and Withers [13], this presents a serious problem in terms of general tomographic reconstruction of strain; a given boundary deformation does not uniquely define the strain field within an object.

## 2. Tomography via boundary displacement reconstruction

While the argument from Lionheart and Withers is true in a general sense, there are often physical realities that do lead to a trivial kernel. For example, if a uniform elastic body is only subject to boundary tractions (i.e. an *in situ* loading in the absence of all body forces and eigenstrains [14]), then there is an obvious (injective) link between the internal strain field and boundary deformation; an absence of boundary deformation obviously implies zero strain in this case.

This observation provides a potential approach to tomographic reconstruction of strain for this class of problems. This strategy is as follows;

1. Utilising Eq. (3), reconstruct the elastic component of displacement over the entire boundary of the object.
2. Calculate the internal strain field by solving the resulting Dirichlet boundary value problem.

A numerical implementation of this approach (adapted from [15]) is as follows;

### 2.1. Numerical algorithm

In the first stage, we are concerned with the reconstruction of boundary deformation. To this end, we begin by discretising the

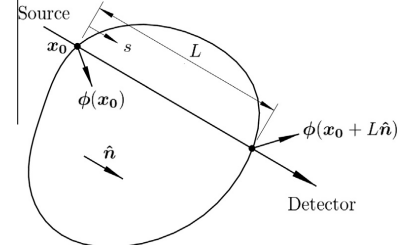


**Fig. 1.** Strain within a body measured by an idealised ray in a Bragg-edge time-of-flight transmission neutron experiment. This measurement represents the normal component of strain in the direction  $\hat{\mathbf{n}}$ , averaged along the path. It can be expressed as the relative change of the length of the path through the body.

surface of the body using a triangular mesh with  $n_v$  vertices (or ‘nodes’) with  $3n_v$  unknown Cartesian displacements. A given ray can enter and leave the body at arbitrary points; the displacement of which can be related back to the nodes through interpolation via linear shape functions.

Say a ray intersects a given mesh element at  $\mathbf{x}$  as shown in Fig. 2. With reference to the displacement of the three corresponding nodes,  $\phi_1$ ,  $\phi_2$ , and  $\phi_3$ , we can approximate the displacement at  $\mathbf{x}$  using linear shape functions as;

$$\phi(\mathbf{x}) = \lambda_1 \phi_1 + \lambda_2 \phi_2 + \lambda_3 \phi_3, \quad (4)$$

where  $\lambda_i = \frac{A_i}{A}$  for  $i \in \{1, 2, 3\}$  and  $A = \sum A_i$  is the total area of the element.

Through Eq. (3), we can now express the strain measured by a given Bragg-edge measurement in matrix form as;

$$\begin{aligned} \langle \epsilon \rangle &= I_\epsilon(\mathbf{x}^p, \hat{\mathbf{n}}) = \frac{1}{L} \begin{bmatrix} \hat{\mathbf{n}}^T & -\hat{\mathbf{n}}^T \end{bmatrix} \begin{bmatrix} \phi^q \\ \phi^p \end{bmatrix} \\ &= \frac{1}{L} \left( \begin{bmatrix} \hat{\mathbf{n}}^T \lambda_1^q & \hat{\mathbf{n}}^T \lambda_2^q & \hat{\mathbf{n}}^T \lambda_3^q \end{bmatrix} \begin{bmatrix} \phi_1^q \\ \phi_2^q \\ \phi_3^q \end{bmatrix} - \begin{bmatrix} \hat{\mathbf{n}}^T \lambda_1^p & \hat{\mathbf{n}}^T \lambda_2^p & \hat{\mathbf{n}}^T \lambda_3^p \end{bmatrix} \begin{bmatrix} \phi_1^p \\ \phi_2^p \\ \phi_3^p \end{bmatrix} \right), \end{aligned} \quad (5)$$

where superscript  $p$  refers to the entry point,  $q$  refers to the exit and  $L = \|\mathbf{x}^q - \mathbf{x}^p\|$ .

Note that this calculation has been split into two parts corresponding to the entry and exit. In principle these could be combined into one matrix, however if the mesh elements are neighbours it is possible for some of the vertices to be repeated. It should also be noted that this expression is constructed for a convex body, however it could be trivially extended to a non-convex body by considering differences between each instance of an entry or exit of the ray.

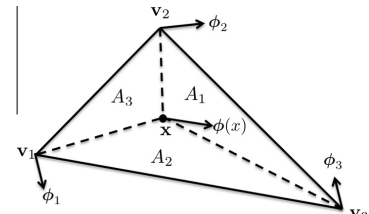


**Fig. 2.** Interpolation of displacement at a point  $\mathbf{x}$  within a triangular mesh element on the surface of a body. The areas of the sub triangles are denoted by  $A_1$ ,  $A_2$ , and  $A_3$ . The nodal displacements are given by  $\phi_1$ ,  $\phi_2$ , and  $\phi_3$ . The displacement at the point  $\mathbf{x}$  is  $\phi(\mathbf{x})$ .

Given  $m$  such rays, we can build a matrix relating the displacement of all nodes to the set of strain measurements of the form;

$$\begin{bmatrix} \vdots \\ \epsilon_k \\ \vdots \end{bmatrix} = \begin{bmatrix} \vdots & & & & & \\ \cdots & \frac{1}{l_k} \hat{\mathbf{n}}_k^T \lambda_1^q & \cdots & \frac{1}{l_k} \hat{\mathbf{n}}_k^T \lambda_2^q & \cdots & \frac{1}{l_k} \hat{\mathbf{n}}_k^T \lambda_3^q \cdots & \vdots \\ \vdots & \vdots & \vdots & \vdots & \vdots & \vdots & \vdots \\ - & \begin{bmatrix} \vdots & & & & & \\ \cdots & \frac{1}{l_k} \hat{\mathbf{n}}_k^T \lambda_1^p & \cdots & \frac{1}{l_k} \hat{\mathbf{n}}_k^T \lambda_2^p & \cdots & \frac{1}{l_k} \hat{\mathbf{n}}_k^T \lambda_3^p \cdots & \vdots \\ \vdots & \vdots & \vdots & \vdots & \vdots & \vdots & \vdots \end{bmatrix} & \begin{bmatrix} \vdots \\ \phi_1^q \\ \vdots \\ \phi_2^q \\ \vdots \\ \phi_3^q \\ \vdots \end{bmatrix} \\ - & \begin{bmatrix} \vdots & & & & & \\ \cdots & \frac{1}{l_k} \hat{\mathbf{n}}_k^T \lambda_1^p & \cdots & \frac{1}{l_k} \hat{\mathbf{n}}_k^T \lambda_2^p & \cdots & \frac{1}{l_k} \hat{\mathbf{n}}_k^T \lambda_3^p \cdots & \vdots \\ \vdots & \vdots & \vdots & \vdots & \vdots & \vdots & \vdots \end{bmatrix} & \begin{bmatrix} \vdots \\ \phi_1^p \\ \vdots \\ \phi_2^p \\ \vdots \\ \phi_3^p \\ \vdots \end{bmatrix}, \quad (6) \end{bmatrix}$$

where elements associated with measurement  $k$  are inserted into the  $k$ th row and into the columns associated with the corresponding entry and exit nodes. This process produces a measurement matrix,  $\mathbf{A}$ , with  $m$  rows and  $3n_v$  columns of the form;

$$\epsilon^* = \mathbf{A}\Phi, \quad (7)$$

where  $\epsilon^*$  are the expected measurements corresponding to a given set of deformations,  $\Phi$ .

We can then determine the boundary deformations that correspond to a given set of measurements,  $\epsilon_m$ , by solving the associated unconstrained least squares optimisation problem;

$$\Phi^* = \underset{\Phi \in \mathbb{R}^{3n_v}}{\operatorname{argmin}} \|\epsilon_m - \mathbf{A}\Phi\|^2. \quad (8)$$

Several algorithms exist for solving such a problem, however it should be noted that the matrix  $\mathbf{A}$  is very sparse (at most, each ray interacts with only 6 nodes). The LSQR algorithm [16] exploits this sparsity and is ideally suited to the problem.

The second stage involves the calculation of the internal elastic strain field from the reconstructed boundary displacements. This can proceed by solving the resulting Dirichlet boundary problem using well established linear-static Finite Element techniques.

## 2.2. Necessary conditions and uniqueness

There are two necessary but not sufficient conditions required to accurately solve this problem. Firstly, the measurements need to be taken from at least 3 distinct directions when solving in two-dimensions, or 6 directions when solving in three-dimensions. This relates directly to the number of unique elements in the strain tensor at each point.

The second condition requires that  $\mathbf{A}$  has sufficient rank to solve for the  $3n_v$  deformations. This can approximately determine the required number of projections; however there are two complicating factors;

1. In any given projection, some pixels may contribute no extra information. For example, the corresponding ray may not pass through any material.
2. The measurement has an invariance to translation and rotation which limits the rank of  $\mathbf{A}$  to  $3n_v - 6$ .

This second issue implies that a family of equivalent solutions exist which differ by rigid body motions. In principle, any one of these solutions could be used to determine the strain field within the body through the process indicated above; however, strictly speaking they are unbounded<sup>3</sup>. A range of techniques exist for finding individual solutions within this set, with either a subset of unknown displacements set to zero (known as *basic solutions*) [17] or minimum  $L_2$  norm solutions through regularisation of the form;

$$\Phi^* = \underset{\Phi \in \mathbb{R}^{3n_v}}{\operatorname{argmin}} (\|\epsilon_m - \mathbf{A}\Phi\|^2 + \zeta \|\Phi\|^2) = \underset{\Phi \in \mathbb{R}^{3n_v}}{\operatorname{argmin}} \left\| \begin{bmatrix} \epsilon_m \\ \mathbf{0}_{[m \times 1]} \end{bmatrix} - \begin{bmatrix} \mathbf{A} \\ \zeta \mathbf{I}_{[m \times m]} \end{bmatrix} \Phi \right\|^2 \quad (9)$$

with a suitably small parameter  $\zeta > 0$ . Note that the intrinsic LSQR algorithm implemented in the MATLAB numerical analysis package automatically selects the minimum  $L_2$  norm solution in rank deficient cases such as this.

## 3. Simulation

In the following section we provide an overview of an implementation of this algorithm that is tested on synthetic data. Appropriate experimental data is not yet available, however this situation will hopefully be remedied soon with experiments planned in the near future.

The algorithm we have outlined has been explicitly developed for the three-dimensional case, however, in this simple demonstration, we revert back to two-dimensions where interpolation of strain fields and visualisation of solutions are simplified. At all times it should be noted that a three-dimensional implementation would follow along similar lines, but carry slightly more complexity in terms of geometry and the size of the problem.

Consider the two-dimensional (plane stress) uniform isotropic cantilevered plate subject to a load,  $P$ , as shown in Fig. 3a.

The strain field within this plate can be approximated as;

$$\begin{aligned} \epsilon_{xx} &= \frac{P}{EI}(l-x)y, \quad \epsilon_{yy} = \epsilon_{zz} = -\frac{vP}{EI}(l-x)y, \\ \epsilon_{xy} &= -\frac{(1+v)P}{2EI}(h^2 - y^2), \quad \epsilon_{xz} = \epsilon_{yz} = 0, \end{aligned} \quad (10)$$

where  $E$  and  $v$  are Young's modulus and Poisson's ratio respectively and  $I = \frac{bh^3}{12}$ . The restraint caused by the fixed end and the presence of the load create local deviations from this idealised distribution; a finite element solution to the actual strain field accounting for these factors is shown in Fig. 3b.

As a demonstration and test-bed for our reconstruction algorithm, it is possible to make simulated Bragg-edge strain projections of this strain distribution based on Eq. (2). Reconstruction of the two-dimensional strain field from this synthetic data allows the convergence of the algorithm to be examined in addition to its ability to reject experimental noise and other systematic errors.

In all of the following analysis,  $E = 200$  GPa,  $v = 0.3$ ,  $h = 10$  mm,  $t = 6$  mm,  $l = 20$  mm, and  $P = 2$  kN.

### 3.1. Synthetic data generation

The strain field shown in Fig. 3b is based on a linear-static solve in the structural finite element package STRAND7. This model involves a  $40 \times 20$  mesh of quad4 plate elements.

Components of the biaxial strain tensor at the centroid of each element in this mesh were imported into MATLAB through the STRAND7 Advanced Programming Interface (API). Simulated

<sup>3</sup> if  $\Phi$  is a solution, then  $\Phi + \Phi^0$  where  $\Phi^0 \in \text{null}(\mathbf{A})$  is also a solution.

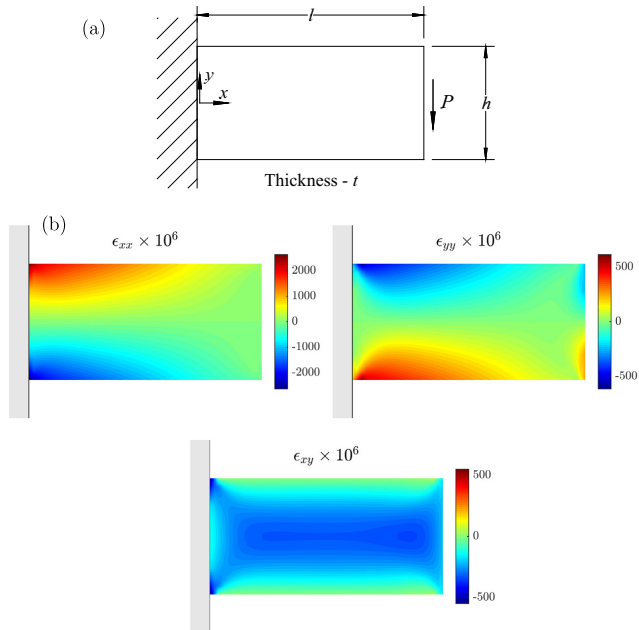


**Fig. 3.** (a) A uniform two-dimensional isotropic plate subject to a cantilevered load of  $P$ . (b) A finite element solution to the strain field for  $E = 200$  GPa,  $v = 0.3$ ,  $h = 10$  mm,  $t = 6$  mm,  $l = 20$  mm, and  $P = 2$  kN. (For interpretation of the references to color in this figure legend, the reader is referred to the web version of this article.)

projections were made by applying Eq. (2) to this field assuming a one-dimensional pixelated detector with a pixel spacing of 55  $\mu\text{m}$ .

Integration along ray paths was based on a nearest-neighbour linear interpolation of the strain field using the ‘scatteredInterpolant’ intrinsic MATLAB function and the trapezoid rule. In principle, simulated measurements could have been based on Eq. (3), however a more pragmatic approach allows for easier simulation of experimental realities such as attenuation and finite beam width.

### 3.2. Convergence and noise rejection

Reconstruction of boundary deformation from various sets of simulated projections were carried out in MATLAB using the LSQR intrinsic function to solve Eq. (8). In each case, the set of projections were made over an array of equally spaced angles over  $180^\circ$  to avoid repeated measurements; projections in opposing directions are equivalent. Measurement uncertainty was introduced by adding various levels of zero-mean Gaussian noise to each simulated strain measurement.

Reconstructions were based on 121 boundary nodes in-line with those used in the finite element model (i.e. 242 unknown displacements). Displacements due to rigid body motions were removed from each reconstruction through an optimisation process. This involved the determination of a translation and rotation that, when combined, minimises the displacement of the restrained nodes at the fixed support. Corresponding strain fields were then calculated by applying the adjusted displacements to the boundary of an otherwise unrestrained finite element model using the STRAND7 API.

**Fig. 4** shows typical results in terms of the reconstructed strain field for 5 and 30 projections with a measurement uncertainty<sup>4</sup> of  $1 \times 10^{-4}$ .

In all cases, the observed error in the reconstructed strain profile reduced as the number of projections increased. In terms of standard deviation, this error was limited by a lower bound of  $2 \times 10^{-5}$  which, after thorough investigation, was found to be related to differences between the interpolation method between STRAND and MATLAB; quad4 shape functions in STRAND verses natural-neighbour linear interpolation in MATLAB.

**Fig. 5** shows the reduction of the uncertainty in the reconstructed strain field as a function of the number of projections over a range of uncertainties. The value reported is the amount in excess of the lower bound. As was previously observed in granular systems [15], the rate of convergence to the solution was found to be of the order  $\sim (N - 3)^{0.5}$  (see inset in **Fig. 5**).

### 3.3. Effects of attenuation

The measurement model described by Eq. (2) is idealised in the sense that it assumes no attenuation of the neutron beam. In reality, the intensity of the beam diminishes as it passes through the body, and this introduces a non-uniform weighting to the average strain measured by Bragg-edges. If we assume a uniform linear attenuation coefficient,<sup>5</sup>  $\mu$ , this weighting is described by an

<sup>4</sup> This value represents the standard deviation in each Bragg-edge strain measurement.

<sup>5</sup> Attenuation is typically wavelength dependent. The coefficient used here should be a value representative for wavelengths close to the Bragg-edge under consideration.

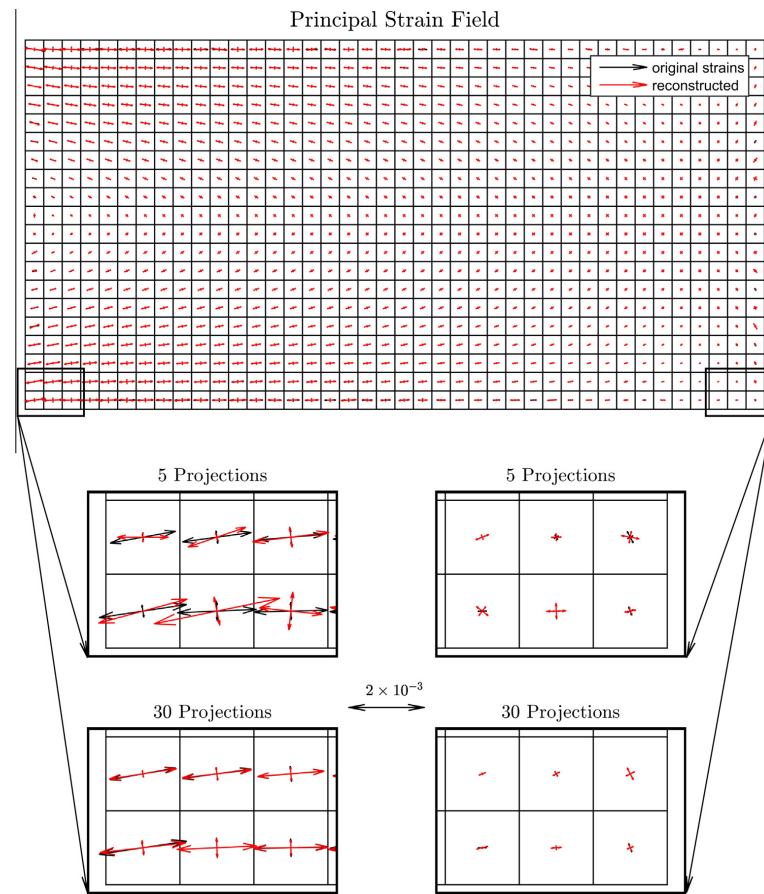


**Fig. 4.** Reconstructed distributions of the principal strains within the cantilevered plate; original strain field in black, reconstructions in red. (For interpretation of the references to color in this figure legend, the reader is referred to the web version of this article.)

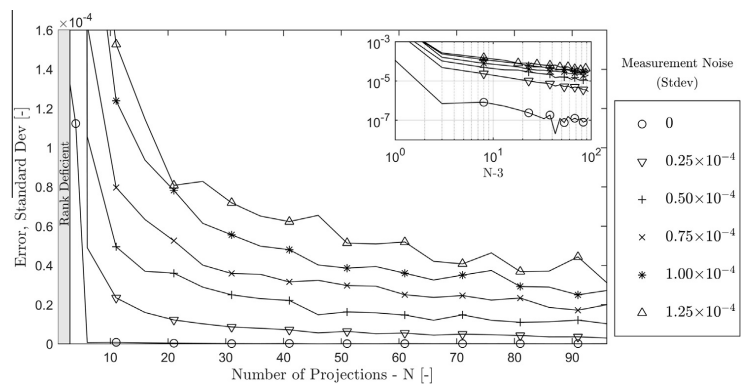


**Fig. 5.** Uncertainty in the reconstructed strain distribution as a function of the number of projections.

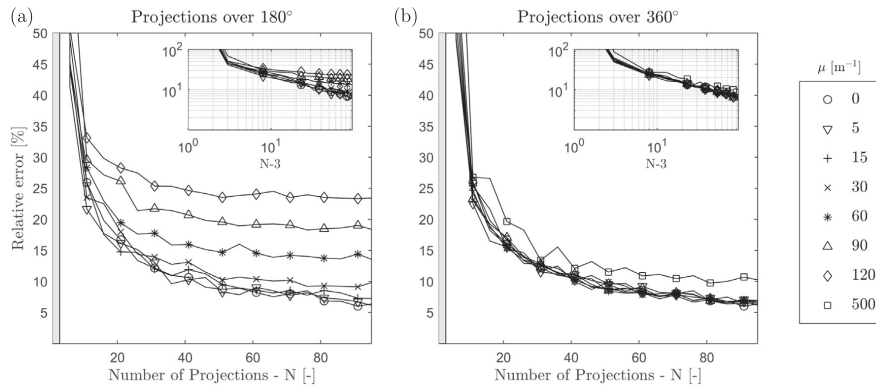


**Fig. 6.** Convergence of the reconstructed strain profile in the presence of beam attenuation and a measurement uncertainty of  $1 \times 10^{-4}$  for (a) sets of projections over a  $180^\circ$  arc and (b) projections over the full  $360^\circ$  range.

exponential decay of the form  $e^{-\mu s}$  and the weighted version of the LRT becomes;

$$I_{\mu e}(\mathbf{x}_0, \hat{\mathbf{n}}) = \frac{1}{\int_0^L e^{-\mu s} ds} \int_0^L e^{-\mu s} \epsilon_{ij}(\mathbf{x}_0 + s\hat{\mathbf{n}}) \hat{n}_i \hat{n}_j ds. \quad (11)$$

This weighting can easily be introduced into the simulation process to investigate the effects of attenuation on the reconstruction.

Sets of projections were generated with  $\mu = 5, 15, 30, 60$  and  $90 \text{ m}^{-1}$ , representing typical attenuation rates over a range of materials (e.g.  $\mu = 10 \text{ m}^{-1}$  for aluminium, and  $\mu = 120 \text{ m}^{-1}$  for iron [18]). Two different sets were created for each attenuation value; one where projections were made over  $180^\circ$  (as before), and one where directions alternated over the full  $360^\circ$  to minimise bias. Specifically, for a set of  $N$  projections; angles over  $180^\circ$  were chosen as  $\frac{\pi}{N}n$ , while corresponding angles over  $360^\circ$  were  $\frac{\pi}{N}n + \frac{\pi}{2}(1 - (-1)^n)$ , where  $n = 0, 1, \dots, N - 1$ .

In all cases, noise with a standard deviation of  $10^{-4}$  was included in the simulated measurements.

The relative magnitude of the error in the reconstruction<sup>6</sup> for each set is shown in Fig. 6.

With projections over  $180^\circ$ , attenuation created a systematic, spatially distributed error in the reconstructed strain profile which was observed to increase with attenuation rate. Below  $\mu = 30 \text{ m}^{-1}$  this effect was negligible. Note that  $\mu = 30 \text{ m}^{-1}$  corresponds to an attenuation half-length of 23 mm, which is comparable to the dimensions of the sample. It is expected that this error would also depend on the gradient of the strain field; if the strain field is constant, the exponential weighting has no effect.

This systematic error was negligible in the case where projections were made over  $360^\circ$ . It appeared as though the bias introduced by attenuation is largely mitigated by making projections from all direction and the algorithm was able to converge to the correct solution regardless of the attenuation rate. As a final test of this observation, a simulation for  $\mu = 500 \text{ m}^{-1}$  was carried out with the result shown in Fig. 6. Even at this extreme rate of attenuation, the deviation of the reconstructed distribution from the unattenuated case is reasonably small. Note that  $\mu = 500 \text{ m}^{-1}$  corresponds to a transmission rate as low as 0.002% for some ray paths through

the sample. This is an encouraging observation that tends to suggest that modification of the algorithm to account for the effects of attenuation is unnecessary with appropriate experiment design.

#### 4. Conclusions

Bragg-edge neutron strain tomography appears to be possible for *in situ* loadings in the absence of body forces and eigenstrains. A three-dimensional algorithm was developed through which this can be achieved through reconstruction of elastic boundary displacement followed by the calculation of a linear-static finite element solution to the resulting elasticity problem.

In a two-dimensional demonstration, this approach was found capable of reconstructing internal strain fields from Bragg-edge strain images in the presence of realistic levels of measurement noise and beam attenuation. In this system, the bias introduced by beam attenuation was able to be practically removed by ensuring projections were made over a full  $360^\circ$  range; at least up to the maximum attenuation rate examined. Experimental realities would provide many other obstacles at attenuation rates beyond those tested.

The next stage of this work will involve the planning and execution of an experimental demonstration of the technique. The simulation tool developed in this paper will provide invaluable guidance in this process. For example; in the two-dimensional example presented, with a measurement uncertainty of  $1 \times 10^{-4}$  and an attenuation rate similar to iron, around 40–50 projections are required to achieve a final uncertainty of  $5 \times 10^{-5}$  in a reconstructed strain distribution with 0.5 mm spatial resolution.

#### Acknowledgments

This work is supported by the Australian Research Council through a Discovery Project Grant (DP130104290).

#### References

- [1] J. Santisteban, L. Edwards, M. Fitzpatrick, A. Steuwer, P. Withers, Engineering applications of Bragg-edge neutron transmission, *Appl. Phys. A* 74 (1) (2002) s1433–s1436.
- [2] E.H. Kisi, C.J. Howard, *Applications of Neutron Powder Diffraction*, Oxford University Press, 2008.
- [3] M.E. Fitzpatrick, A. Lodini, *Analysis of Residual Stress by Diffraction Using Neutron and Synchrotron Radiation*, CRC Press, 2003.

<sup>6</sup> Overall relative error has been calculated as  $\sqrt{\frac{\sum \delta e_{ij}^n \delta e_{ij}^n}{\sum e_{ij}^{n,0} e_{ij}^{n,0}}}$ , where  $\delta e_{ij}^n$  is the difference between the original strain tensor,  $e_{ij}^n$ , and the reconstructed version at the centroid of mesh element  $n$ .



## **Appendix C**

# **General Tomographic Reconstruction Paper**

# Tomographic Reconstruction of Elastic Strain Fields from Attenuated Bragg-Edge Neutron Measurements

A.W.T Gregg<sup>a</sup>, J.N. Hendriks<sup>a</sup>, C.M. Wensrich<sup>a</sup>, M.H. Meylan<sup>b</sup>, A Wills<sup>a</sup>

<sup>a</sup>*School of Engineering, The University of Newcastle, Callaghan NSW 2308, Australia*

<sup>b</sup>*School of Mathematical and Physical Sciences, The University of Newcastle, Callaghan NSW 2308, Australia*

---

## Abstract

*Keywords:* Strain tomography; Bragg-edge neutron transmission

---

### 1. Neutron Transmission Strain Imaging and Tomography

2       Bragg-edges refer to abrupt increases in the relative neutron transmission  
3       rate in polycrystalline solids as a function of wavelength [1]. These edges  
4       are formed through diffraction; any given neutron of wavelength  $\lambda$  can be  
5       coherently scattered by crystal planes of a given spacing,  $d$ , provided that  
6       the scattering angle,  $\theta$ , satisfies Bragg's law;  $\lambda = 2d \sin \theta$ . This relationship  
7       holds up until  $\lambda = 2d$  and above this wavelength an abrupt increase in  
8       transmission rate occurs due to the fact that it is not possible to scatter a  
9       neutron by more than  $2\theta = 180^\circ$  (i.e. backscattered). Similar to diffraction  
10      peaks, the location and geometry of these edges can provide a great deal of  
11      information on the structure, phase composition and internal strain state of  
12      materials [1].

13       Of particular interest here, strain measurements based on the relative  
14      movement of Bragg-edges refer to the average forward (or backward) com-  
15      ponent of normal strain through a sample in the direction of transmitted  
16      neutrons. As with all diffraction techniques, these measurements refer only  
17      to the elastic component of strain.

18       Modern time-of-flight detector technology now provides the ability to  
19      make high-resolution Bragg-edge strain measurements in much the same way  
20      as a traditional radiograph [2]. Strain imaging obviously raises the prospect  
21      of strain tomography, and several attempts have been made to solve the  
22      resulting tensor reconstruction problem over the past decade. These attempts

have revolved around a number of special cases such as axial-symmetry [3, 4, 5], granular systems [6] and reconstruction in the absence of eigenstrains [7].

The key approach in the initial work on axisymmetric systems revolved around expressing the tensor reconstruction problem as a scalar problem through an assumption of strain compatibility. This stemmed from a belief that it is not possible to reconstruct more than one variable per pixel using single axis tomography. This is certainly the case for scalar reconstruction problems, but is not strictly true here. The measurement projects different linear combinations of the unknown strain components depending on the direction. For example; in the simplest two-dimensional case, three unknown strain components for a system consisting of one pixel can be resolved by making three independent measurements from different directions.

In spite of the assumption of compatibility, these axisymmetric approaches have successfully reconstructed a number of inherently incompatible strain fields (e.g. ring-and-plug systems). While general application is far from demonstrated, this is none-the-less a puzzling result.

## 2. The Longitudinal Ray Transform (LRT) and its null space

The measurement at each pixel within a transmission strain image can be modeled as being a Longitudinal Ray Transform (LRT) of the strain field. With reference to Figure 1, this can be written [8];

$$I_\epsilon(\mathbf{x}_0, \hat{\mathbf{n}}) = \frac{1}{L_0} \int_0^{L_0} \epsilon_{ij}(\mathbf{x}_0 + s\hat{\mathbf{n}}) \hat{n}_i \hat{n}_j ds \quad (1)$$

As was recently pointed out by Lionheart and Withers [8], in the case of compatible strain fields, the LRT is only dependent on boundary displacement. This can be observed by considering a body subject to a displacement field  $\phi$ , resulting in the strain field;  $\epsilon_{ij} = \frac{1}{2}(\phi_{i,j} + \phi_{j,i})$ . Along the ray we can write  $\frac{d\phi_i}{ds} = \phi_{i,j} \frac{dx_j}{ds} = \phi_{i,j} n_j$ , and Equation (1) becomes;

$$I_\epsilon(\mathbf{x}_0, \hat{\mathbf{n}}) = \frac{1}{L_0} \int_0^{L_0} \frac{1}{2} \left( \frac{d\phi_i}{ds} \hat{n}_i + \frac{d\phi_j}{ds} \hat{n}_j \right) ds = \frac{1}{L_0} (\phi_i(\mathbf{x}_1) - \phi_i(\mathbf{x}_0)) \hat{n}_i \quad (2)$$

In simple terms, this implies that  $I_\epsilon$  can be expressed as the relative change in the path-length  $L_0$ . This highlights a sizable null space that consists of, at least, the set of all compatible strain fields that result in no

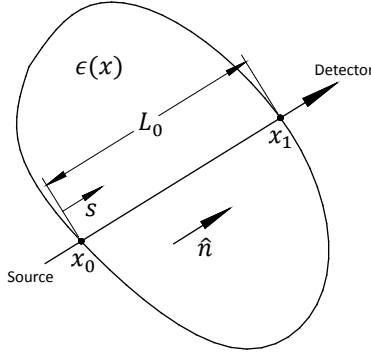


Figure 1: A single Bragg-edge measurement from a ray passing through a sample provides the average normal strain in the forward direction.

52 boundary deformation. This directly implies that no unique inverse exists,  
 53 and the general reconstruction problem is not solvable without additional  
 54 information.

55 This certainly presents a difficulty, however it does not prevent a solution  
 56 being found if additional physical constraints can be found (e.g. equilib-  
 57 rium equations or the minimisation of strain energy). A special case of this  
 58 was considered by Wensrich et al. where it was assumed that the unknown  
 59 strain field was only the result of boundary tractions [7]. In this case, the  
 60 reconstruction algorithm can focus on determining the resulting boundary  
 61 deformation and the strain field can be found as a Finite Element solution  
 62 to the resulting linear-elastic boundary value problem.

63 The LRT has an inherent symmetry of the form;  $I_\epsilon(\mathbf{x}_0, \hat{\mathbf{n}}) = I_\epsilon(\mathbf{x}_1, -\hat{\mathbf{n}})$ ,  
 64 which, in practice, is broken through the effects of attenuation.

$$I_{\mu\epsilon}(\mathbf{x}_0, \hat{\mathbf{n}}) = \frac{1}{\int_0^{L_0} e^{-\mu s} ds} \int_0^{L_0} e^{-\mu s} \epsilon_{ij}(\mathbf{x}_0 + s\hat{\mathbf{n}}) \hat{n}_i \hat{n}_j ds. \quad (3)$$

65 Through a similar process to before, for the strain field  $\epsilon_{ij} = \frac{1}{2}(\phi_{i,j} + \phi_{j,i})$ ,

66 integration by parts provides;

$$I_{\mu\epsilon}(\mathbf{x}_0, \hat{\mathbf{n}}) = \frac{\mu}{1 - e^{-\mu L_0}} \left[ (e^{-\mu L_0} \phi_i(\mathbf{x}_1) - \phi_i(\mathbf{x}_0)) \hat{n}_i + \mu \int_0^{L_0} e^{-\mu s} \phi_i \hat{n}_i ds \right] \quad (4)$$

67 The two stages in this approach are essentially decoupled; boundary deformation  
68 is found that best fits the strain measurements, and then the physics  
69 of the problem is introduced through the finite element model.

70 In a more general system this approach is not possible due to the fact  
71 that the relationship in Equation 2 is based directly on an assumption of  
72 the compatibility of the strain field. In the presence of eigenstrains, the  
73 elastic component of strain (i.e. observed strain) does not necessarily have  
74 this constraint and there is no direct link between boundary deformation  
75 and the measurements. None-the-less, the general approach may still have  
76 some merit; a solution is to be found that best fits the measurements while  
77 simultaneously minimising strain energy

78 It may also be possible to base the reconstruction on a less idealised model  
79 of strain measurement; one that hopefully has a trivial null space.

### 80 3. Components of Strain

81 In a general sense, the strain at any point in a body can be decomposed  
82 into three parts;

$$\epsilon = \epsilon_E + \epsilon_T + \epsilon_P. \quad (5)$$

83 Where  $\epsilon_E$  is the elastic component of strain, that is related to stress  
84 through Hooke's law.  $\epsilon_T$  is the strain due to thermal expansion and  $\epsilon_P$  all  
85 forms of so-called *Eigen-strain* (such as plastic strain and interference).

86 Note that we have intentionally excluded thermal expansion from our  
87 definition of Eigen-strain. The principal reason for this is that, as with all  
88 diffraction techniques, Bragg-edge strain measurements only observe strains  
89 that physically alter lattice spacing. As a general rule, Eigen-strains (as  
90 identified here) do not fall into this category.

92 This has an important consequence in terms of the compatibility of the  
93 strain field observed by Bragg-edge imaging. Notionally, compatibility guarantees  
94 the strain field is related to the gradient of an underlying single-valued

96 displacement field; however, it refers to the total strain - not the individual  
97 parts. From this point of view, it is quite possible that the observed strain  
98 field (that is,  $\epsilon_E + \epsilon_T$  violates compatibility if Eigen-strains are present.

99  
100 This potential incompatability is at the heart of why the boundary re-  
101 construction method detailed in (Wensrich, 2016) cannot be utilised in the  
102 presence of Eigen-strains. However, a new method of reconstruction, dubbed  
103 the *Internal-Strain Method* shows promise in reconstructing the visible strain  
104 field  $\epsilon_E + \epsilon_T$  even in the presence of Eigen-strains.

#### 105 4. The Internal Strain Method

106 The average strain seen by an attenuated Bragg-Edge measurement  $k$  can  
107 be idealised as:

$$\langle \epsilon_k \rangle = \frac{1}{\int_0^L \chi(s) ds} \int_0^L \chi(s) \hat{\mathbf{n}}^\top \boldsymbol{\epsilon}(\mathbf{x}_0 + s\hat{\mathbf{n}}) \hat{\mathbf{n}} ds. \quad (6)$$

108 Where  $\chi(s) = e^{-\mu s}$ . In an approach reminiscent of finite-element analysis,  
109 we discretise the elastic strain field that is to be reconstructed into a collection  
110 of  $N$  distinct voxels. We define the set of all voxel indices as  $V$ . Each voxel  
111  $v \in V = 1, 2, \dots, \max(V)$  is assumed to posses a constant, unknown strain  
112 tensor  $\boldsymbol{\epsilon}_v$ .

113 Define the set of indices corresponding to voxels intersected by a ray  $k$   
114 as  $M_k \in V$ , and allow  $m_k$  to index each element of  $M_k$ . For example, say a  
115 body contains six voxels,  $V = \{1, 2, 3, 4, 5, 6\}$  as shown in figure 2.

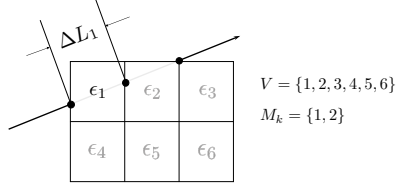


Figure 2: Two voxels are intersected by a ray.

116 Then  $M_k = \{1, 2\}$  and  $m_k = 1$  then  $m_k = 2$ .

<sup>117</sup> The measurement  $\langle \epsilon_k \rangle$  can be modelled by an Euler approximation to the  
<sup>118</sup> integral which takes the form:

$$\langle \epsilon_k \rangle \approx \frac{\chi(L_k)}{\sum_{m \in M_k} \chi(s_m) \Delta L_m} \sum_{m \in M} \chi(s_m) \hat{\mathbf{n}}_k^\top \boldsymbol{\epsilon}_m \hat{\mathbf{n}}_k \Delta L_m \quad (7)$$

<sup>119</sup> Where  $\Delta L_m$  is the illuminated length of a voxel with index  $m$  penetrated  
<sup>120</sup> by the ray,  $s_m$  is the value of the co-ordinate  $s$  at the midpoint of the illu-  
<sup>121</sup> minated length of voxel  $m$ ,  $\boldsymbol{\epsilon}_m$  is the unknown strain tensor in voxel  $m$ , and  
<sup>122</sup>  $\hat{\mathbf{n}}_k$  is the unit direction vector of ray  $k$ .

<sup>123</sup> Define a vector  $\boldsymbol{\varepsilon}_v$  that contains the (three) unique unknown strain com-  
<sup>124</sup> ponents in a voxel  $v$  by:

$$\boldsymbol{\varepsilon}_v = \begin{bmatrix} \boldsymbol{\epsilon}_{xx_v} \\ \boldsymbol{\epsilon}_{xy_v} \\ \boldsymbol{\epsilon}_{yy_v} \end{bmatrix} \quad (8)$$

<sup>125</sup> And a vector  $\mathbf{N}_k$  such that:

$$\hat{\mathbf{n}}_k^\top \boldsymbol{\epsilon}_v \hat{\mathbf{n}}_k = \mathbf{N}_k \boldsymbol{\varepsilon}_v \quad (9)$$

<sup>126</sup> Also define the scaling co-efficient due to attenuation of each ray  $k$  as:

$$C_k = \frac{\chi(L_k)}{\sum_{m \in M_k} \chi(s_m) \Delta L_m} \quad (10)$$

<sup>127</sup> If many measurements of this form are taken, a system of linear equations  
<sup>128</sup> can be constructed relating the strain measurements  $\langle \epsilon \rangle$  to the unknown  
<sup>129</sup> intersected voxel strain tensor components  $\boldsymbol{\varepsilon}_v$

$$\begin{bmatrix} \vdots \\ \langle \epsilon_k \rangle \\ \vdots \end{bmatrix} = \begin{bmatrix} & & & & & \\ & \cdots & C_k N_k \chi(s_1) \Delta L_1 & \cdots & C_k N_k \chi(s_{\max(M_k)}) \Delta L_{\max(M_k)} & \cdots \\ & & \vdots & & \vdots & \\ & & & & & \end{bmatrix} \begin{bmatrix} \vdots \\ \boldsymbol{\varepsilon}_1 \\ \vdots \\ \boldsymbol{\varepsilon}_{\max(M_k)} \\ \vdots \end{bmatrix} \quad (11)$$

<sup>130</sup>      The resulting system co-efficient matrix is by nature very sparse, with  
<sup>131</sup> only a small subset of all voxels usually intersected by a given ray.

<sup>132</sup>      At no stage in this formulation have we specified that the body under  
<sup>133</sup> examination must not contain so-called Eigen-strains.

<sup>134</sup>      This concept can be extended to more accurate approximations of the  
<sup>135</sup> integral (i.e: trapezoidal) in the construction of the co-efficient matrix.

<sup>137</sup> **5. Demonstration and Simulation**

<sup>138</sup> In order to test our hypothesis that the presence of attenuation trivialises transform kernel, a simulation environment which implements the Internal Strain Method has been developed. Bragg-Edge strain tomography  
<sup>139</sup> has been simulated for two cases: a cantilevered beam, and an artificial,  
<sup>140</sup> non-compatible strain field.  
<sup>141</sup>

<sup>143</sup> *5.1. Simulation of Bragg-Edge Measurements*

<sup>144</sup> In 2D examples, the cartesian components of a strain tensor field can  
<sup>145</sup> be characterised by three scalar fields: an  $\epsilon_{xx}(x, y)$ ,  $\epsilon_{xy}(x, y)$  and  $\epsilon_{yy}(x, y)$   
<sup>146</sup> field. In both reconstructions, these have been characterised by MATLAB  
<sup>147</sup> anonymous functions which allow the components of the biaxial strain tensor  
<sup>148</sup> to be queried at all  $(x, y)$  points within the plate.

<sup>149</sup> Attenuated Bragg-Edge measurements were simulated by applying Equation  
<sup>150</sup> XXX to this tensor field. In both cases, a one-dimensional pixelated  
<sup>151</sup> detector with characteristic length 30mm and pixel width of  $55\mu\text{m}$  has been  
<sup>152</sup> simulated. Integration along ray paths was performed using trapezoid rule,  
<sup>153</sup> namely via the intrinsic `trapz` MATLAB function.

<sup>154</sup> *5.2. Reconstruction: Cantilevered Beam*

<sup>155</sup> Problem geometry, loading and material properties for this reconstruction  
<sup>156</sup> were chosen to replicate the conditions simulated in [7], and are as shown in  
<sup>157</sup> Figure 3a.

<sup>158</sup> The strain field within this beam has been approximated as;

$$\begin{aligned}\epsilon_{xx} &= \frac{P}{EI}(l - x)y, \quad \epsilon_{yy} = \epsilon_{zz} = -\frac{\nu P}{EI}(l - x)y, \\ \epsilon_{xy} &= -\frac{(1 + \nu)P}{2EI} \left( \left(\frac{h}{2}\right)^2 - y^2 \right), \quad \epsilon_{xz} = \epsilon_{yz} = 0,\end{aligned}\tag{12}$$

<sup>159</sup> where  $E$  and  $\nu$  are Young's modulus and Poisson's ratio respectively and  
<sup>160</sup>  $I = \frac{th^3}{12}$ . The  $\epsilon_{xx}$ ,  $\epsilon_{xy}$  and  $\epsilon_{yy}$  components of this field are shown in Figure 3b.  
<sup>161</sup> Note that minor differences exist between the field observed here and that in  
<sup>162</sup> [7], where instead a finite-element solution to the field was under study.

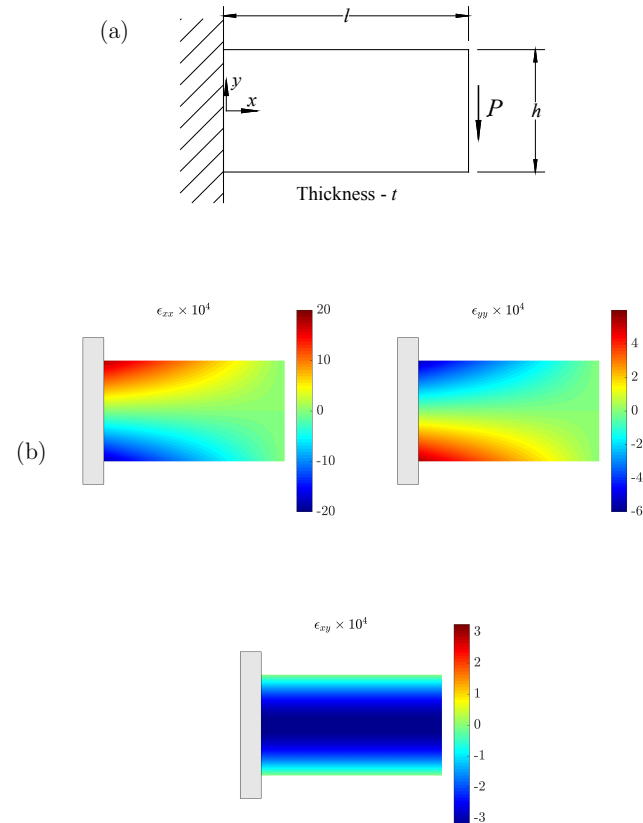


Figure 3: (Colour online)(a) A uniform two-dimensional isotropic plate subject to a canilevered load of  $P$ . (b) An analytical solution to the strain field for  $E = 200\text{GPa}$ ,  $\nu = 0.3$ ,  $h = 10\text{mm}$ ,  $t = 6\text{mm}$ ,  $l = 20\text{mm}$ , and  $P = 2\text{kN}$ .

163    5.2.1. *Simulation Results*

164    A sensitivity analysis revealed that the quality of a simulated reconstruction  
 165    was largely dependent on three variables: the number of measurement  
 166    projections taken, the density of the reconstruction mesh, and the magni-  
 167    tude of attenuation applied, characterised by the attenuation co-efficient  $\mu$ .  
 168    A quantitative measure of relative reconstruction error was calculated as:

$$\sqrt{\frac{\sum_n \delta\epsilon_{ij}^n \delta\epsilon_{ij}^n}{\sum_n \epsilon_{ij}^n \epsilon_{ij}^n}}. \quad (13)$$

169    Where  $\delta\epsilon_{ij}^n$  is the difference between the true strain tensor,  $\epsilon_{ij}^n$  (itself  
 170    calculated as an integral average of the strain field over the voxel area), and  
 171    the reconstructed version at voxel in question  $n$ . A plot of this reconstruction  
 172    error as a function of the number of measurement projections taken and the  
 173    attenuation magnitude is shown in figure 4. Here, a mesh discretisation of  
 174     $40 \times 80$  square voxels (of characteristic length 0.25 mm) was implemented,  
 175    which was found to be sufficient to achieve mesh independence.

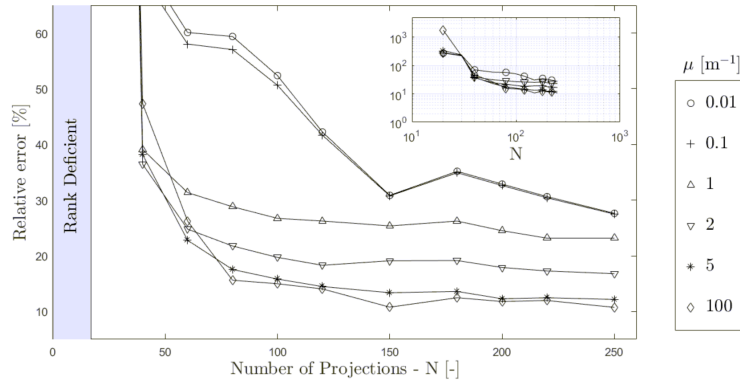


Figure 4: Placeholder figure: Convergence to a solution state with approximately 10% relative error was observed as the attenuation co-efficient  $\mu$  was increased.

176    The internal strain method was observed to require significantly more  
 177    projections to converge than that utilised in [7]. It was found that increas-

ing the magnitude of attenuation in simulated measurements significantly reduced the error seen in the reconstructed strain field. Convergence to a solution with total relative error in the order of 10 % was seen as the attenuation coefficient  $\mu$  was increased from  $0.1\text{m}^{-1}$  to  $5\text{m}^{-1}$ .

No appreciable reduction in error was seen for further increase in attenuation (to  $\mu = 100\text{m}^{-1}$ ) or number of projections (to 500). The strain reconstruction for  $mu = 100\text{m}^{-1}$ ,  $N = 250$  projections, and a mesh density of  $40 \times 80$  voxels are shown in figure 5.

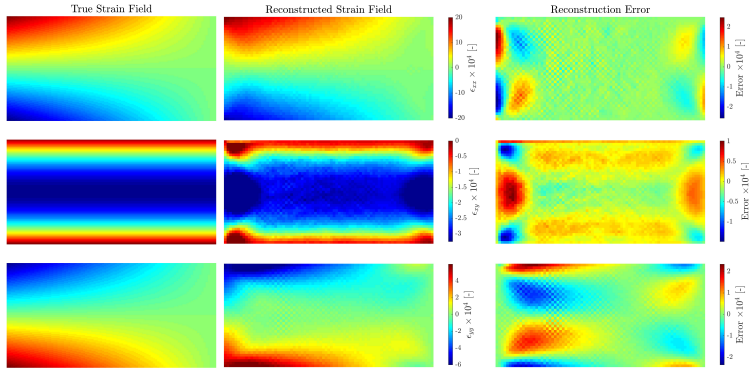


Figure 5: Left, Center: True and reconstructed  $\epsilon_{xx}$ ,  $\epsilon_{xy}$  and  $\epsilon_{yy}$  strain fields for a mesh discretisation of  $40 \times 80$  voxels and 250 projections, with  $\mu = 100\text{m}^{-1}$ . Right: Reconstruction error fields.

### 186 5.2.2. Reconstruction Error

187 The persistence of a 10% error floor prompted further study of the  
 188 reconstructed error fields. It is suspected that the error fields seen are largely  
 189 composed of elements from the kernel of the attenuated transform. Simulated  
 190 attenuated measurements through these *error* fields were found to be signif-  
 191 icantly smaller than the working strains — in fact, for the error fields shown  
 192 in figure 5, at least 80% of measurements were three orders of magnitude  
 193 below the working strains.

194 Figure ?? shows the same reconstruction results, but for a simulation  
 195 where a much smaller magnitude of attenuation was applied:  $\mu = 0.1\text{m}^{-1}$ .

196      Clearly, the error fields for this magnitude of attenuation are quite differ-  
 197      ent than that from the converged case. Again, measurements through these  
 198      error fields were significantly smaller than the working strains. Our hypoth-  
 199      esis is that the kernel of the attenuated transform is not trivial. This kernel  
 200      is certainly much smaller than that of the unattenuated transform — to lie  
 201      in the null space of the attenuated transform, fields must give rise the same  
 202      zero measurement in every direction of projection. Given that the weighting  
 203      by attenuation is non-symmetric about the ray center, this condition imme-  
 204      diately precludes a class of fixed-boundary fields which were previously in  
 205      the kernel of the unattenuated transform.

206      We hypothesise that as the magnitude of attenuation is increased, the  
 207      error observed in the reconstruction shifts from being composed largely of  
 208      unattenuated transform null fields to being composed of fields from the null  
 209      of the attenuated transform. Once a sufficient level of attenuation is reached  
 210      (here,  $\mu = 5\text{m}^{-1}$ , the error field is composed exclusively of elements from  
 211      the null space of the attenuated transform, and error due to the numerical  
 212      nature of the environment, and problem discretisation.

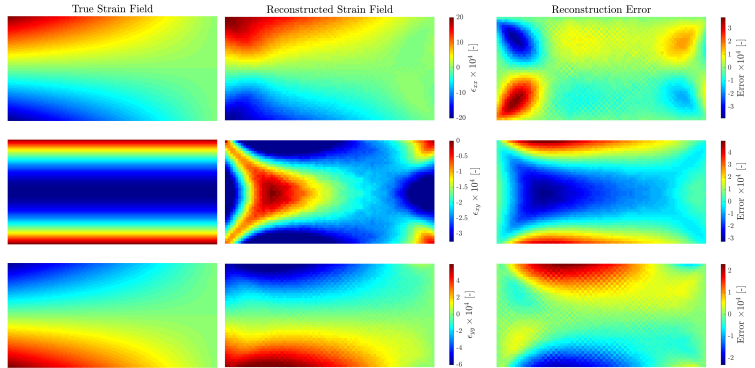


Figure 6: Left, Center: True and reconstructed  $\epsilon_{xx}$ ,  $\epsilon_{xy}$  and  $\epsilon_{yy}$  strain fields for a mesh discretisation of  $40 \times 80$  voxels and 250 projections, with  $\mu = 0.1\text{m}^{-1}$ . Right: Reconstruction error fields.

<sup>213</sup> 5.2.3. Error Field Compatibility

<sup>214</sup> In two dimensions, a strain field is said to be compatible if:

$$\frac{\partial^2 \epsilon_{xy}}{\partial x \partial y} - \frac{\partial^2 \epsilon_{yy}}{\partial x^2} - \frac{\partial^2 \epsilon_{xx}}{\partial y^2} = 0 \quad (14)$$

<sup>215</sup> Reconstruction error fields (including those shown in figures ?? and ??)  
<sup>216</sup> were evaluated for compatibility. The error field was smoothed with a Gaus-  
<sup>217</sup> sian filter ( $\sigma = 0.8$ ), and a least-squares surface fitting numerical differentia-  
<sup>218</sup> tion algorithm was implemented to calculate the relative incompatibility. In  
<sup>219</sup> both the cases where the error fields were suspected to be from the unatten-  
<sup>220</sup> uated transform null space and that of the attenuated transform, the error  
<sup>221</sup> fields were found to be compatible.

<sup>222</sup> 5.3. Reconstruction: Artificial, Incompatible Strain Field

<sup>223</sup> To further explore the possibility of the unattenuated transform null space  
<sup>224</sup> containing only compatible strain fields, a second example was reconstructed.  
<sup>225</sup> The geometry and discretisation of the cantilevered beam were maintained,  
<sup>226</sup> and a fabricated strain field of the following form was implemented:

$$\epsilon_{xx} = ay^3 \quad (15)$$

$$\epsilon_{yy} = bx^3 \quad (16)$$

$$\epsilon_{xy} = c(x + y)^2 \quad (17)$$

<sup>227</sup> Note that the co-ordinate system for this field has been shifted to the  
<sup>228</sup> center of the geometry. Constants  $a$ ,  $b$  and  $c$  were chosen to ensure a strain  
<sup>229</sup> of approximately  $1 \times 10^{-3}$  at the top-right vertex. This field is clearly in-  
<sup>230</sup> compatible at most  $(x, y)$  points, as:

$$\frac{\partial^2 \epsilon_{xy}}{\partial x \partial y} - \frac{\partial^2 \epsilon_{yy}}{\partial x^2} - \frac{\partial^2 \epsilon_{xx}}{\partial y^2} = 4c - 6ay - 6bx \quad (18)$$

<sup>231</sup> In other words, the condition for compatibility is:

$$6ay + 6bx = 4c \quad (19)$$

<sup>232</sup> Reconstruction results for this field,  $\mu = 0.1\text{m}^{-1}$ , and 250 projections  
<sup>233</sup> taken are shown in figure 7.

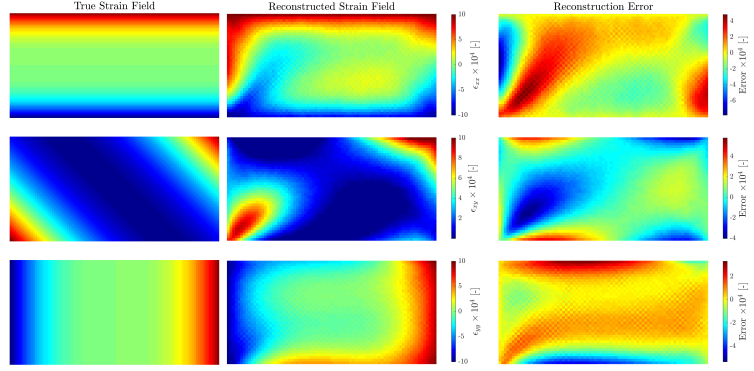


Figure 7: Left, Center: True and reconstructed  $\epsilon_{xx}$ ,  $\epsilon_{xy}$  and  $\epsilon_{yy}$  strain fields for a mesh discretisation of  $40 \times 80$  voxels and 250 projections, with  $\mu = 0.1\text{m}^{-1}$ . Right: Reconstruction error fields.

As before, more than 80% of the magnitudes of measurements through the error fields were at least three orders of magnitude smaller than the working strains, suggesting that the fields are largely composed of elements of the null space of the unattenuated transform.

Additionally, these error fields were found to be compatible.

## 6. Implications

- Results suggest the attenuated transform has a (smaller) null space
- Results also suggest that the null spaces of both transforms contain compatible strain fields
- We suspect they contain *only* compatible fields, but we're yet to prove this...